



Università degli Studi di Napoli
“Federico II”

DOTTORATO DI RICERCA IN FISICA

Ciclo XXXII

Coordinatore: prof. Salvatore Capozziello

**The role of fission in the search of
the super heavy promised land**

Settore Scientifico Disciplinare FIS/04

Author:
Alessandro Pulcini

Tutor:
Prof. Emanuele Vardaci

Anni 2017/2020

Università degli Studi di Napoli “Federico II”

Department of Physics

Doctor of Philosophy

XXXII cycle

Abstract

The role of fission in the search of the super heavy promised land

by Alessandro Pulcini

The study of the fission process is considered mostly important both for searching pathways to synthesize new superheavy elements and predict their stability against fission, and for the direct impact on the understanding of the fission recycling process in the r-process of nucleosynthesis. A description of the fission process with reliable predictive power is necessary, in particular, for low-energy fission where the fission-fragment mass distributions are strongly sensitive to microscopic effects. In this thesis, the study of five reactions aimed at a deeper understanding of the fission process in the mercury region is presented. This study was triggered by the recent hypothesis that the fission mechanism is different in the mercury region from the one postulated in the neighboring actinoid region. Furthermore, a method aimed at separating fission products from the ones produced by mechanisms with different time scales by means of the measurement of gamma rays in coincidence with binary fragments is presented. The main target of this method is the disentanglement of fission and quasi-fission products, two mechanisms with many common properties often overlapped in experimental data.

Contents

Introduction	1
Chapter 1 - Nuclear fission	4
1.1 Reaction mechanism classification	4
1.2 Fusion and fission	9
1.3 Quasi-fission	12
1.4 Dynamical description of fusion-fission and competitive mechanisms	14
1.5 Fission in heavy and superheavy nuclei	18
Chapter 2 – Experiment $^{64,68}\text{Zn} + ^{112}\text{Sn}$	24
2.1 Scientific motivation	24
2.1.1 Fission in the mercury region	24
2.1.2 Performed experiment	27
2.2 Experimental setup	29
2.2.1 CORSET	29
2.2.2 Electronics and trigger	33
2.2.3 CORSET time calibration	34
2.3 Results and discussion	35
2.3.1 Selection of binary reaction channels	35
2.3.2 Mass-TKE distributions	37
2.3.3 Selection of fusion-fission events	43
2.3.4 Fission modes in $^{180,176}\text{Hg}$	50
2.3.5 Discussion	60
Chapter 3 – Experiment $^{32}\text{S} + ^{197}\text{Au}$	65
3.1 Scientific motivation	65
3.1.1 Signatures of quasi-fission	65
3.1.2 Gamma ray probe	69
3.1.3 Performed experiment	69
3.2 Experimental setup	70
3.2.1 CORSET	70
3.2.2 ORGAM	71
3.2.3 PARIS	72
3.2.4 Electronics and trigger	73
3.2.5 ORGAM and PARIS calibration	75
3.3 Results and discussion	77

3.3.1 Selection of binary reaction channels	77
3.3.2 Selection of gamma rays in coincidence with binary reaction channels	78
3.3.3 The gamma ray fold distributions	79
3.3.4 The response matrix of ORGAM + PARIS	83
3.3.5 From gamma ray fold to multiplicity	86
3.3.6 Comparison with simulations	90
3.3.7 Angular momentum transfer	94
3.3.8 Discussion	97
Chapter 4 – Conclusions and perspectives	99
4.1 Experiment $^{64,68}\text{Zn} + ^{112}\text{Sn}$	99
4.2 Experiment $^{32}\text{S} + ^{197}\text{Au}$	100
References	102

Introduction

In the last few decades, through technological, experimental and theoretical advances, the outcomes of experimental fission studies have considerably progressed. With the use of advanced ion beam productions and detection techniques, much more detailed and precise information can now be obtained for the traditional mass regions of fission research and, more important, new regions of nuclei have become consistently accessible for fission studies. Nuclear fission is one of the most striking examples of a nuclear decay, where the nucleus splits predominantly in two smaller nuclei releasing a large amount of energy. It is a unique tool mostly important not only for searching pathways to synthesize new superheavy elements and to predict their stability against fission, but also for the direct impact on the understanding of the fission recycling process in r-process nucleosynthesis. A description of the fission process with reliable predictive power is therefore needed, in particular for low-energy fission where the fission-fragment mass distributions are strongly sensitive to microscopic effects.

This thesis will show two specific studies. The first is a campaign of five different reactions ($^{64, 68}\text{Zn} + ^{112}\text{Sn}$ at different bombarding energies) carried out with the aim of observing the fusion-fission (FF) mass distributions of ^{176}Hg and ^{180}Hg . The second is on the reaction $^{32}\text{S} + ^{197}\text{Au}$, used as a test for a method aimed at the disentanglement of fission and quasi-fission (QF) products, two mechanisms with many common properties often overlapped in experimental fission data.

The interest on the fission in the mercury region was triggered by a recent study in which it was observed the occurrence of asymmetric fission in ^{180}Hg , whereas in the neighboring pre-actinoid region predominantly symmetric FF mass distributions occur. Moreover, the repartition of the mass between the two fragments triggered the hypothesis that the fission mechanism in ^{180}Hg is also different from the one postulated in the actinoid region, where strong shell effects due to the nascent fission fragments are observed. In such a case, the fission of ^{180}Hg should have been a symmetric split (two ^{90}Zr fragments with shell closure $N = 50$). Several theoretical models have reproduced the experimental observation but experimental data for nuclei in the surrounding area are scarce: only few yield distributions have been measured, some with very limited statistics. Hence, it would be highly valuable to test experimentally the theoretical

predictions, especially considering that these same models are widely used in the literature throughout the whole Segrè chart and, in particular, in the superheavy mass region to estimate the stability against fission. The isotopes ^{176}Hg and ^{180}Hg , populated at different excitation energies, provide a particularly interesting testing ground for these models, due to their FF mass distributions expected to behave differently. The experiment has been performed at the JYFL accelerator laboratory in Jyväskylä (Finland) using a detection setup consisting of the CORSET time-of-flight spectrometer, for detecting the two fission fragments in coincidence.

The overlap in the mass symmetric region of the reaction products from FF and QF complicates the assignment of symmetric events to complete fusion on the basis of the mass distribution alone. Additional observables, besides mass distribution, should be used. The method proposed here relies on the fact that FF and QF are characterized by a different timescale. Within this framework a detailed study has been carried out to find out how timescales can be probed via angular momentum transfer as measured via gamma rays multiplicity, namely the number of gamma rays emitted per event. The proof of principle was explored by measuring the gamma rays in coincidence with two fragments in the reaction $^{32}\text{S} + ^{197}\text{Au}$ at beam energy near the Coulomb barrier. This reaction is characterized by a large FF cross section and a negligible contribution from the QF. The central part of mass-TKE distribution, corresponding to the symmetric scission, is therefore dominated by fragments originated in FF process and would not be polluted with components from processes of nearby time scale. Consequently, the comparison between the gamma multiplicity in the quasi-elastic (QE) channel and the FF channel would provide the best conditions to evaluate the validity of the concept described above. The experiment has been performed at the Tandem ALTO accelerator facility at IPN Orsay (France) using a detection setup consisting of ORGAM and PARIS detector arrays coupled with the CORSET time-of-flight spectrometer.

Thesis Layout

Chapter organization:

- Chapter 1 introduces the main features of nuclear fission, gives a brief description of a dynamical model used for its description and shows the behavior of the most commonly used experimental observables, with a focus on induced fission in heavy and super heavy nuclei;
- Chapter 2 and 3 contain details about the experiments mentioned above, the experimental setup, the analysis method and the result of data analysis performed by the author;
- Chapter 4 provides conclusions and remarks.

A Bibliography section follows.

Chapter 1 - Nuclear fission

1.1 Reaction mechanism classification

Nuclear reactions are induced by bombarding fixed target nuclei with accelerated ion beams. At energies comparable with the Coulomb barrier, given by:

$$E_B = \frac{1}{4\pi\epsilon_0} \frac{Z_1 Z_2 e^2}{r} \quad [1.1]$$

where r is the separation of the centers of the beam and target atomic nuclei and e the elementary charge, heavy ions typically have De Broglie wavelengths much smaller than their radii, so that in some respect their motion is similar to that of a classical particle.

On this basis, the overall features of nuclear reactions can be classified in terms of the impact parameter b , as shown in Figure 1.1. Four different b windows can be identified:

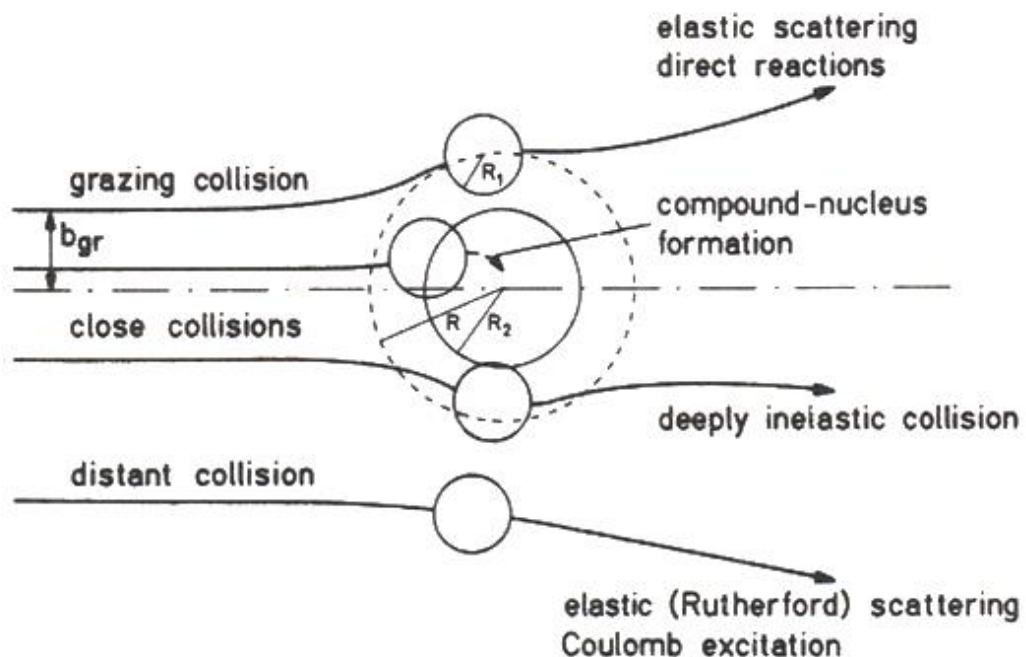


Fig 1.1 Reaction mechanisms as a function of the impact parameter b . [1]

- a) Distant collisions: $b_{gr} < b$
- b) Grazing collisions: $b_{dir} < b < b_{gr}$
- c) Close collisions: $b_{fus} < b < b_{dir}$
- d) Central collisions: $b < b_{fus}$

In case a) the impact parameter is bigger than the sum of the radii of the two atomic nuclei. The two nuclei can only interact through the Coulomb field and this results in Rutherford scattering and in case Coulomb excitation. b_{gr} is defined as the grazing impact parameter and it is equal to the sum of the radii of the two nuclei. It can be determined experimentally. As the impact parameter decreases, the increasing superposition of nuclear matter opens the way to new reaction channels.

In case b) the impact parameter value decrease down to b_{dir} , where deep inelastic reactions show up. In this window nuclear forces are no longer negligible and the trajectories after collision are defined by the competition between Coulomb and nuclear forces. These reactions come with some loss of relative motion energy, hence are called *quasi elastic* reactions.

In case c), with impact parameter reduced still further, the nuclei begin to interact very strongly. This happens quite sharply because the nuclear density rises very rapidly in the surface region and several scenarios where the produced nuclei differ from those interacting can be observed. The collision can produce the exchange of few nucleons among the interacting nuclei accompanied by a small reduction of the relative motion energy or in case of so called *deep inelastic* reactions a more massive nucleon transfer with large kinetic energy damp can occur. Hence, the relative motion energy loss is transferred to the reaction products that are produced in high excited states, with masses similar to those of the projectile and of the target.

In case d), if the energy is high enough to overcome the repulsive Coulomb potential, the complete fusion process becomes accessible. In complete fusion there is a complete superposition of the nuclear matter; the two nuclei lose their individuality and form a *compound nucleus* that reaches thermodynamic equilibrium. In this kind of process all the relative motion energy is transferred into the intrinsic degree of freedom and the system is in an excited state.

A discussion in term of the impact parameter is equivalent to a discussion in term of the angular momentum, being

$$l\hbar = \mu v_{\infty} b = k\hbar b \quad [1.2]$$

where k is wavenumber associated to the relative motion and μ is the reduced mass and v_{∞} is the relative asymptotic velocity. The total cross section for these processes σ_R may be estimated with angular momentum as

$$\sigma_R = \frac{\pi}{k^2} \sum_{l=0}^{\infty} (2l+1) T_l \quad [1.3]$$

where T_l is the transmission coefficient, i.e. the probability to form a CN in the collision between a projectile and the target nucleus with mutual angular momentum l . In the strong absorption model, it is usually used the sharp cut-off approximation for T_l

$$\begin{aligned} T_l &= 1 \quad l < l_{gr} \\ T_l &= 0 \quad l > l_{gr} \end{aligned} \quad [1.4]$$

where l_{gr} is the angular momentum corresponding to the grazing impact parameter. For a generic $l < l_{gr}$ one has that

$$\sigma = \frac{\pi}{k^2} (l+1)^2 \quad [1.5]$$

and, deriving with respect to l , one obtain

$$\frac{d\sigma}{dl} = \frac{2\pi}{k^2} l \quad [1.6]$$

From this formula, it is possible to identify three different windows of angular momentum limited by different values of l , as shown in Figure 1.2: $0 \div l_{fus}$ in which we have mostly fusion reactions; $l_{fus} \div l_{dir}$ in which we have mostly inelastic reactions; $l_{dir} \div l_{gr}$ in which we have mostly direct reactions. The first window can be further divided in two different windows. One at lower angular momentum values, where the excited compound nucleus has high probability to deexcite with the emission of light particles; this leads to the formation of the so-called *evaporation residue*. A second one for higher angular momentum values, where the fission barrier of the exit channel decreases and the fission decay becomes dominant; in this window there is mostly production of *fission fragments*.

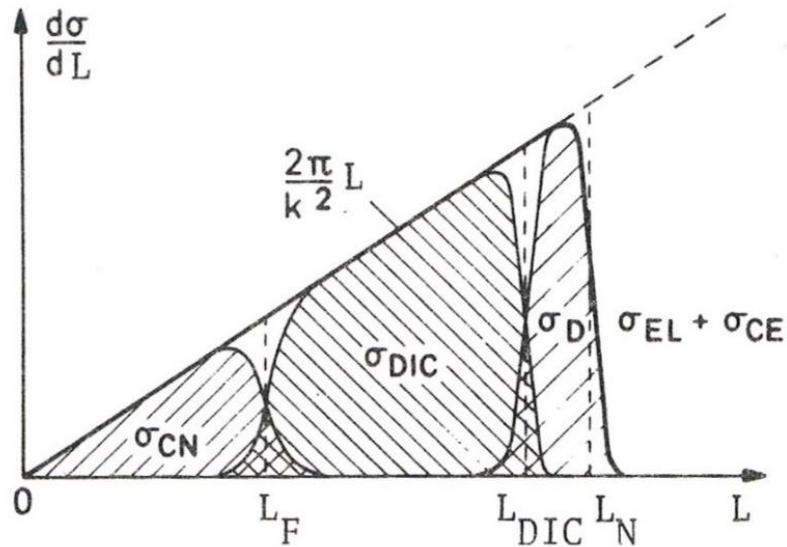


Fig 1.2 Reaction mechanisms as a function of the angular momentum l . [1]

Reaction mechanisms can also be categorized according to the time-scale of the interaction. Typical values extracted with systematics are:

- Quasi elastic reactions: $\tau_{int} < 10^{-22} s$
- Dissipative reactions: $10^{-22} s < \tau_{int} < 10^{-20} s$
- Complete fusion reaction: $\tau_{int} > 10^{-20} s$

It has to be said that the sharp distinction amongst mechanisms is somewhat blurred by a full quantum-mechanical treatment. The character of the interaction depends on the masses and charges of the two atomic nuclei and on their relative energy. Furthermore there are particular phenomena that occur in special circumstances.

Semi-classical models describing heavy ions reactions are based on an effective potential made by three terms [1]: the repulsive electrostatic Coulomb potential, equal to $Z_1 Z_2 e^2 / r$ outside the nuclei and rather less inside, the strongly attractive nuclear potential that essentially acts only within the volume occupied by the nuclei and falls off exponentially outside and the repulsive centrifugal potential $l(l+1)/r^2$ that accounts for the increasing difficulty for nuclei with higher momentum to approach each other. The sum of these three terms gives a series of potentials that depend on l and on the radial distance r as shown in Figure 1.3 for the case of $^{18}\text{O} + ^{120}\text{Sn}$.

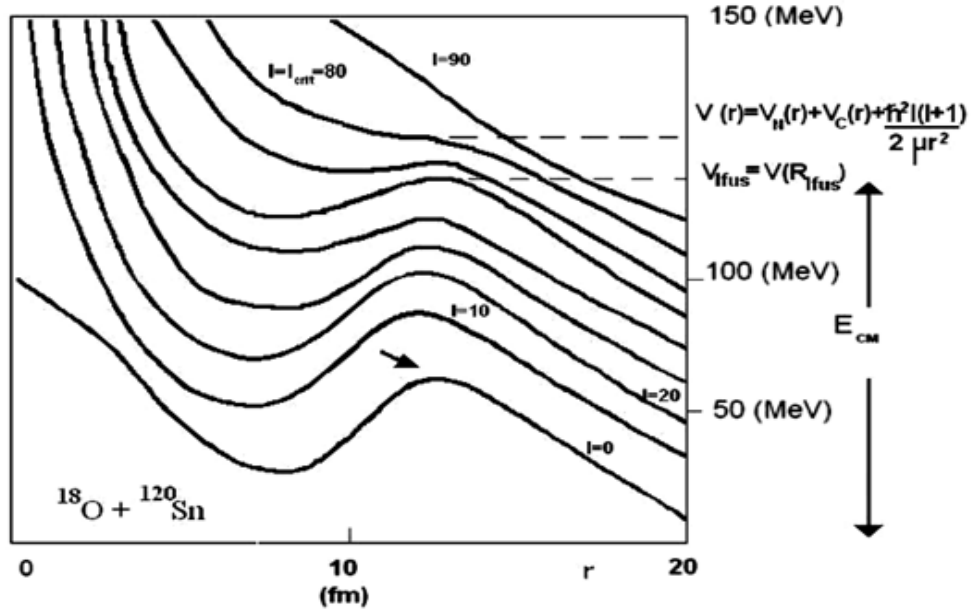


Fig 1.3 Effective potential for the system $^{16}\text{O}+^{120}\text{Sn}$ as a function of the radial distance of the center of the two nuclei. Different curves are for different values of the angular momentum. [2]

The value of l_{fus} is one of the most important quantities predicted by these models, because it allows to calculate the fusion cross section. In fact classically, in order for an incident ion with angular momentum l to cross the potential barrier, the relative kinetic energy should be higher than the value $V(l, R_{fus})$. Fusion can occur only if potential has a pocket and dissipative forces are strong enough to deexcite the system in to a bound state. These dissipative forces represent a schematization of energy transfer from the relative motions to intrinsic excitation. As l increases, the centrifugal potential increases and this means that the relative minimum of the potential will be less pronounced up to the disappearance of the pocket. Therefore, fusion does not occur for angular momentum higher than a critical value l_{crit} . Consequently, given the value of the energy of the relative motion in the center of mass (CM) reference frame E_{CM} , the maximum value of the angular momentum that allows the fusion to occur, the one identified before as l_{fus} , can be obtained imposing E_{CM} equal to the potential barrier $V(l_{fus}, R_{fus})$. l_{fus} is limited by the l_{crit} value beyond which fusion cannot occur anymore. In sharp cut off approximation, according to [1.5], the fusion cross section is

$$\sigma_{fus} = \frac{\pi}{k^2} (l_{fus} + 1)^2 \quad [1.7]$$

1.2 Fusion and fission

Reactions with low impact parameter, low angular momentum and enough kinetic energy to overcome the Coulomb barrier can lead to the complete fusion of the two nuclei with the formation of the compound nucleus (CN). During the interaction, all the relative motion energy and the relative angular momentum are distributed to the intrinsic degrees of freedom through a series of nucleon-nucleon interaction leaving the CN in a highly excited state. Due to the relatively long interaction time, $\tau_{int} > 10^{-20} s$, the system reaches thermodynamic equilibrium before the decay. The energy of the system is the energy of the relative motion in the center of mass reference frame plus the reaction Q-value; the angular momentum is the vector sum of the orbital angular momentum and the spins of the two nuclei.

It is called *nuclear fission* the process where the CN decays by splitting into two fragments of similar masses.

A model that describes the fission process is the *Rotating Liquid Drop Model* (RLDM). According to RLDM, the CN behaves like an incompressible macroscopic rotating liquid drop, with uniform charge distribution, that deforms in an elongated shape up to the separation of the two fragments. The nucleus shape is determined by the action of the attractive nuclear force that acts like a surface tension, and repulsive Coulomb and centrifugal forces. Therefore, a potential energy is defined as a function of deformation and of angular momentum. This potential has a maximum (*saddle point*) as shown in Figure 1.4 after which the nucleus has high chances to fission. At the scission point, the elongated nucleus breaks into two separate pieces, called *primary fragments*. Primary fragments have usually high excitation energy and cool down predominantly by neutron evaporation. Fragments, which no longer emit neutrons and deexcite by gamma ray emission, are called *secondary fragments*. Unstable ground states of secondary fragments decay by β^- emission until a stable nucleus is reached. This is illustrated schematically in Figure 1.5.

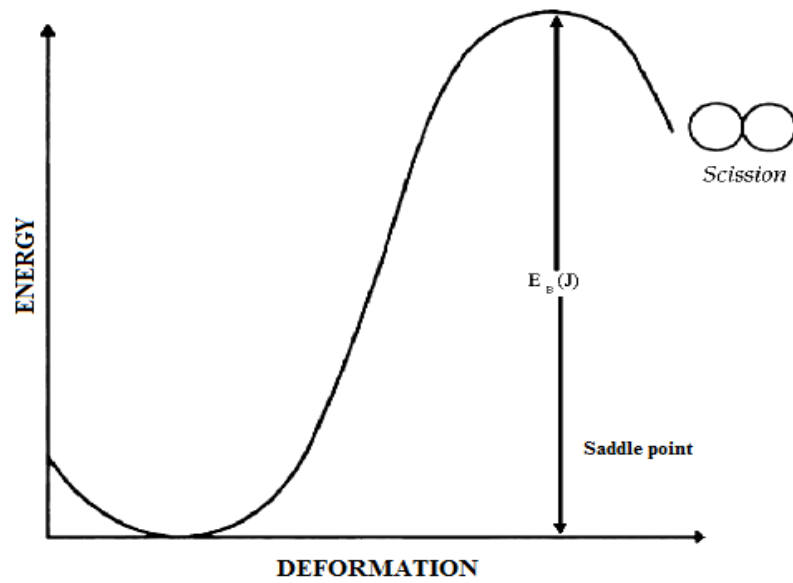


Fig 1.4 Fission potential as a function of the nuclear deformation.

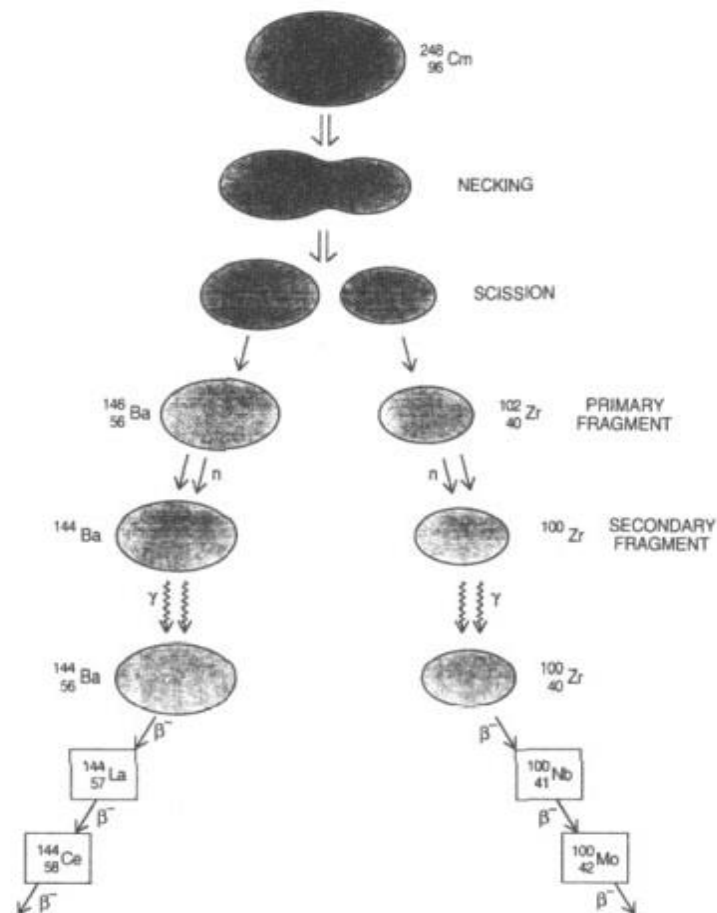


Fig 1.5 Schematic drawing showing the formation of fragments in the fission of ^{248}Cm . Primary and secondary fragments, as used in the text, are defined in this figure. [3]

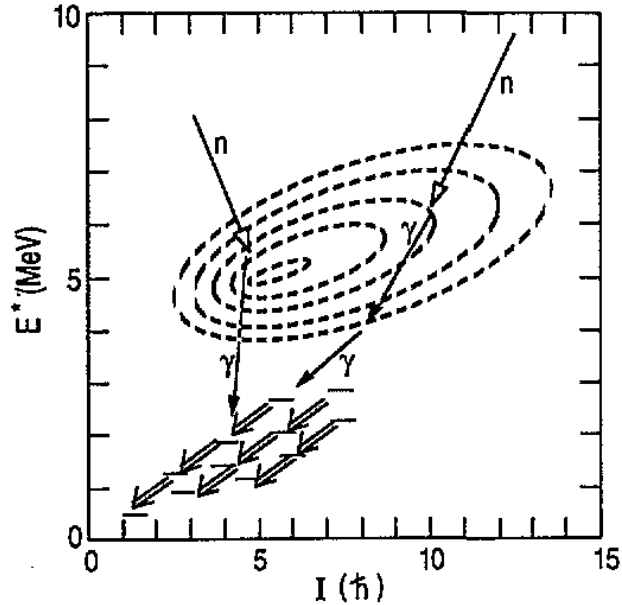


Fig 1.6 Schematic drawing showing entry points into a secondary fission fragment after neutron evaporation from a primary fragment. The contours, spaced roughly at intervals successively decreasing by factor of two, show the region of excitation energy and spin from which the secondary fragments deexcite by emission of statistical gamma rays to discrete yrast or near-yrast levels. [3]

Gamma rays in the secondary fragment arise from a broad range of excitation energy corresponding to the spread in energies of the neutrons emitted from the primary fragment. They also arise from levels with a large spread of spins corresponding to the spread in the primary fragments introduced by fission mechanism. There are also many gamma ray paths to the ground state from any point in this entry region. A variable number of *statistical* gamma rays, with essentially continuous energy distribution and relatively high energies of an MeV or greater, takes the secondary fragments from the initial chaotic entry region down to a more ordered regime in which there are rather few yrast or near-yrast levels. An yrast level is the state of a nucleus with the minimum excitation energy for a given angular momentum. This is illustrated schematically in Figure 1.6. The number of statistical gamma rays depends partly on the initial excitation energy of the primary fragment. This is higher for fission of high-excited systems but, typically, gamma ray deexcitation from the entry region involves from one to three statistical gamma rays per fragment [3]. Decays from the relative few levels populated in the yrast region are observed as *discrete* gamma rays.

From the potential energy defined within the RLDM, it can be derived a useful parameter, the *fissility parameter*. It is defined as the ratio between the Coulomb term and two times the nuclear term in the potential energy of a non-deformed nucleus,

giving a measure of the disruptive electrostatic forces compared to the surface tension. This parameter is related to the probability of the nucleus to decay by fission and it's defined as:

$$\chi = \frac{E_C^{(0)}}{2E_S^{(0)}} = \frac{Z^2/A}{(2a_S/a_C)\{1 - k[(N - Z)/A]^2\}} \quad [1.8]$$

where $E_C^{(0)}$ and $E_S^{(0)}$ represent respectively the Coulomb and the surface energy of the non-deformed nucleus, a_C and a_S are respectively the parameters related to $E_C^{(0)}$ and $E_S^{(0)}$ and k is the surface asymmetry constant. Values of χ are linked to the number of equal spherical shaped fragments that determine the absolute minimum in the effective potential energy [4]: for $\chi < 0.35$ a single sphere has the lowest energy, which means that a non-deformed nucleus with such a fissility parameter will decay preferably by emitting light particles; for $0.35 < \chi < 0.61$ two equal fragments at infinite separation have least energy; for $0.61 < \chi < 0.86$ three fragments; etc. These ranges are related to the tendency to form fragments with the strongest binding energy, which occurs for nuclei with $\chi = 1/4$. This corresponds to the region of in the vicinity of iron. Nuclei in this region are indeed among the relatively more abundant elements in nature.

1.3 Quasi-fission

In heavy-ion collisions at energy around the Coulomb barrier, the complete fusion process has to face a strong counteracting binary process, the *quasi-fission (QF)*. QF is a transitional mechanism between *deep-inelastic* collisions and complete fusion, in which the composite system separates in two main excited fragments without forming a CN due to the action of the repulsive Coulomb force.

Despite the QF process is strongly connected with the reaction entrance channel a clear picture of what are the most important characteristics that either enhance or hinder QF is still matter of discussion. Being the fusion-fission and QF products not simple to separate, three criteria are widely used to identify the dominant process in a given reaction:

- The reaction Coulomb factor Z_1Z_2 , the charge product of reaction partners. This

parameter relates to the Coulomb energy in the entrance channel. It has been identified a threshold value of $Z_1Z_2 = 1600$ for the appearance of QF.

- Entrance channel mass asymmetry

$$\alpha_0 = (A_p - A_t)/(A_p + A_t) \quad [1.9]$$

where A_p is the mass number of the projectile and A_t the mass number of the target. With decreasing mass asymmetry, the cross section for QF increases.

- Effective fissility parameter χ_{eff} connected with repulsive and attractive forces in the entrance channel. Recently, a mean fissility parameter was proposed in [5], given by $\chi_m = 0.75\chi_{eff} + 0.25\chi$, where χ is the one identified by the [1.8]. From analysis of a large data set, it has been found that QF take place for reaction with $\chi_m > 0.68$.

Those criteria, however, are not universal. For instance, they do not take into account the shapes of the interacting nuclei. The relative orientation of deformed nuclei changes the Coulomb barrier and the distance between the centers of the colliding nuclei and this leads to a change in the balance between repulsive and attractive forces.

The interaction energy is also a very important parameter for QF. The relative contribution of QF process decreases when the interaction energy increases. The question about the influence of angular momentum on the QF process is furthermore still open and additional experimental data including the gamma-ray probe can provide information on the excitation states of the reaction products needed to shed light on this point.

The QF has been described as a reaction mechanism in which, after the capture by nuclear attraction, there is a formation of an intermediate di-nuclear system. During the interaction there is an exchange of nucleons among the two partners but they re-separate due to Coulomb repulsion before reaching the complete amalgamation that leads to the CN formation. This interpretation implies a dynamical view of the interaction. A dynamical treatment, necessary for the description these processes, is discussed in the next Section.

1.4 Dynamical description of fusion-fission and competitive mechanisms

A dynamical description of a nuclear reaction cannot follow all the single particle degrees of freedom. Instead, it becomes important to identify some bulk degrees of freedom, which can provide a realistic picture of collective behavior. All the remaining degrees of freedom (unknown) are treated as a heat bath. The energy transfer between the degrees of freedom describing the collective motion of the excited nucleus and the internal excitation is schematized with the presence of dissipative forces. Hence, the forces leading the evolution of the system are the nuclear conservative potential, the dissipation treated with a friction term and a stochastic term depending on the temperature to introduce fluctuations. The equations that couple these degrees of freedom describe the time evolution of the reaction in terms of the chosen variables and their conjugate momenta. The choice of the variables to describe the shape of system is crucial to properly simulate the evolution of the system from the first interaction among the reactants until the formation of reaction products in order to provide a correct estimation of physical observables, *e.g.* cross sections of different competing reaction mechanisms. On one side, the number of degrees of freedom must be minimized in order to have a limited set of coupled differential equations to solve. On the other side, too few variables would not allow the simultaneous description of several configurations assumed by the complex system before the collision, during the survival of the di-nuclear system, and in the re-separation stages that determine the evolutive path of the nucleus, *i.e.* the competition among different reaction mechanisms as for instance fusion and QF.

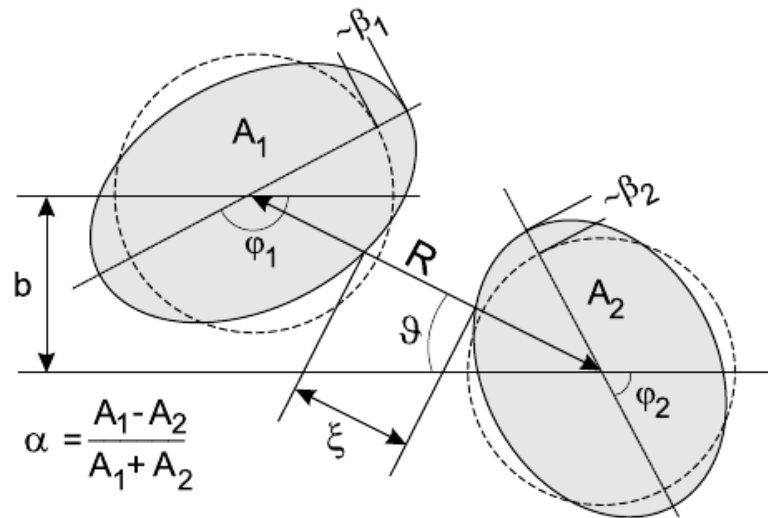


Fig 1.7 Schematic representation of the degrees of freedom used in the model to describe the nuclear shape of the complex system in a collisional event [6]

In the stochastic model of Zagrebaev and Greiner (DNS model) [6], the variables selected to describe the collision among two nuclei are the following:

- the distance R between nuclear centers or elongation of mono-nucleus;
- the quadrupole deformation of the two fragments, $\beta_{1,2}$;
- the mass asymmetry as defined by [1.9];
- the angle of rotation of nuclei in the reaction plane, $\phi_{1,2}$;
- the angle between beam axis and the line connecting nuclear centers, θ .

The equation that describe the time-evolution of each variable are in the form of Langevin type:

$$\mu\ddot{q} = -\frac{\partial V}{\partial q} - \gamma\dot{q} + \sqrt{\gamma T \Gamma(t)} \quad [1.10]$$

where :

- q is the generic degree of freedom;
- V is the potential energy (Coulomb + nuclear) plus the centrifugal barrier;
- γ is the friction coefficient associated to q ;
- $T = \sqrt{E^*/a}$ is the nuclear temperature, $E^* = E_{CM} - E_{kin} - V$ the excitation

energy, a the nuclear level density;

- $\Gamma(t)$, aleatory function with Gaussian distribution (zero mean value, takes into account stochastic diffusion).

The friction and the stochastic terms are responsible of the dissipation and are used to describe the mechanism of energy loss during mass transfer. The time evolution of the system represented by the chosen variables is represented by trajectories in the phase space.

One of the key ingredients of this type of models is clearly the choice of the potential once the degrees of freedom are chosen. The choice of the multidimensional potential determines the driving potential on which the trajectories of the solutions of the Langevin equations describe the possible reaction channels. For instance in Figure 1.8 is shown the driving *potential energy surface* (PES) of the ^{238}U nucleus depending on two variables: elongation and mass asymmetry. Figure 1.8 (a) shows the simplified macroscopic potential initially proposed to explain fission based on the *liquid drop model* (LDM). According to this model in a fission event the nuclear shape initially spherical elongates along the line of zero mass asymmetry due to the repulsive forces. The nuclear shape in the two-dimensional phase space evolves along the path indicated by the red line in Figure 1 (a): it overcomes the saddle point and reaches the scission point, splitting in two equal fission fragments.

While the LDM approach was able to qualitatively explain why fission is one of the main decay modes of heavy nuclei, it failed to describe the experimental observation that the fission happens asymmetrically too, giving rise to two fragments with different masses. The introduction of the microscopic corrections, given by the nuclear shell model, naturally led to the appearance of new valleys and peaks in the PES, as shown in Figure 1.8 (b), that were able to explain the appearance of the asymmetric fission-fragment mass distribution. As the microscopic shell effects depend strongly on specific neutron and proton numbers, their influence on the PES will differ among the nuclei, often leading to even more complex fission potential-energy landscapes with several fission valleys (or fission modes), each characterized by its unique saddle and scission points.

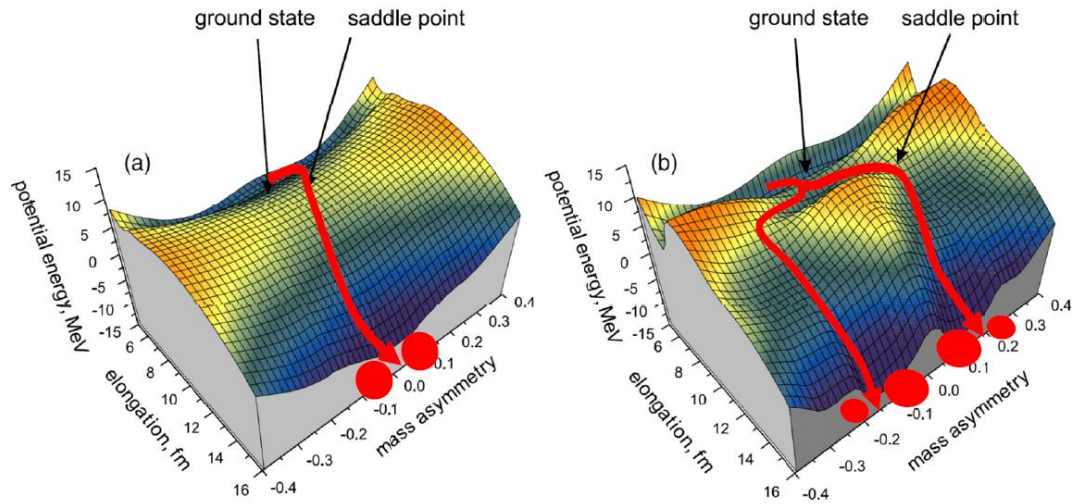


Fig 1.8 (a) Macroscopic and (b) total potential-energy surface for the ^{238}U nucleus as a function of elongation and fission-fragment mass asymmetry. The most probable fission paths (or “fission valleys”), which follow the lowest energy of the nucleus, are shown by the red lines with arrows. While in the LDM approach only symmetric fission can happen along the single symmetric valley, the introduction of microscopic shell effects produces the asymmetric fission valleys. [7]

A detailed knowledge of the potential for a given nuclear system allows to predict the more probable mass split or the most probable reaction mechanisms for reaction leading to that given nuclear system. In Figure 1.9 is shown the calculated PES as a function of elongation and mass asymmetry for the nuclear system formed in $^{48}\text{Ca} + ^{248}\text{Cm}$ collision. If the projectile energy is lower than the Coulomb barrier and tunneling effect does not occur, the reaction is expected to proceed through the deep inelastic channel. Otherwise, if the contact point is reached, the intermediate system can follow different paths and go through one of the possible valleys, due to the stochastic term in the Langevin equations. The different trajectories plotted in Figure 1.9 represent different reaction mechanisms, namely quasi-fission with asymmetric mass split (solid line “QF₁”), quasi-fission with symmetric mass split (solid line “QF₂”), fusion-fission (FF) with symmetric mass split (dashed line) that leads to the same mass asymmetric distribution of QF₂.

To study of FF and QF is so extremely important for several reasons: it highlights the presence of shell effects, it provides the basis for predicting properties of the fission of heavy and super heavy nuclei, it allows to measure the fusion cross sections for the most promising reactions for the synthesis of new super-heavy elements.

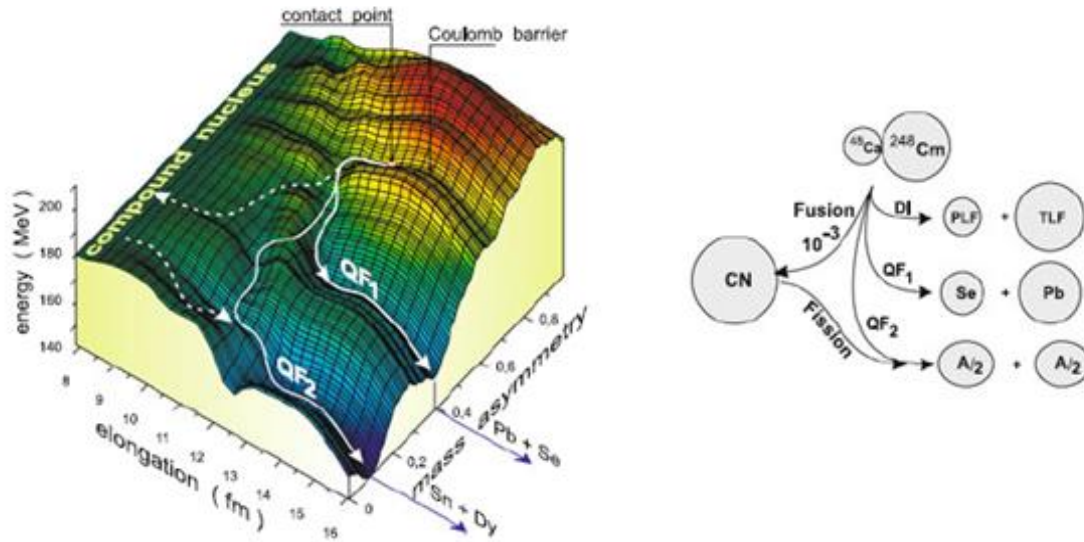


Fig 1.9 Example of a driving potential energy surface as a function of elongation and mass asymmetry for the nuclear system formed in $^{48}\text{Ca} + ^{248}\text{Cm}$ collision. The solid lines with arrows show schematically (without fluctuations) the quasi-fission trajectories going to the lead and tin valleys. The dashed curves correspond to fusion (CN formation) and fission processes.

1.5 Fission in heavy and superheavy nuclei

At relatively high excitation energy (~ 50 MeV), the influence of shell effects is negligible and the dominant process is the symmetric fission well described in the framework of the LDM. Due to the quenching of shell effects occurring at high excitation energy, the fission into two symmetrical nuclei is energetically favorable according to the LDM. It is well known that in the fission of heated nuclei the mass distribution of fragments is one-dumped and close to a Gaussian shape whose variance σ_M^2 increase approximately proportionally to the temperature of the fissioning nucleus. In Figure 1.10 the mass-TKE distribution of fission fragments of ^{216}Ra formed in the reaction $^{12}\text{C} + ^{204}\text{Pb}$ at CN excitation energy of 40 MeV is presented as an example of a classic case of LDM fission [8]. The TKE (*Total Kinetic Energy*) is the sum of the kinetic energies of the two fragments in the center of mass reference frame:

$$TKE = E_{CM}^{(1)} + E_{CM}^{(2)} \quad [1.11]$$

The solid curves in Figure 1.10 are the mass distribution, average TKE and its dispersion as function of fragment mass expected according to LDM with parameters set from the systematics.

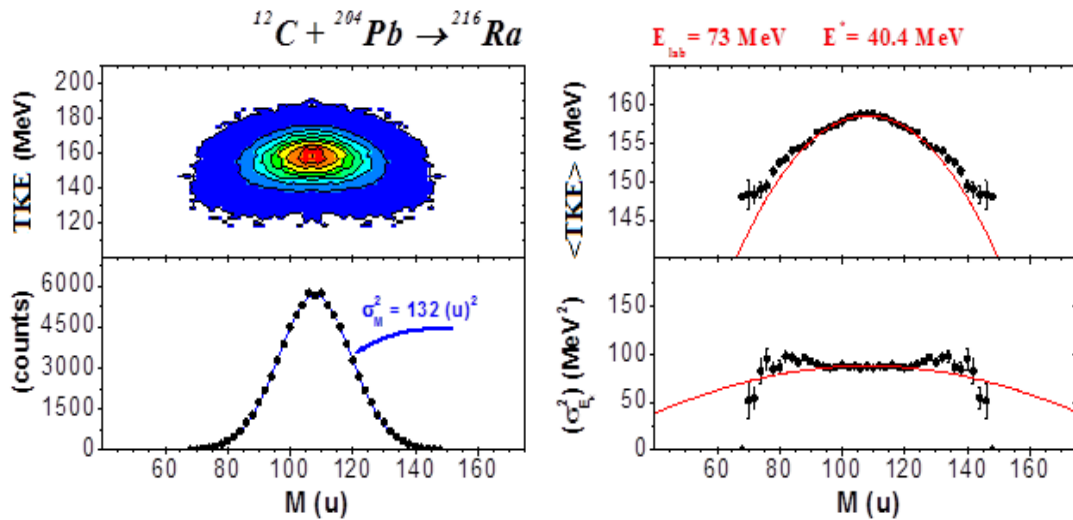


Fig 1.10 In the left column, from top to bottom: mass-TKE distribution of fission fragments of $^{216}\text{Ra}^*$ and mass distribution of fission fragments. In the right column, from top to bottom: average TKE distribution and TKE dispersion as function of the fragment masses. [8]

In the framework of LDM, the average TKE has a parabolic dependence on the fragment mass and does not depend on the initial excitation energy and angular momentum of the fissioning nucleus, but only on its mass and atomic numbers. The average TKE is expected to increase with the ratio $(Z_{CN})^2/(A_{CN})^{1/3}$, where Z_{CN} and A_{CN} are the atomic and mass number of the fissioning nucleus, as indicated by the formulas of well-known Viola systematics [9-10]. The formulas of this systematics predicting the average TKE for symmetric mass fragments (TKE_s , fragments with mass equal to $A_{CN}/2$) and asymmetric mass fragments (TKE_a , fragments with mass equal to A and $A_{CN} - A$) are:

$$TKE_s = 0.1189 \frac{Z_{CN}^2}{A_{CN}^{1/3}} + 7.3 \text{ MeV} \quad [1.12]$$

$$TKE = TKE_s A_{CN}^{-5/3} 2^{8/3} \frac{A (A_{CN} - A)}{A^{1/3} + (A_{CN} - A)^{1/3}} \quad [1.13]$$

Spontaneous and low energy fission have a different behavior. At low excitation energy, an asymmetric fission mode is observed in mass-TKE distribution of fission fragments for all nuclei from $A \approx 200$ u up to $A \approx 256$ u. For nuclei with $A < 220$ u the LDM symmetric mode prevails, with a small contribution ($< 0.5\%$) of the asymmetric component [11]. Whereas, for actinide nuclei with $Z = 90-102$ and $A = 226-256$ u the asymmetric mode prevails in spontaneous fission as well as in induced fission at

excitation energies up to 30-40 MeV. For transitional cases like nuclei in the region of Ra [12] or Ac [13], the mass distributions at low energy fission are a superposition of symmetric and asymmetric modes with comparable contributions.

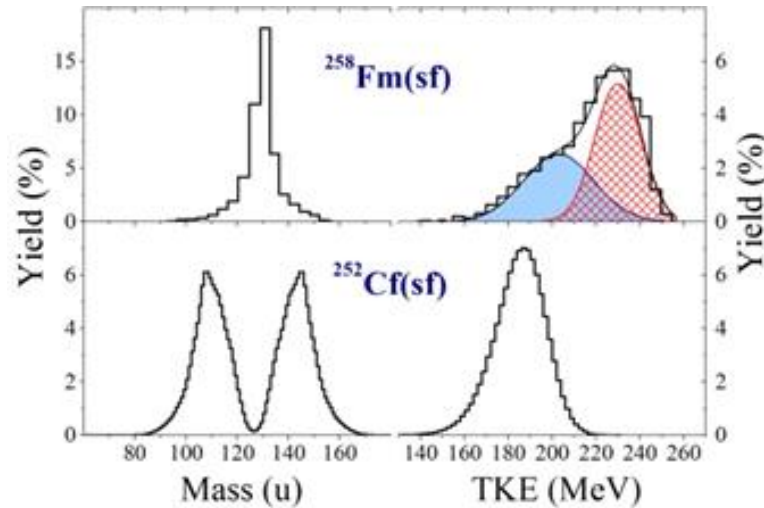


Fig 1.11 The mass and TKE distributions for spontaneous fission of ^{252}Cf and ^{258}Fm [14].

The phenomenon of bimodal fission has been observed for the case of spontaneous and low energy fission of nuclei in Fm–Rf region. Bimodality means the co-existence of two different modes of fission having both symmetric mass but two different average values of TKE in the same nucleus. The TKE distribution strongly differs from a Gaussian shape distribution as found in the fission of all other actinides. It is important to note that bimodal fission appears for Fm isotopes ($Z=100$) and more heavy elements when two fission fragments are close to the spherical proton $Z=50$ and neutron $N=82$ shell closures. An example of this phenomenon is given in Figure 1.11 for the spontaneous fission of ^{252}Cf and ^{258}Fm . The mass distribution of ^{258}Fm is symmetric and the associated TKE distribution can be decomposed into two Gaussian distributions. The opposite holds true for the spontaneous fission of ^{252}Cf for which the mass distribution is grossly asymmetric and the TKE grossly unimodal. These findings cannot be explained by the LDM, and it was natural to resort to shell effects.

In Figure 1.12 is given an overview of the measured mass and nuclear-charge distributions of fission products from low-energy fission [15] described so far. It shows a region of the Segrè chart around ^{208}Pb (the nucleus in correspondence of the two spherical shell closures $Z = 82$ and $N = 126$). Black empty squares are for stable nuclei, blue and green symbols mark nuclei whose mass distribution has been measured (blue

symbols for direct kinematics: circles for mass distributions and plus symbols for Z distributions; green cross symbols for Z distributions in inverse kinematics). Red distributions are taken from experimental data.

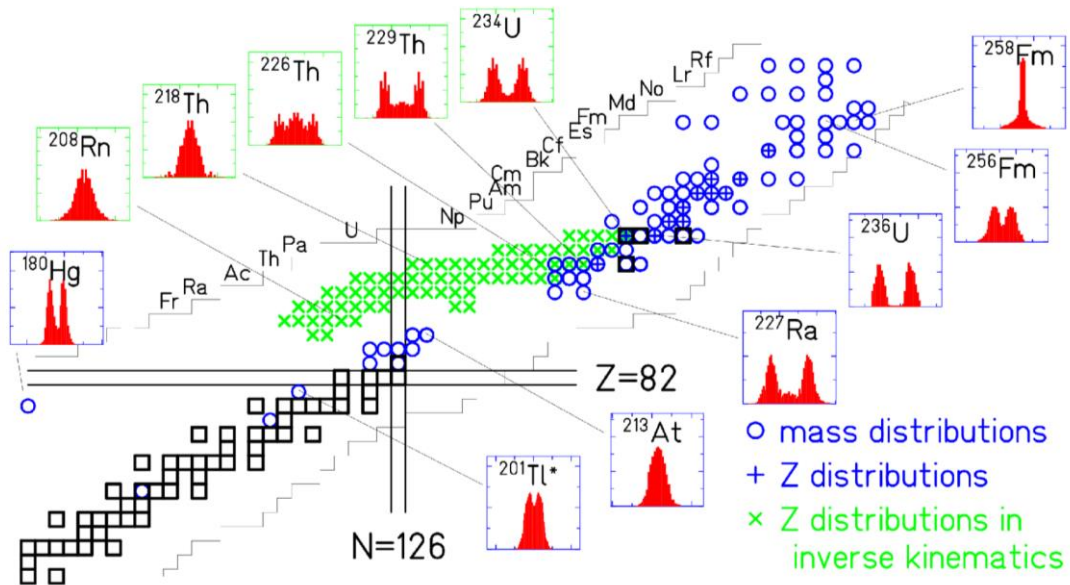


Fig 1.12 Region of the Segrè chart around ^{208}Pb . Blue and green symbols indicate a measured mass distribution. Blue symbols are for measurements in direct kinematics: circles for measured mass distributions and plus symbols for measured Z distributions; green cross symbols are for measured Z distributions in inverse kinematics. The red mass distributions are from experimental data. Black empty squares are for stable nuclei [15].

The above properties of the fission fragments mass distributions have been understood qualitatively, and in some case quantitatively on the basis of the concept of multimodal nuclear fission, whose foundation arises from the valley structure in the PES in the multimodal deformation space of the fissioning nucleus, as shown in Figure 1.9. In a frame of a two-center shell model, the PES exhibits a sequence of pronounced valleys as the consequence of the shell structure of the forming fragments. Four main fission modes, in accordance with Brosa model [16], have been distinguished in theoretical calculations as well as experimentally:

- symmetric mode;
- standard I mode, caused by the influence of spherical proton $Z = 50$ and neutron $N = 82$ shell closures;
- standard II mode determined by deformed nuclear shell closures with $Z \approx 54-56$ and $N \approx 86$;

- supershort mode, manifesting itself only when light or heavy fragments are close in their nucleon composition to the double magic tin with $A \approx 132$ (^{132}Sn).

Empirically, the multimodality is supported by the reproduction of measured mass and TKE spectra of fission fragments as a sum of several Gaussian curves representing each fission mode. For instance, although the mass distribution for ^{258}Fm in Figure 1.11 is symmetric, the TKE distribution is represented by a sum of two components: one is centered at TKE ≈ 200 MeV characterized by symmetric fission mode, the other distributed around 230 MeV, corresponding to the super-short mode.

The average TKE of fission fragments is determined by the mutual Coulomb repulsion among the primary fragments at scission point, which, in turn, depends on the shape of the two fragments. The different TKE values of the different fission modes could be explained by considering different paths in the PES. One path reaches the scission point in a stretched neck configuration, as the one predicted by the LDM; the other reaches the scission point in a touching sphere configuration and therefore higher TKE than the other path.

The same PES concept can also explain the widths of the mass and TKE distributions. According to the shape of the PES, the distribution width grows with the valley width: wider valleys correspond to larger widths. Therefore, even if two paths result in symmetric mass distributions, the higher TKE valley is narrower than the lower TKE valley. This explains the differences in the widths of the mass and TKE distributions of the different modes.

In Figure 1.13 are shown the mass distributions, the average TKE and its variance as a function of the mass of the binary product of the $^{18}\text{O} + ^{208}\text{Pb} \rightarrow ^{226}\text{Th}$ reaction for different excitation energy of the CN [17]. The mass distributions are reproduced summing the contributions of symmetrical fission mode (the filled areas) and asymmetrical fission modes standard I and standard II (hatched areas). In the average TKE distributions, it is possible to notice that for asymmetric fission modes the TKE has higher value than for symmetric fission.

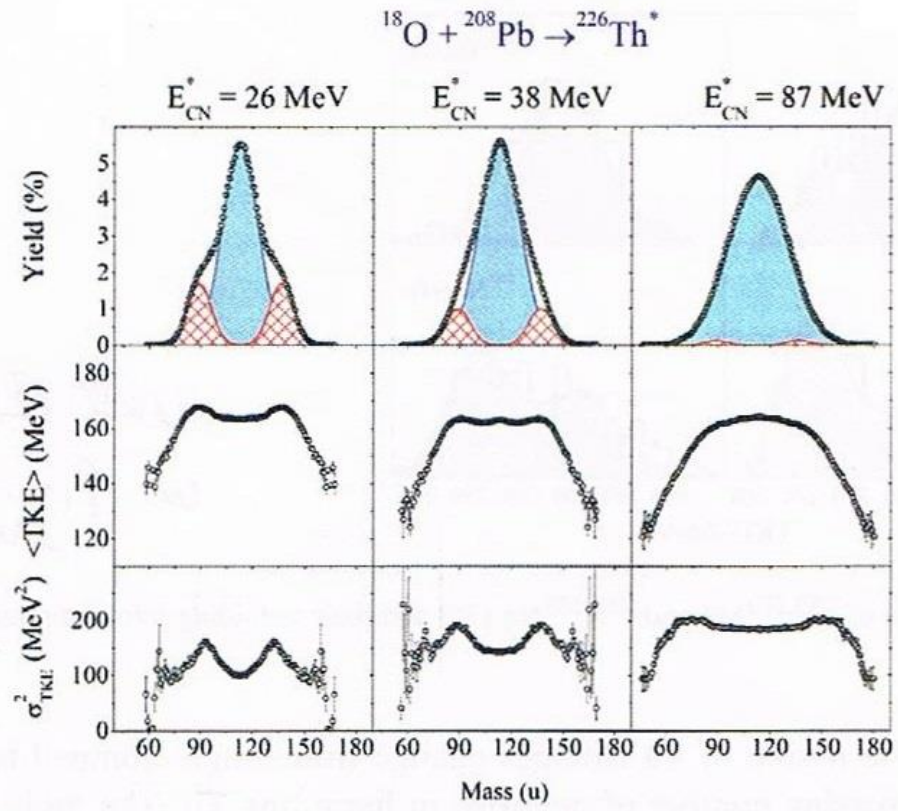


Fig 1.13 Mass-TKE distributions of binary product of the $^{18}\text{O} + ^{208}\text{Pb}$ reaction at different excitation energies. From top to bottom: mass yields, average TKE and its variance as a function of mass. Filled areas in the mass distributions are associated to symmetric mode, hatched are associated with the sum of standard I and standard II asymmetric modes. [17]

Chapter 2 – Experiment $^{64,68}\text{Zn} + ^{112}\text{Sn}$

2.1 *Scientific motivation*

The process of nuclear fission continues to provide new and unexpected features regardless of a long history of intensive theoretical and experimental studies [18]. The study of the fission process is considered presently mostly important not only for searching pathways to synthesize new superheavy elements and to predict their stability against fission, but also for the direct impact on the understanding of the fission recycling process in r-process nucleosynthesis [19]. A description of the fission process with reliable predictive power is therefore needed, in particular for low-energy fission where the fission fragments mass distributions are strongly sensitive to microscopic effects. Many observations, summarized in Section 1.5, strongly support the hypothesis that nuclei may fission through several independent fission modes (multimodal fission) corresponding to different precission shapes and fission paths in a multidimensional potential-energy landscape, in which shell effects are dominant.

2.1.1 *Fission in the mercury region*

In the pre-actinoid region, predominantly symmetric FF mass distributions have been observed. Recently, in a study of β -delayed fission of ^{180}Tl at ISOLDE, CERN, it was observed the occurrence of asymmetric fission in ^{180}Hg [20-21], with the most probable mass numbers in the mass distribution at ~ 80 for the mass of the light fragment and ~ 100 for the mass of the heavy one. This result triggered the hypothesis that the fission mechanism in ^{180}Hg is different from the one postulated in the actinoid region, where strong shell effects of the nascent fragments, driven by the double magic ^{132}Sn , decide the shape of the mass distribution. For such a case, the fission of ^{180}Hg should have been a symmetric split in two ^{90}Zr fragments ($N = 50$ shell closure in the fragments). The mechanism occurring in the fission of ^{180}Hg should therefore be different from the one in the actinide region, since strong shell effects due to the nascent fission fragments are not observed.

Several theoretical models have reproduced this observation [22-24]. In Ref. [22],

Panebianco and collaborators have performed scission-point calculations that can explain the asymmetric splitting of ^{180}Hg and the symmetric splitting of ^{198}Hg as connected to shell effects of the fragments (spherical and deformed ones) in the determination of the most probable fragmentation. Using a micro-macro scission point model, Andreev and collaborators [23] have studied the isotopic chain of mercury and predicted an evolution from symmetric distribution in ^{174}Hg to asymmetric around ^{180}Hg and more symmetric for $^{192-196}\text{Hg}$. Finally, they showed that the observed asymmetric mass distribution can be understood in terms of conventional fragment shell effects at the scission point where the most probable mass split away from symmetry is attributed to the deformed scission-point configurations. These calculations also predict that the influence of the excitation energy on the shape of the mass distribution is rather weak.

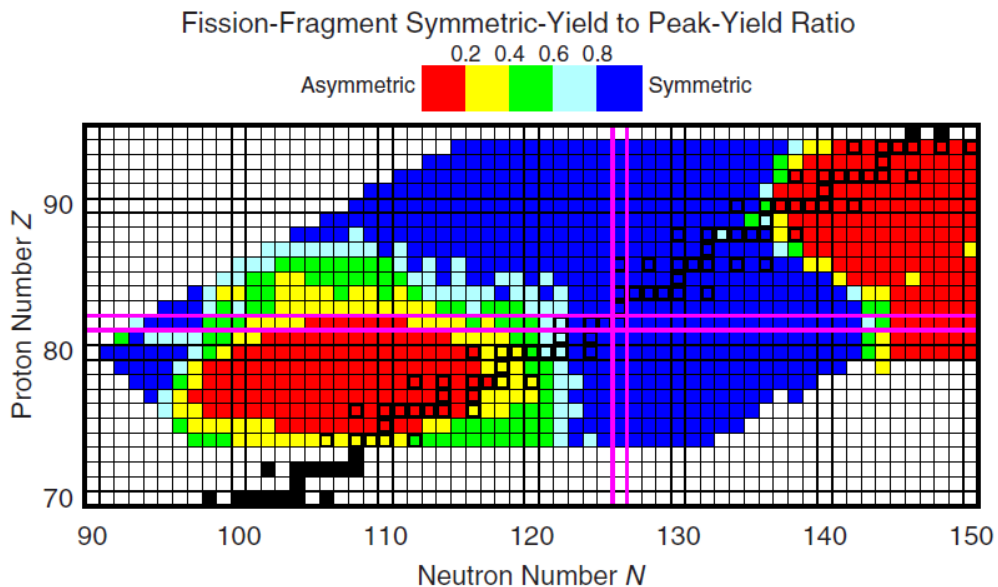


Fig 2.1 Calculated symmetric-yield to peak-yield ratios for 987 fissioning systems. Black squares (open in colored regions, filled outside) indicate β -stable nuclei [24].

The most extensive calculations of the FF mass yields were carried out by Moller *et al.* [24] by using a recently developed Brownian Metropolis shape-motion treatment on 5D micro-macro potential energy surface. The larger dimensional space has highlighted that the potential surface changes very rapidly and consequently the asymmetric mass distribution in ^{180}Hg is attributed to the rapid localized single-particle effects in the vicinity of the saddle point. A concise overview of the calculated fission modes expected is shown in Figure 2.1. Two extended regions of asymmetric fission are drawn in red color. The one in the bottom left corner is the predicted region of the new type of

asymmetric fission and includes $^{178,180}\text{Hg}$, while the previously known asymmetric fission region in the heavy actinides is seen in the top right corner. These two red regions are separated by a region of predominantly symmetric fission (shown in blue) which is now considered to be another transitional region.

Experimental data for nuclei in the blue and red colored lower left corner of Figure 2.1 are scarce: only ten or so yield distributions have been measured, some with very limited statistics [18]. Regions where there might be differences between calculated results and measurements lie near the calculated transition line between symmetric and asymmetric fission. To draw more definite conclusions about the accuracy of the present implementation of Moller's model in this region experimental data for additional nuclides are clearly needed. Because the nuclear potential-energy structure is so different in this region compared to the actinide region, additional experimental data together with fission theory studies, which incorporate additional dynamical aspects should provide new insights.

To dig inside the fission modes, it is very useful to explore the neighboring isotopes. For what it concerns with the Hg region, Figure 2.2 shows calculated yields [25] for four even Hg isotopes from ^{174}Hg to ^{180}Hg for three different excitation energies: 2 MeV above the calculated saddle energy, 20 MeV, and 40 MeV. The experimental analysis indicates a mass yield of ^{180}Hg that is clearly asymmetric, with the most probable heavy and light masses of 100 and 80, respectively [20]. The calculations, though providing an asymmetric mass distribution, miss the most probable masses by about 10 mass units. However the calculated yields for ^{180}Hg become narrower and tend toward the masses 100 and 80 as the compound-system energy decreases.

The following trends in the calculated fission-fragment mass distributions in Figure 2.2 are particularly remarkable: (1) for the lighter isotopes the yield distributions are flatter and less dependent on energy than in the heavier region; (2) for ^{174}Hg and ^{176}Hg the yield distribution becomes more asymmetric with increasing energy. This behavior is at variance with all the other Hg isotopes, also heavier ones. Hence, it would be highly valuable to test experimentally the theoretical prediction of an anomalous energy dependence for the lighter Hg isotopes. The test of Moller's model acquires much more relevance by considering that its predictions concerning the fission barriers and ground state deformations are widely used in the literature throughout the whole Segrè chart and, in particular, in the superheavy mass region to estimate the stability against fission. For instance, the issues why the center of the superheavy region, where fission barriers

are higher, does not overlap with the expected magic number $Z=114$ and $N=184$ and the fission barriers are of about 1 MeV higher than the few measured near the superheavy island are still not understood. These are important aspects that should require additional insight and experimental data.

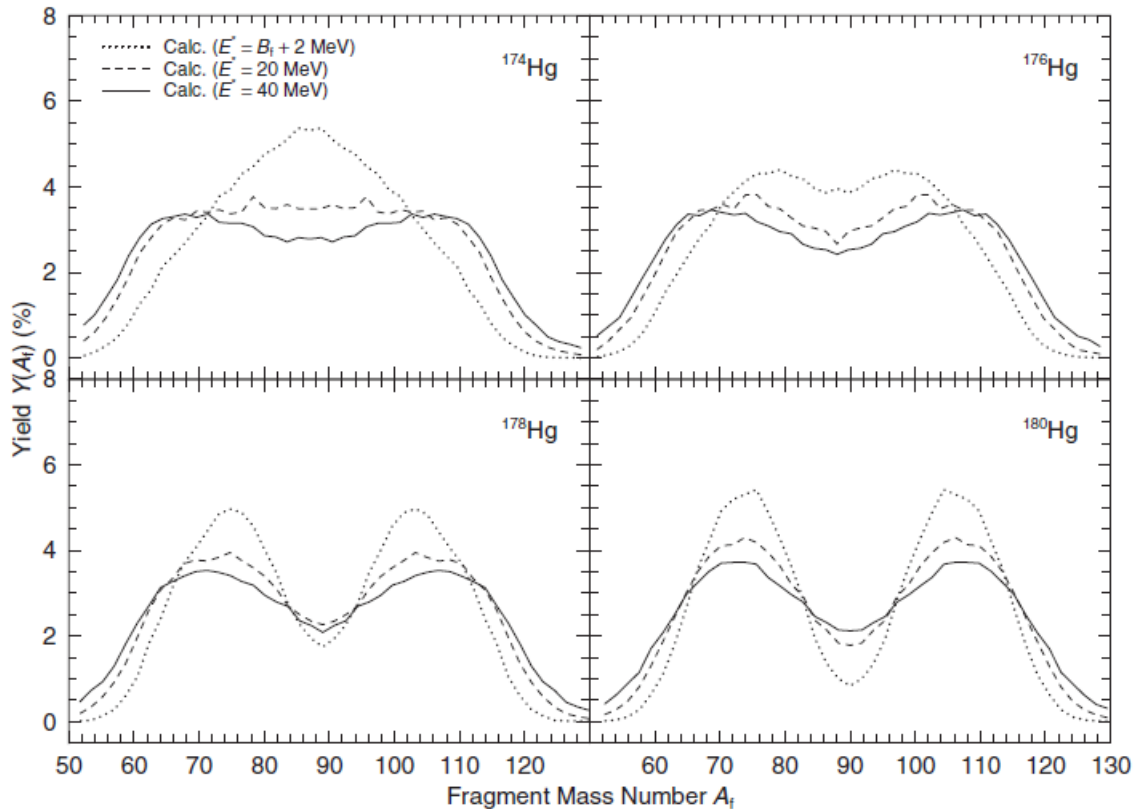
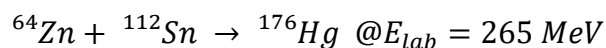
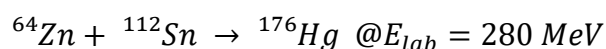
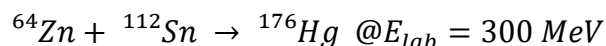
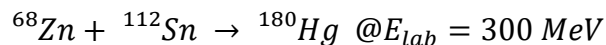
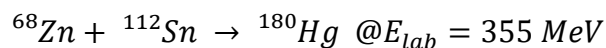


Fig 2.2 Calculated yields for four Hg isotopes at three excitation energies. For the lighter isotopes the yields become more asymmetric with increasing energy, an unusual behavior. [25].

2.1.2 Performed experiment

As a key test for Moller's predictions, the following reactions have been studied at the JYFL accelerator laboratory in Jyväskylä (Finland):



Relevant information are shown in Table 2.1. If fusion occurs, these reactions lead to the

formation of $^{176, 180}\text{Hg}$ whose fission fragments mass distributions should behave in opposite ways with growing excitation energy of the CN.

It is remarkably interesting to get insight in the fission fragments mass distribution for ^{176}Hg , never measured before, because Moller *et al.* have predicted that it becomes more asymmetric at higher excitation energy, contrarily to all known expectations about the damping of the shell effects. The experimental finding of this feature could offer a key for the explanation of Moller's prediction that the mass region around Hg has different features than all the nearby regions as for instance the actinide one, where fission is asymmetric and becomes more symmetric with the increasing of excitation energy.

Tab 2.1 Table of the most relevant parameters concerning the measured reactions: projectile energies (both in laboratory, E_{lab} , and center of mass, E_{CM} , reference frames); Coulomb barrier, V_C ; fusion Q value; excitation energy of the CN, E_{CN}^* ; fission barrier of the CN, B_f .

$^{68}\text{Zn} + ^{112}\text{Sn} \rightarrow ^{180}\text{Hg}$					
E_{lab} [MeV]	E_{CM} [MeV]	V_C [MeV]	Q [MeV]	E_{CN}^* [MeV]	B_f [MeV]
355	221	172.2	-138.7	82	9.8
300	187	172.2	-138.7	48	9.8
$^{64}\text{Zn} + ^{112}\text{Sn} \rightarrow ^{176}\text{Hg}$					
E_{lab} [MeV]	E_{CM} [MeV]	V_B [MeV]	Q [MeV]	E_{CN}^* [MeV]	B_f [MeV]
300	191	173.5	-142.8	48	9.6
280	178	173.5	-142.8	35	9.6
265	169	173.5	-142.8	26	9.6

Mass-TKE distributions of the reaction products can be measured by using a kinematic method, namely by measuring the time-of-flight of two fragments in coincidence along with the momentum and mass number conservation laws. In this way the mass and TKE distributions of primary fragments are obtained.

A description of the experimental setup and the analysis method used is provided in the following Sections.

2.2 Experimental setup

2.2.1 CORSET

Binary reaction products of the five studied reactions have been detected in coincidence by using the two-arm time-of-flight (ToF) spectrometer CORSET (CORrelation SETup) [26]. Each arm of the spectrometer consists of a compact start detector and a position-sensitive stop detector, both based on microchannel plates (MCP). Depending on the reaction under investigation, the arms can be positioned at different angles to the beam axis. The distance between the start and stop detectors of each arm (the flight path) and the distance from the start detector to the target can be adjusted as needed .

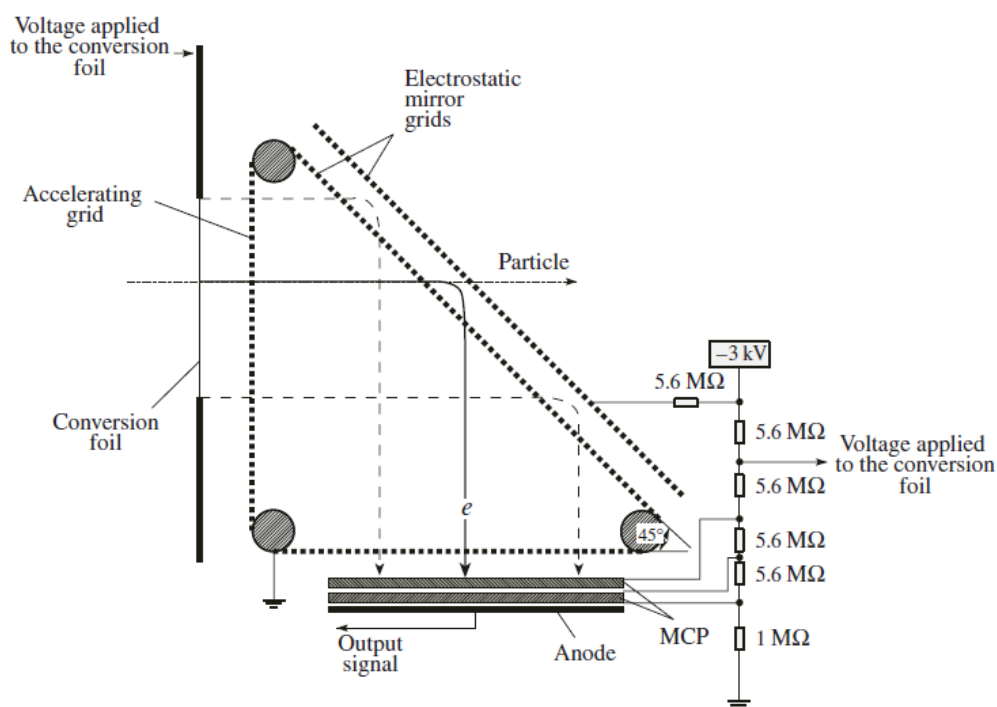


Fig 2.3 Schematic diagram of the start detector. [26]

The start detector is composed of a conversion foil, an accelerating grid, an electrostatic mirror and a chevron MCP assembly. A schematic diagram of a start detector is shown in Figure 2.3. When passing through the conversion foil of the detector, a particle (from protons to heavy ions) knocks out electrons, which are accelerated in the electric field between the foil and the accelerating grid to an energy of ~ 3 keV. The grids of the electrostatic mirror deflect the electrons by 90° , and then they hit the chevron MCP assembly. Wherever a particle hits the entrance foil, the electron

ranges have the same length; therefore, the output time signal is position-independent. The detector design has been optimized in order to obtain the maximum active area for a minimum detector size.

The entrance foil can be made either of carbon or mylar. An aluminum or gold layer may be sputtered on the mylar foil to raise the secondary yield of electrons. A particle passes through all electrostatic fields generated by the grids without being deflected from its primary direction and practically without changing its initial velocity. Nevertheless, one must take into account the energy lost by a particle in its passage through the conversion foil. For fission fragments, these losses in the used foils are few MeV (2–5% of the initial energy of a particle). The change in the particle direction due to collisions with atoms of the foil appears to be negligible.

The stop detector consists of a conversion entrance foil directly mounted on an assembly of two MCPs and coordinate system and a printed circuit board with fast amplifiers for one time signal and two coordinate signals. A schematic diagram of a stop detector is shown in Figure 2.4. The coordinate system consists of two mutually perpendicular delay lines of wire. Each “coordinate” is composed of two independent delay lines shifted by 0.5 mm with respect to each other. The voltages applied to the delay lines are selected so that electrons escaping from the MCP are collected on only one of them. The other delay line (which does not collect electrons) is used to compensate for the interference of the fast time signal from the exit surface of the MCP. The coordinate of a particle’s hit point at the detector is determined from the difference in the arrival time of the time signal and the signal from the relevant delay line. The angular resolution of the stop detectors is about 0.3° .

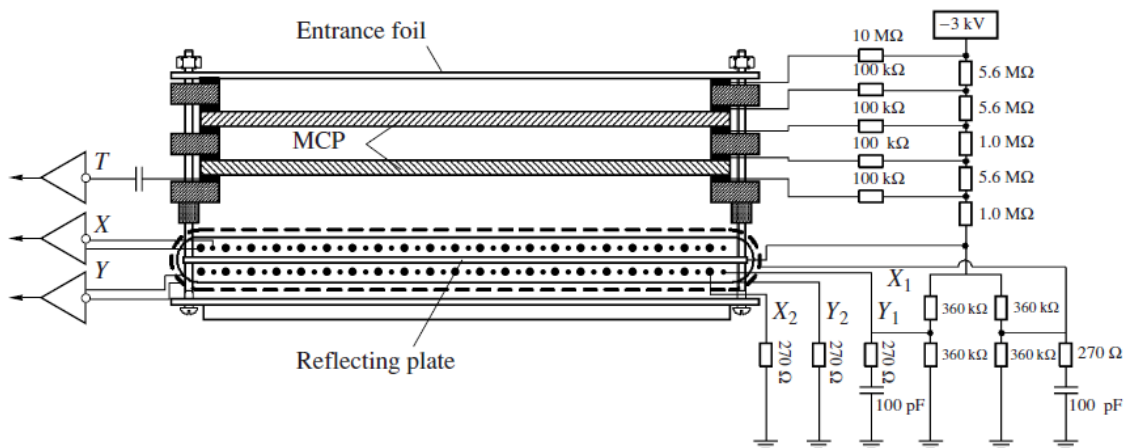


Fig 2.4 Schematic diagram of the position-sensitive stop detector. [26]

In order to monitor the beam intensity and its position at the target and to register beam ions that are elastically scattered by target nuclei, four surface-barrier detectors, the so-called beam monitors, are placed into the reaction chamber symmetrically with respect to the beam. Knowing the counting rates of elastically scattered ions for each of the four detectors and comparing them to the values calculated from the Rutherford elastic scattering, one can find the point of incidence of the beam onto the target.

The time resolution, taken as the full width half-maximum (FWHM), of both ToF arms is 150 ps. The mass resolution is 3 u. The geometrical efficiency of CORSET spectrometer is about 3%.

In the present experiment, two different geometries were used. For all the reactions, data have been taken with a symmetric geometry of the CORSET detectors. Moreover, for two reactions ($^{64}\text{Zn} + ^{112}\text{Sn}$ at $E_{\text{lab}} = 280, 265$ MeV), additional data have been taken with an asymmetric geometry. In the symmetric geometry, the two arms of CORSET were at $\pm 45^\circ$ from the beam axis. In the asymmetric geometry, the two arms of CORSET were at -35° and $+70^\circ$ from the beam axis. In both the configurations and for both arms, the start detectors were at 52 mm from the target and the stop detectors at 300 mm from the start. The size of the CORSET stop detectors is 178 mm \times 68 mm, covering an angular acceptance of $\pm 14.2^\circ$ in the horizontal plane and $\pm 5.5^\circ$ in the vertical plane. Beam monitors were at 8.9° from the beam axis and at ~ 630 mm from the target. The used target is a 30 $\mu\text{g}/\text{cm}^2$ thick aluminum oxide foil used as backing with a 157 $\mu\text{g}/\text{cm}^2$ thick layer of ^{112}Sn placed at 90° with respect to the beam axis in the symmetric geometry and 132° with respect to the beam axis in the asymmetric geometry. In Figure 2.5 it is illustrated the geometry of the CORSET setup (symmetric configuration) for the present experiment.

The two different CORSET configuration have been used to change the intensity between the observed reaction mechanisms and get more insight on the FF mass distribution. Figure 2.6 shows, as example, the calculated angular correlation for the $^{64}\text{Zn} + ^{112}\text{Sn}$ reaction at $E_{\text{lab}} = 280$ between the two fragments in the case of elastic scattering and FF for three different mass ratios, $A_1/A_2 = 1, 2, 3$ (and their inverse). The two black frames in figure delimit the angular coverage of the two CORSET detectors in the two different configurations. The symmetric configuration, compared to the asymmetric one, has a larger kinematic efficiency for larger mass ratios and smaller kinematic efficiency for the symmetric split and for elastic scattering.

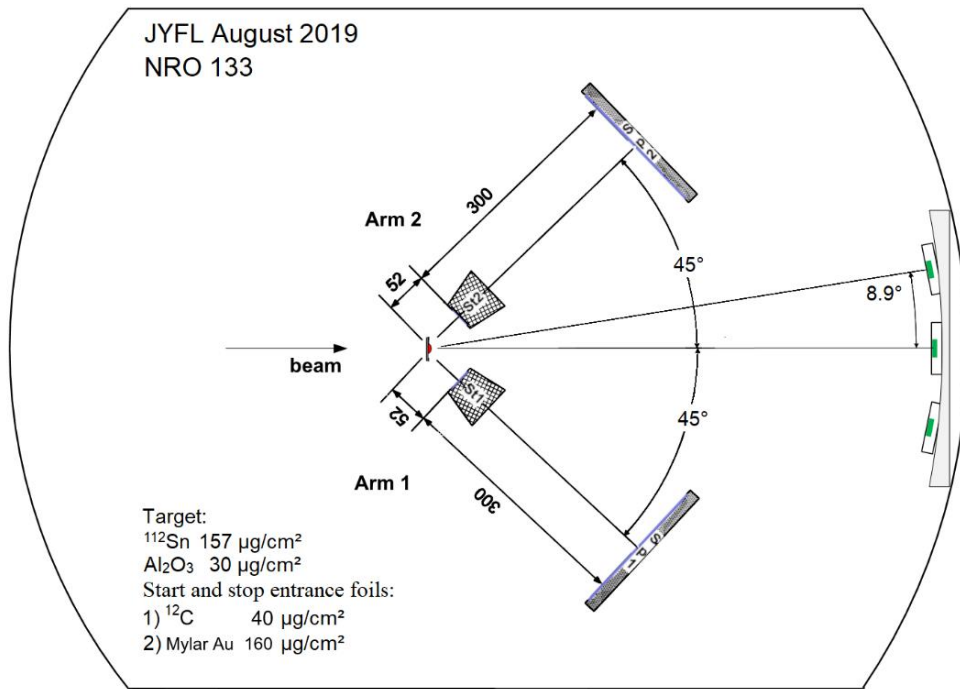


Fig 2.5 Geometry for the CORSET setup (symmetric configuration) for the present experiment. In the bottom left corner are illustrated the characteristic of the target and of the start and stop foils.

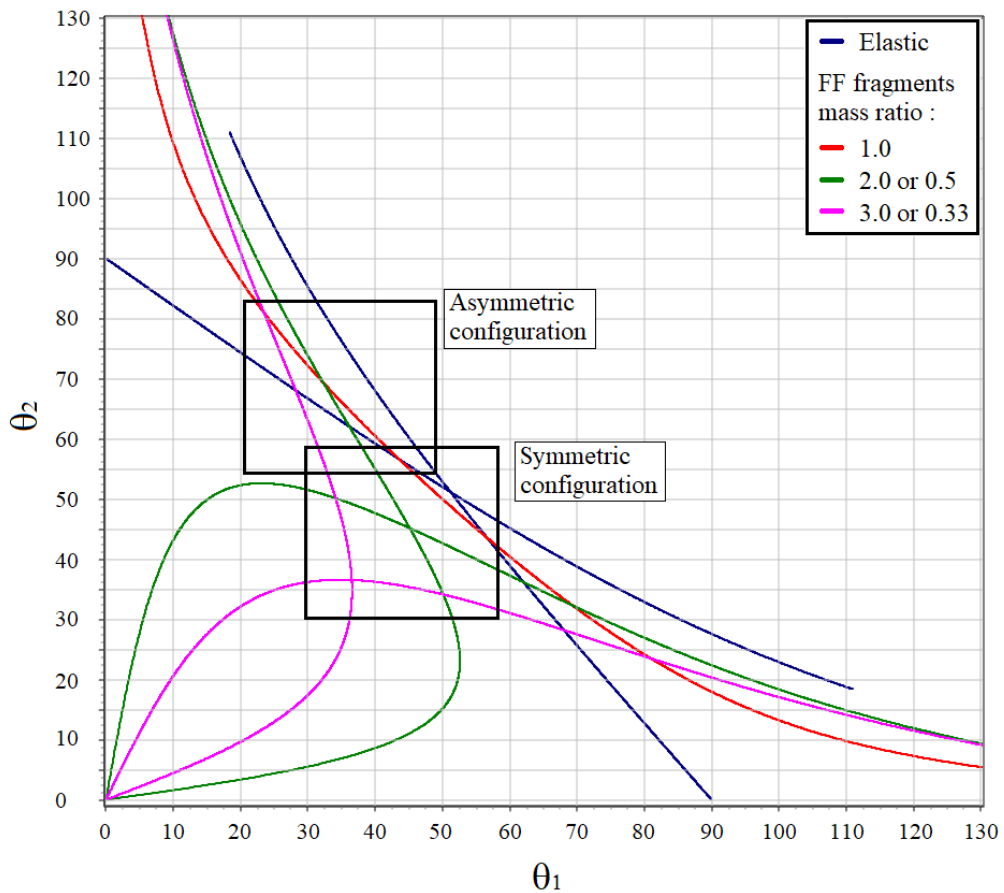


Fig 2.6 Calculated angular correlation for the $^{64}\text{Zn} + ^{112}\text{Sn}$ reaction at $E_{\text{lab}} = 280$ between the two fragments in the case of elastic scattering, blue solid line, and FF for three different mass ratios, $A_1/A_2 = 1, 2, 3$ (and their inverse), respectively red, green and pink solid lines. The two black frames delimit the angular coverage of the two CORSET detectors in the two different configurations.

2.2.2 Electronics and trigger

The circuit diagram of the double-arm ToF spectrometer is shown in Figure 2.7. The time and coordinate signals from the start and stop detectors (St1, St2, Sp1, Sp2, X1, Y1, X2, and Y2) are fed into constant-fraction discriminators (CFDs). Then, signals St1, St2, Sp1, and Sp2 arrive to the logic modules, which generate an output signal (a trigger) if there are two stop signals and at least one start signal.

The start and stop signals come to time-to-amplitude converters (TACs) and then to analog-to-digital converters (ADCs). These converters are used to measure the following time intervals:

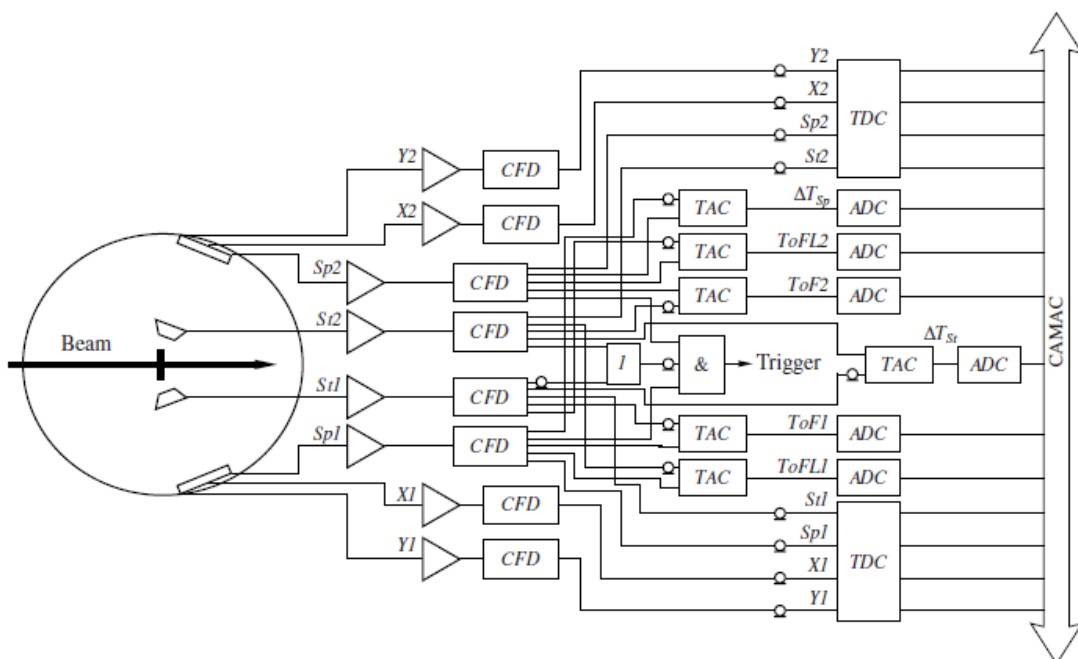


Fig 2.7 Block diagram of the double-arm ToF spectrometer. [26]

- ToF1 between the arrival of signals St1 and Sp1,
- ToF2 between the arrival of signals St2 and Sp2,
- ΔT_{st} between the arrival of signals St1 and St2,
- ΔT_{sp} between the arrival of signals Sp1 and Sp2.

The start and stop signals, as well as the coordinate signals, are independently transmitted via delay lines to a time-to-digital converter (TDC). The trigger signal acts as the start signal for the TDC. The TDC is used to measure the time intervals between the trigger and all the other signals. The coordinate signals are extracted from the

difference between two time intervals: the interval between that coordinate signal and the trigger; the interval between the stop signal and the trigger.

Used modules include ORTEC CFDs, mod. 935, and TACs, mod. 566; CAEN ADC, mod. V785, and TDC, mod. V775; Mesytec ADC, mod. MADC-32; SIS GmbH scaler SIS3800; commercial NIM modules (such as preamplifiers, delay generators, logic units, FIFO, trigger box, NIM/ECL translators).

During the processing of a signal the ADCs and TDCs prevent the electronics to accept new trigger with a busy signal used as a veto for further trigger. The dead time, defined as the number of refused triggers to the number of total trigger ratio, is returned by the electronics.

2.2.3 CORSET time calibration

The time calibration consists in the calibration of both TAC and TDC electronic modules. A Time Calibrator module is plugged into the TACs and TDCs, providing a series of equally distant (in time) peaks used for the evaluation of the slope of the linear calibration.

Since the position information is extracted from time measurements, the TDC channels for X, Y, Start and Stop are separately calibrated and their slope is used to convert position raw data in time. The intercept in the position calibration is obtained through the presence of at least two points on the detector surface whose position is well-known (along X and Y axis): in many cases a mask with some known positions is put in front of the sensitive area (e.g. a plastic reticule in front of CORSET Stop) while, in absence of this tool, the edges of the detector are used.

ToFs may be measured by the difference Stop-Start (TDC channels) or by means of a TAC. In both cases, the difference $S_p - S_t$ from TDC and the output of TAC+ADC chain provide a spectrum in which a known peak may be used to find the intercept of the linear calibration. Usually the known peak is the one related to elastic scattering of the projectile on target and specific calibration runs are conducted. Another option is to use, whenever possible, elastic scattering peaks of both projectile and target to perform a 2-point linear calibration.

2.3 Results and discussion

2.3.1 Selection of binary reaction channels

ToF data along with position information are used to measure the velocity vector of each fragment: given the impact point of the particle on the stop detector, under the hypothesis that the fragments originate in the center of the target, it is possible to reconstruct event-by-event the trajectory length of each fragment and, hence, its velocity vector.

Thus, event-by-event it is possible to apply the momentum and mass number conservation laws to obtain the mass and energy distribution of the fragments. Given the two conservation laws

$$M_{proj}\vec{V}_{proj} = M_1\vec{V}_1 + M_2\vec{V}_2 \quad [2.1]$$

$$M_{proj} + M_{tar} = M_1 + M_2 + M_n \quad [2.2]$$

where $M_{1,2}$ and $\vec{V}_{1,2}$ are the masses and velocity vectors of the two products and M_n is the multiplicity of preequilibrium neutrons, and projecting Equation 2.1 onto the beam axis, it is possible to extract the two masses as following:

$$M_1 = \frac{(M_{proj} + M_{tar} - M_n)V_2\sin\theta_2}{V_1\sin\theta_1 + V_2\sin\theta_2} \quad [2.3]$$

$$M_2 = M_{proj} + M_{tar} - M_1 - M_n \quad [2.4]$$

where $\theta_{1,2}$ is the angle between the velocity vectors of the fragments and the beam axis.

The TKE, as defined by Equation 1.11, is obtained as:

$$TKE = 0.5183 M_1 V_{1,CM}^2 + 0.5183 M_2 V_{2,CM}^2 \quad [2.5]$$

where the factor 0.5183 is a modification to the classical kinetic energy formula, applied in order to match masses in atomic units and velocities in cm/ns into energies in MeV. Hence, it is possible to obtain the Total Kinetic Energy Loss (TKEL), namely the difference between the available kinetic energy in center of mass reference frame and the TKE of the fragments, as:

$$TKEL = E_{CM} - TKE \quad [2.6]$$

TKEL represents the amount of energy dissipated during the interaction.

After the first mass-energy extraction, a correction for energy loss in both target and start detectors is necessary. This is done by means of a recursive algorithm [27] that estimates the energy losses of the fragments passing through matter and recalculates at each step their masses and velocities until a given tolerance is reached.

The hypothesis that the fragments originate in the center of the target introduces an uncertainty on the reconstructed trajectory lengths and, therefore, on the masses. Being the diameter of the used targets ~ 1 cm, the error introduced on the masses is lower than 1 u (lower than the CORSET resolution of 3 u), and so negligible.

It is worthwhile to note that the fragments that arrive in the CORSET detector are secondary fragments, i.e. after the emission of few neutrons. Under the hypothesis that the emission of few neutrons does not affect sensibly (due to the ratio between the neutron mass and the fragment mass) the velocity vector (in terms of its direction and modulus) of the emitting fragment, the reconstruction method allows to obtain the primary fragments mass and energy distributions.

Along with the two masses and TKE, many other useful quantities can be evaluated from the raw data. Some examples are the folding angle, namely the angle between the velocity vectors of the two fragments, and the projections of velocity vectors onto the reaction plane (V_{par}) and orthogonally to it (V_{per}). These two projections are an extremely useful tool in the search for binary Full Momentum Transfer (FMT) events, for which V_{par} is distributed around the center of mass velocity and V_{per} around zero. Figure 2.8 shows a kinematic diagram explaining how the value of V_{par} (V_{\parallel} in figure) can be used to distinguish three different cases:

- a) $V_{\text{par}} = V_{\text{cm}}$, a binary FMT event for which the kinematic reconstruct is well interpreted;
- b) $V_{\text{par}} > V_{\text{cm}}$, the case where (sequential) fission of a fragment (usually the target-like one) occurs and the secondary fragment emitted forward is detected, leading to a misinterpretation of the velocities;
- c) $V_{\text{par}} < V_{\text{cm}}$, similar to the previous but the secondary fragment emitted backward is detected.

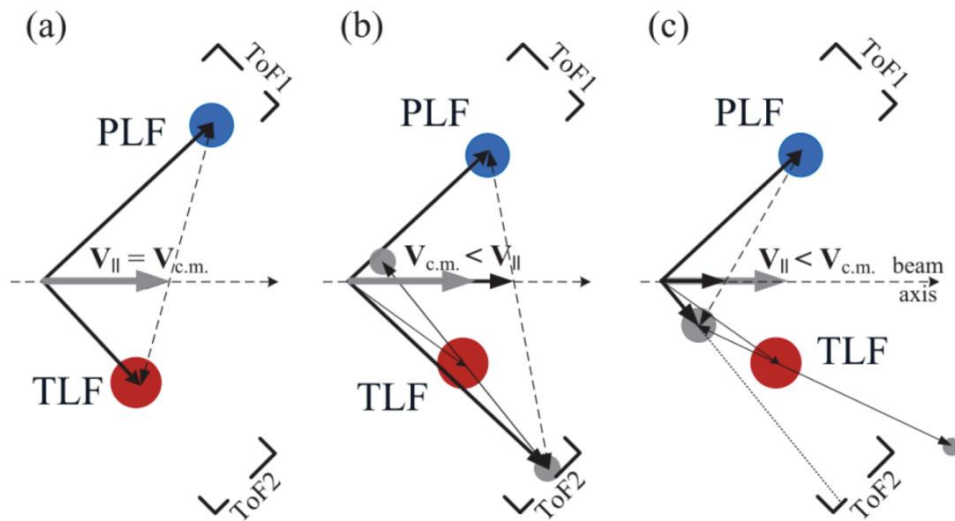


Fig 2.8 Kinematic Diagram, useful to tell if an event is a binary FMT or a sequential fission. (a) $V_{\text{par}} = V_{\text{c.m.}}$, a binary FMT event; (b) $V_{\text{par}} > V_{\text{c.m.}}$, (sequential) fission of a fragment and the secondary fragment emitted forward is detected; (c) $V_{\text{par}} < V_{\text{c.m.}}$, similar to the previous but the secondary fragment emitted backward is detected [28].

2.3.2 Mass-TKE distributions

Figure 2.9 shows the experimental $V_{\text{par}} - V_{\text{per}}$ matrix for the $^{68}\text{Zn} + ^{112}\text{Sn}$ reaction at $E_{\text{lab}} = 300$ MeV. The most populated spot lies in region with V_{per} distributed around zero and V_{par} around the center of mass velocity (1.10 cm/ns in this reaction) and a gate around this spot is used to select the FMT events.

The angular correlation of the two fragments provides a useful tool to check the correct application of the presented selection method. For a binary FMT event, the two detected fragments recoil at 180° with respect to each other in the center of mass reference frame. Figure 2.10 a) shows the experimental matrix of the x and y folding angles ($Fold_{x,CM}$ and $Fold_{y,CM}$ in Figure). After the application of the condition on the velocities, the only remaining events are the ones around 180° on both axes, as shows in Figure 2.10 b).

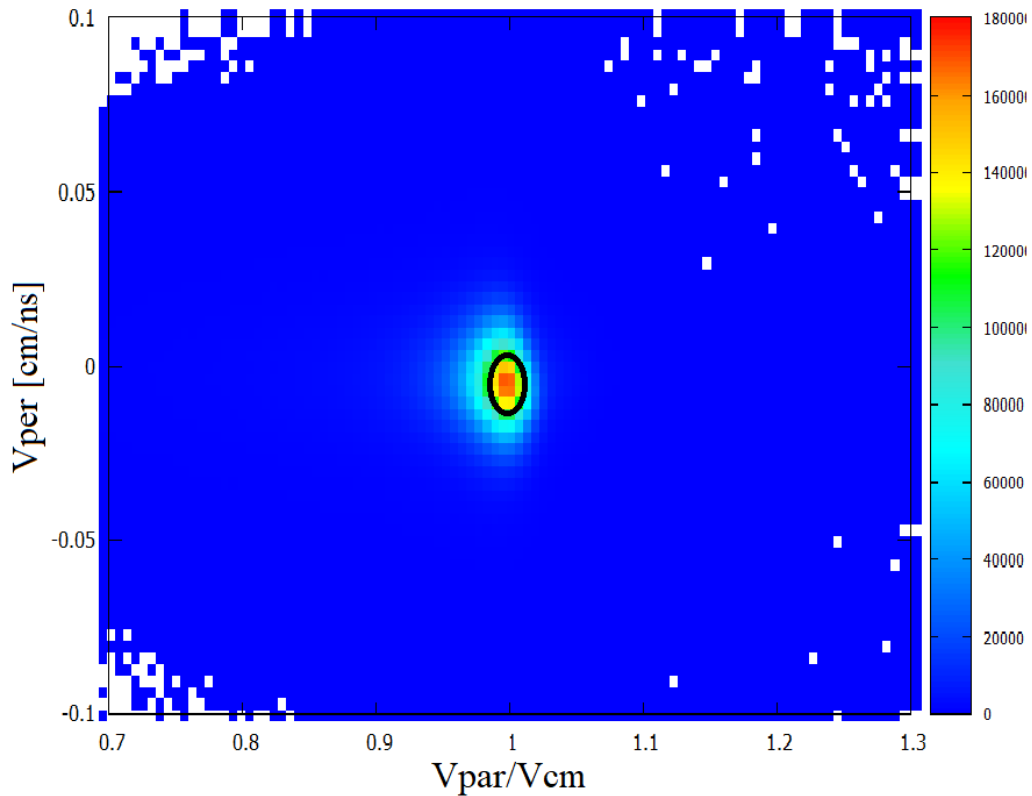


Fig 2.9 Experimental $V_{\text{par}} - V_{\text{per}}$ matrix for the $^{68}\text{Zn} + ^{112}\text{Sn}$ reaction at $E_{\text{lab}} = 300$ MeV. The most populated spot lies in region with V_{per} distributed around zero and V_{par} around the center of mass velocity (1.10 cm/ns). The black circle represents the gate used to select the binary FMT events.

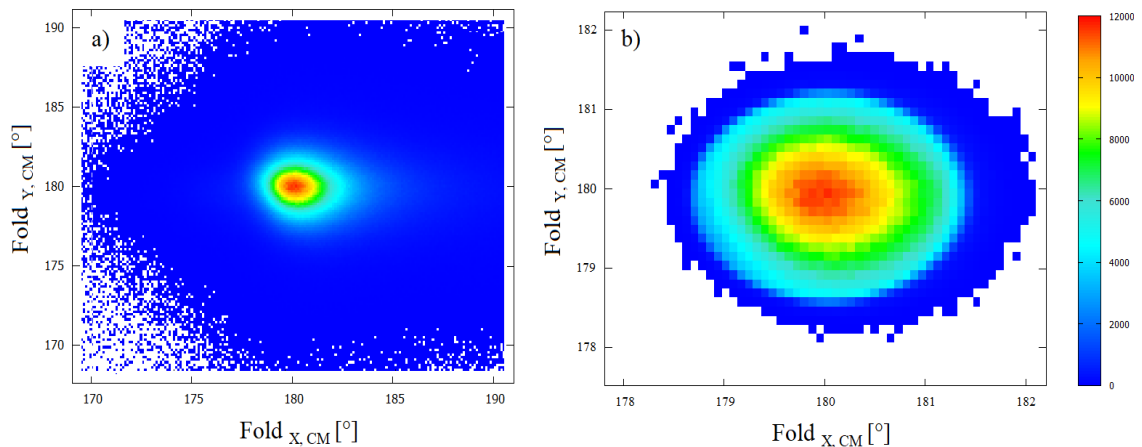


Fig 2.10 Experimental $Fold_{x,CM}$ and $Fold_{y,CM}$ matrix for the $^{68}\text{Zn} + ^{112}\text{Sn}$ reaction at $E_{\text{lab}} = 300$ MeV a) without conditions and b) with the selection of FMT events

The symmetrized mass-TKE matrix obtained for the $^{68}\text{Zn} + ^{112}\text{Sn}$ reaction at $E_{\text{lab}} = 300$ MeV (leading, if fusion occurs, to ^{180}Hg at $E^* = 82$ MeV) after the application of the mentioned gate is shown Figure 2.11. The most populated regions of the matrix lie in correspondence of the elastic masses (68 and 112 u, respectively) and the center of mass energy (187 MeV). This can be seen from the mass and TKE distributions,

obtained as projections of the mass-TKE matrix presented, shown respectively in Figures 2.12 and 2.13. The markers highlight the elastic masses and energy. The events around these regions can be confidently attributed to elastic and quasi-elastic scattering. With decreasing TKE, the contribution of FF increases up to the maximum expected in coincidence of the Viola TKE, 142 MeV for the present reaction, according to Equation 1.12.

The experimental $V_{\text{par}} - V_{\text{per}}$ and symmetrized mass-TKE matrices for the other reactions are shown in Figures from 2.14 to 2.19. The mass-TKE matrices for the $^{64}\text{Zn} + ^{112}\text{Sn}$ reaction at $E_{\text{lab}} = 280, 265$ MeV with asymmetric detection geometry (Fig 2.17 and 2.19) show a more pronounced elastic component, as expected according to Fig 2.6.

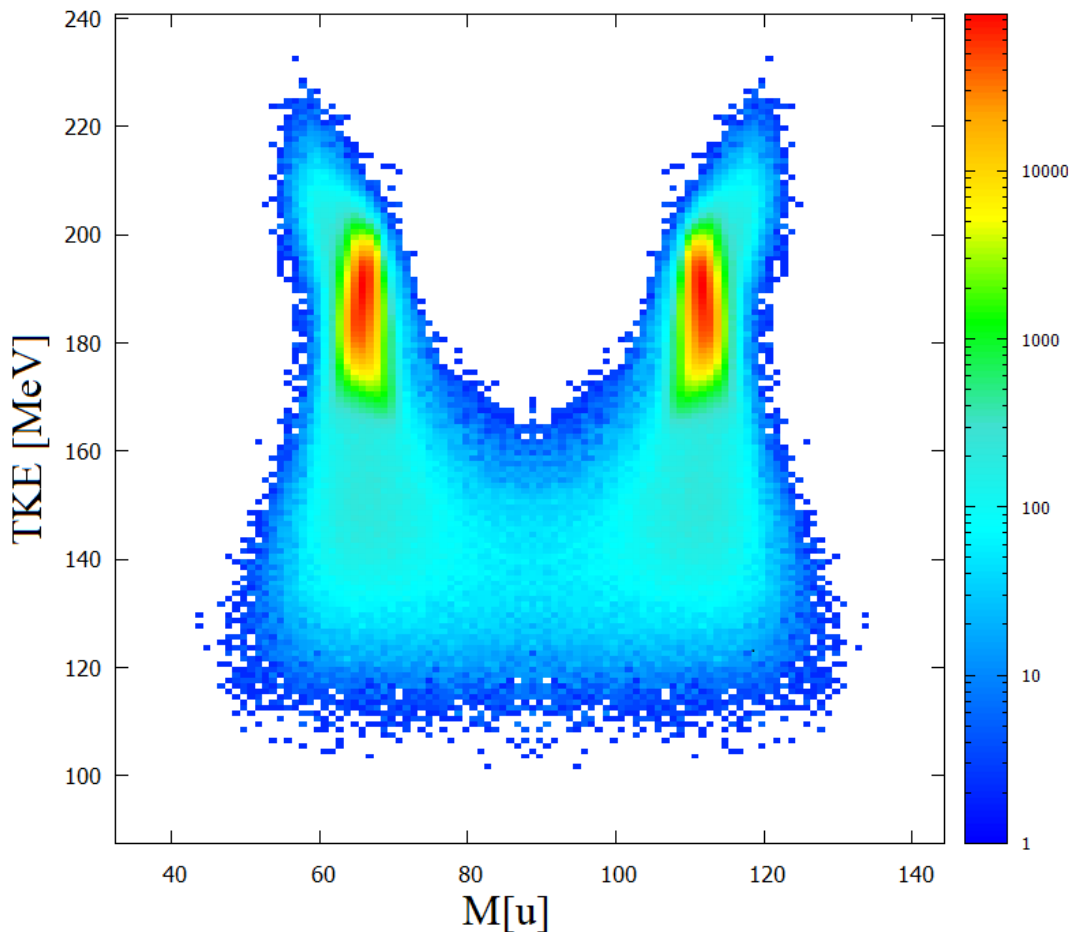


Fig 2.11 Mass-TKE distribution of binary FMT products for the $^{68}\text{Zn} + ^{112}\text{Sn}$ reaction at $E_{\text{lab}} = 300$ MeV.

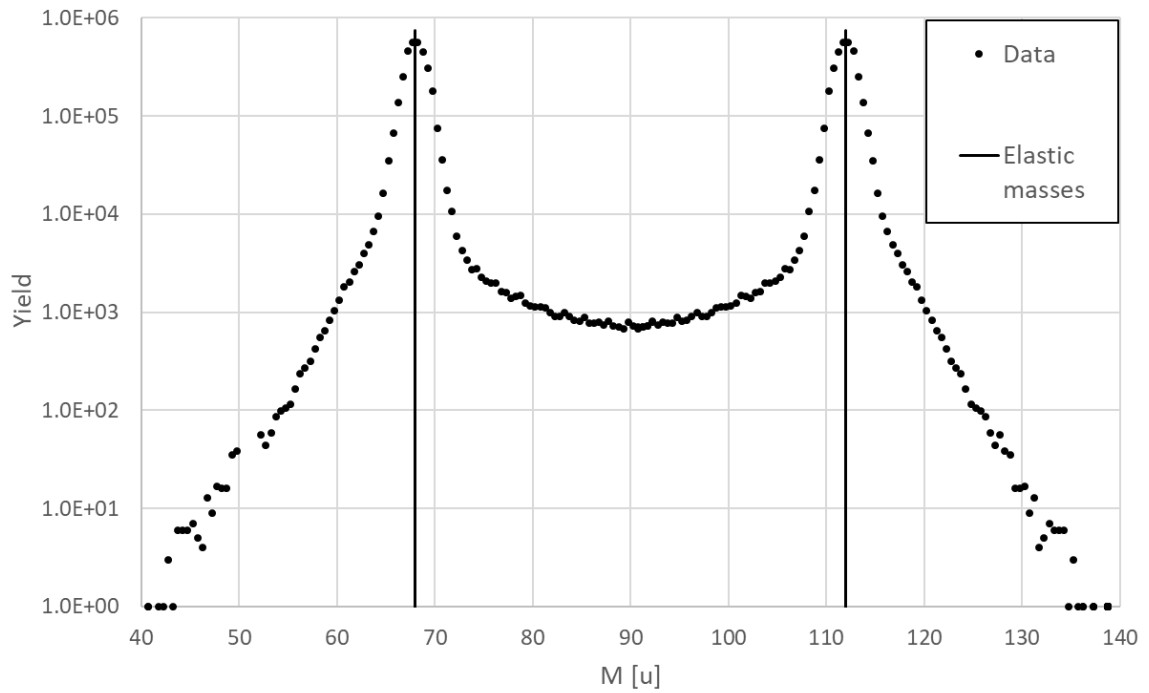


Fig 2.12 Mass distribution of binary FMT products. The markers highlight the masses of projectile and target (68 and 112 u).

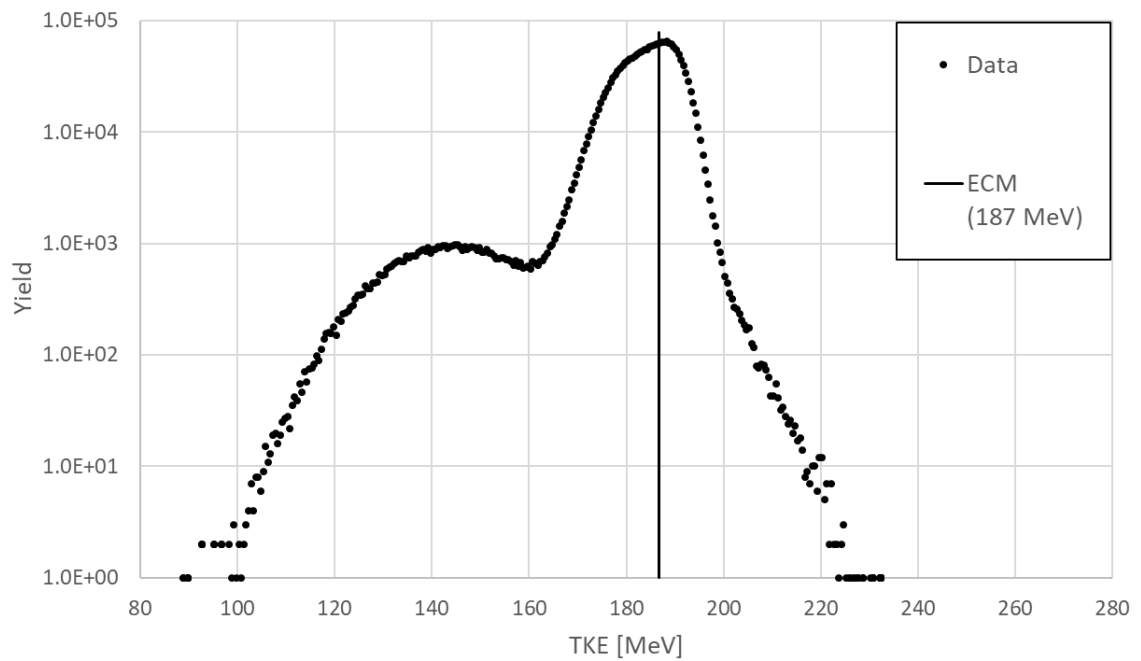


Fig 2.13 TKE distribution of binary FMT products. The marker highlights the bombarding energy in the center of mass reference frame (187 MeV).

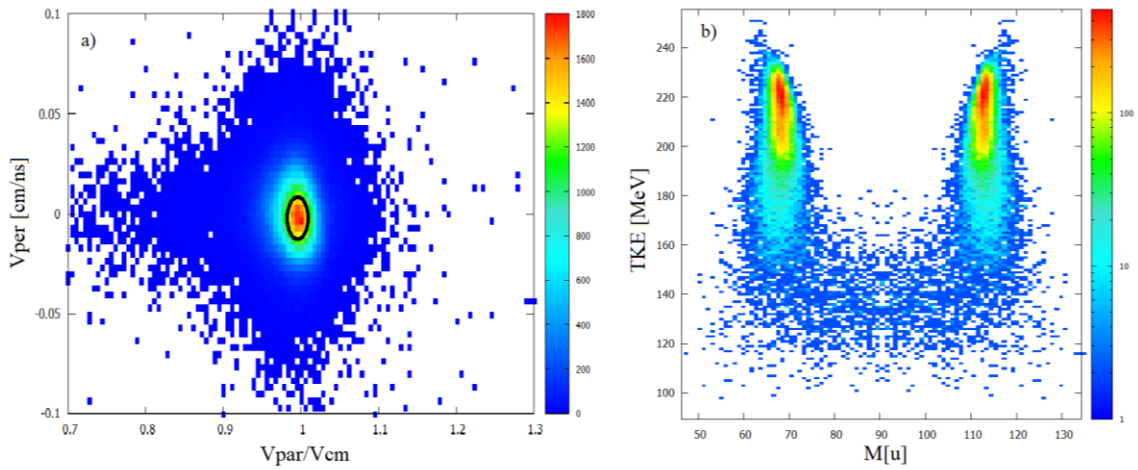


Fig 2.14 a) Experimental $V_{\text{par}} - V_{\text{per}}$ matrix and b) mass-TKE distribution of binary products in the $^{68}\text{Zn} + ^{112}\text{Sn}$ reaction at $E_{\text{lab}} = 355$ MeV.

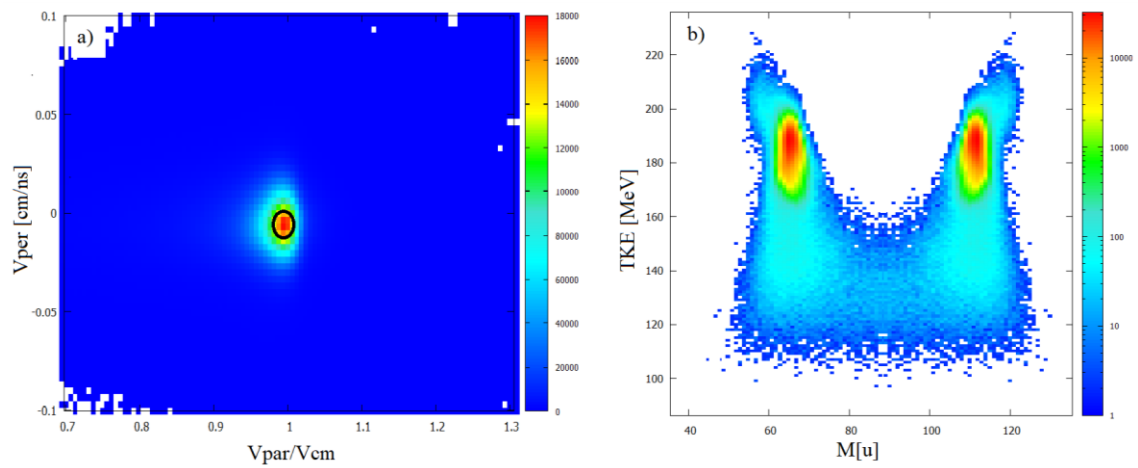


Fig 2.15 a) Experimental $V_{\text{par}} - V_{\text{per}}$ matrix and b) mass-TKE distribution of binary products in the $^{64}\text{Zn} + ^{112}\text{Sn}$ reaction at $E_{\text{lab}} = 300$ MeV.

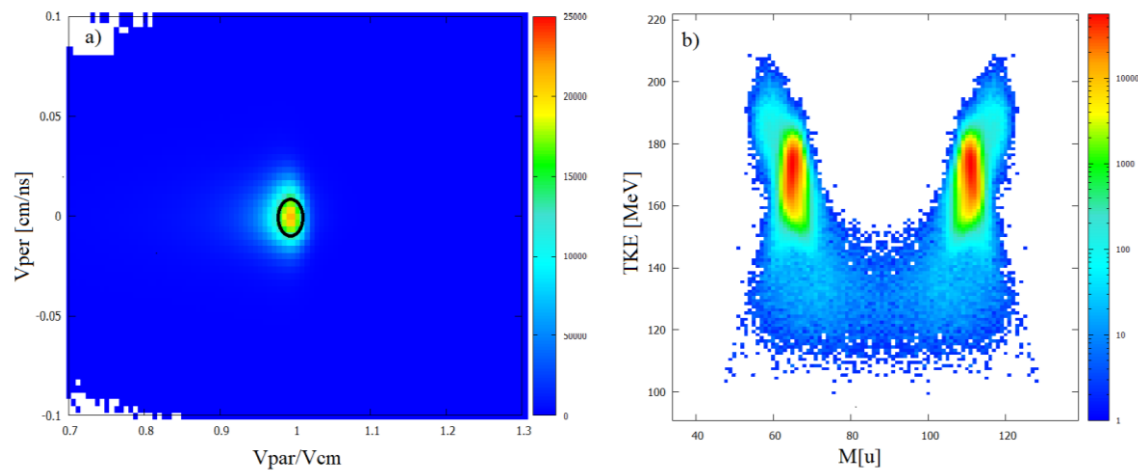


Fig 2.16 a) Experimental $V_{\text{par}} - V_{\text{per}}$ matrix and b) mass-TKE distribution of binary products in the $^{64}\text{Zn} + ^{112}\text{Sn}$ reaction at $E_{\text{lab}} = 280$ MeV.

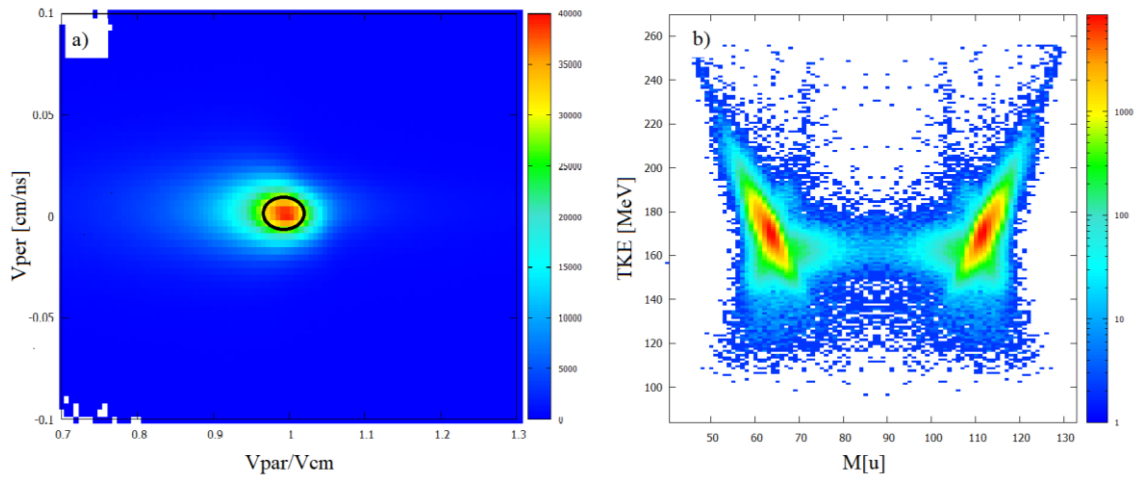


Fig 2.17 a) Experimental $V_{\text{par}} - V_{\text{per}}$ matrix and b) mass-TKE distribution of binary products in the $^{64}\text{Zn} + ^{112}\text{Sn}$ reaction at $E_{\text{lab}} = 280$ MeV with asymmetric detection geometry.

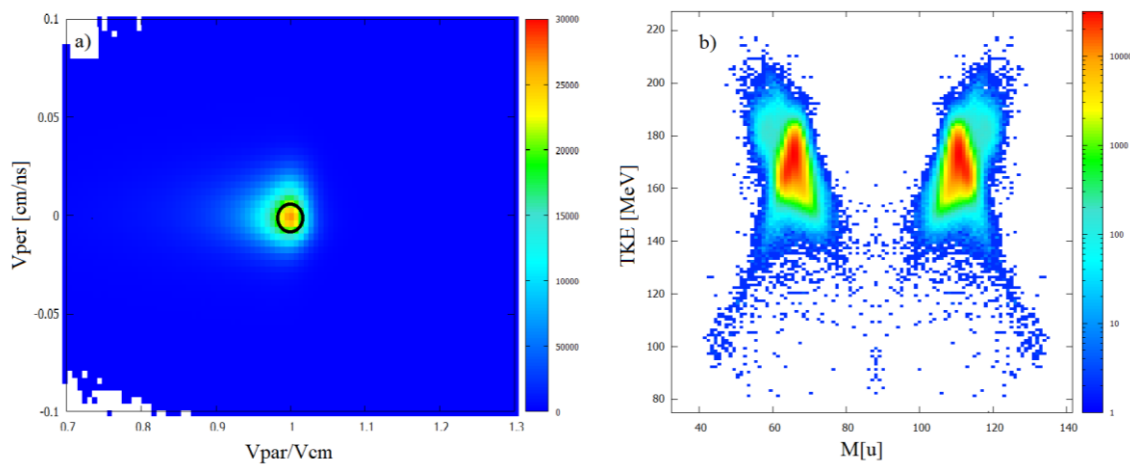


Fig 2.18 a) Experimental $V_{\text{par}} - V_{\text{per}}$ matrix and b) mass-TKE distribution of binary products in the $^{64}\text{Zn} + ^{112}\text{Sn}$ reaction at $E_{\text{lab}} = 265$ MeV.

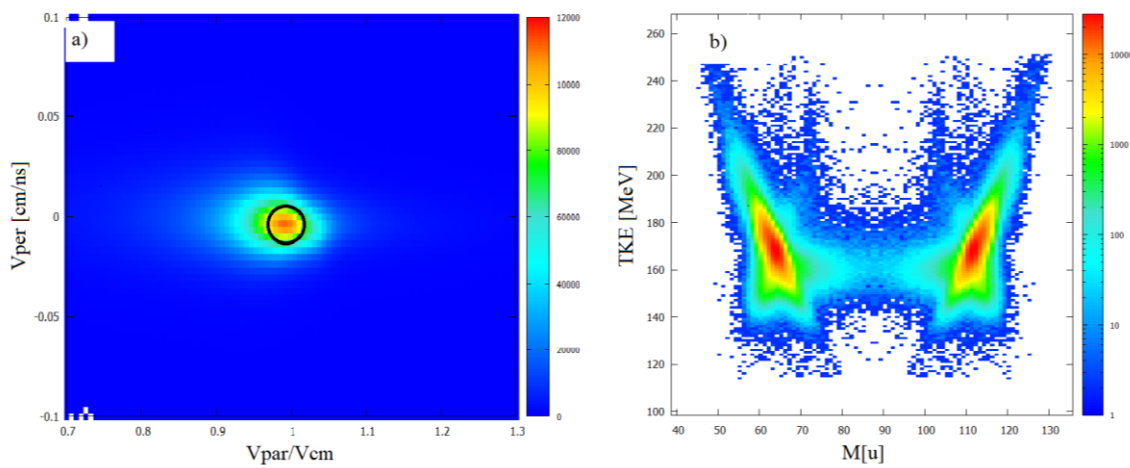


Fig 2.19 a) Experimental $V_{\text{par}} - V_{\text{per}}$ matrix and b) mass-TKE distribution of binary products in the $^{64}\text{Zn} + ^{112}\text{Sn}$ reaction at $E_{\text{lab}} = 265$ MeV with asymmetric detection geometry.

2.3.3 Selection of fusion-fission events

The aim of the present work is to measure the FF mass distribution of the two Hg isotopes, with a closer look at the asymmetric component. Due to the large symmetry in the entrance channels, the mass-TKE matrices do not allow a clear separation of the contributions of the elastic and quasi-elastic components from the asymmetric FF one.

The TKE (or similarly the TKEL) can help in the separation of the two mechanisms, as FF is expected to be the most dissipative process, so the one with higher TKEL. Figure 2.20 shows the TKEL for the $^{68}\text{Zn} + ^{112}\text{Sn}$ reaction at $E_{\text{lab}} = 300$ MeV (leading to ^{180}Hg at $E_{\text{CN}}^* = 48$ MeV) empirically decomposed in 4 different Gaussians. The first Gaussian is centered around $\text{TKEL} = 0$ that, according to Equation 2.6, means $\text{TKE} = E_{\text{CM}}$ and corresponds to the elastic component. The second and third Gaussians, centered around $\text{TKEL} \approx 7$ and ≈ 20 MeV, can be ascribed to quasi elastic and inelastic components. Those processes usually have an expected TKEL lower than ~ 30 MeV. The fourth Gaussian is centered at $\text{TKEL} = 43$ MeV and marks the most dissipative process. It is in correspondence of the TKE expected for symmetric FF mass split, therefore it is reasonable to ascribe this component of the TKEL spectrum to the FF process.

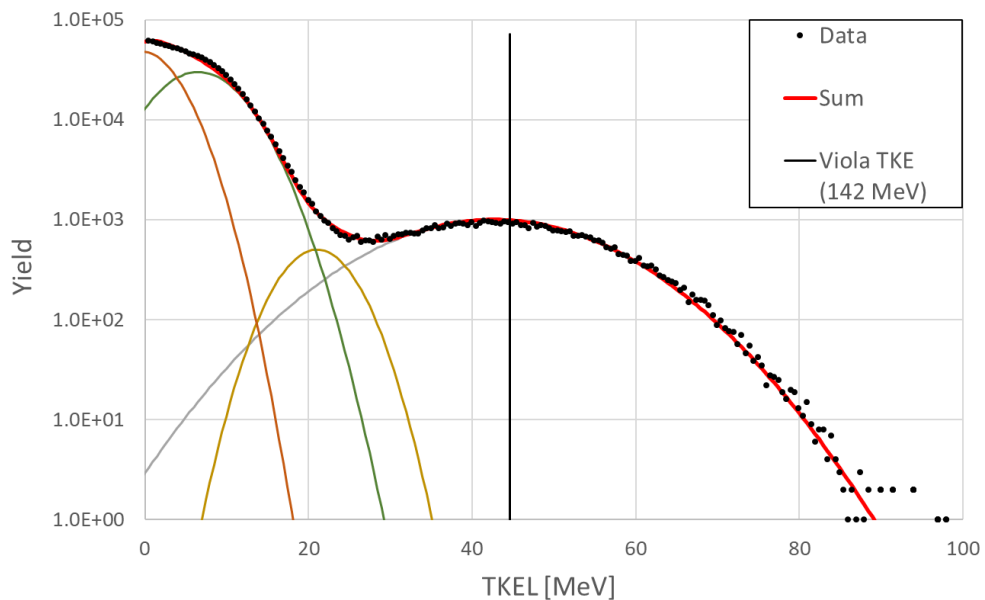


Fig 2.20 Experimental TKEL distribution of binary FMT products for the $^{68}\text{Zn} + ^{112}\text{Sn}$ reaction at $E_{\text{lab}} = 300$ MeV. The experimental data have been decomposed in 4 different Gaussians: the first one, centered around E_{CM} corresponds to the elastic component; the second and third ones, centered around ~ 7 and ~ 21 MeV can be ascribed to quasi elastic and inelastic components; the fourth one, as the most dissipative process, can be ascribed to FF component. The red curve is the sum of the four different Gaussians. The marker highlights the TKEL in correspondence of the Viola TKE for symmetric mass split (142 MeV).

The effect of the selection of different windows of TKEL is shown in Figure 2.21. The experimental mass distributions of primary TLF are shown for different ranges of TKEL: blue curve for TKEL in the range $35 \div 40$ MeV, orange curve for $40 \div 45$ MeV, green curve for $45 \div 55$ MeV and yellow curve for $55 \div 70$. Intervals have been chosen to have distributions with comparable amount of counts. The trend that emerges is an increasing relative yield of the symmetric component of the mass distribution as the TKEL increases.

An analogous trend is present in the other reactions. The experimental TKEL and mass distributions for the other reactions are shown in Figures from 2.22 to 2.26. Results for the $^{64}\text{Zn} + ^{112}\text{Sn}$ reaction at $E_{\text{lab}} = 265$ MeV with asymmetric detection geometry are not shown as the statistics in the FF region was not sufficient for a detailed analysis. This is due to the presence of a predominant elastic component in the mass-TKE matrix that hinders an unambiguous separation of the FF component.

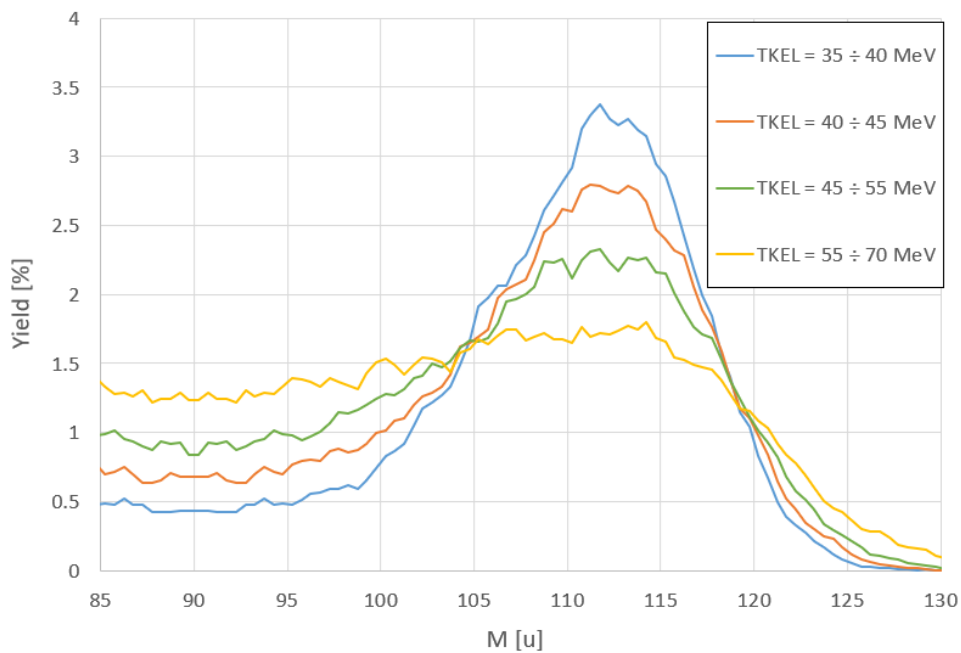


Fig 2.21 Experimental mass distribution of binary FMT products for the $^{68}\text{Zn} + ^{112}\text{Sn}$ reaction at $E_{\text{lab}} = 300$ MeV for different windows in TKEL: blue curve correspond to TKEL in the window $35 \div 40$ MeV, orange curve $40 \div 45$ MeV, green curve $45 \div 55$ MeV, yellow curve $55 \div 70$. Intervals have been chosen to have a comparable counting statistics.

$^{68}\text{Zn} + ^{112}\text{Sn}$ at $E_{\text{lab}} = 355 \text{ MeV}$ leading to ^{180}Hg at $E_{\text{CN}}^* = 82 \text{ MeV}$

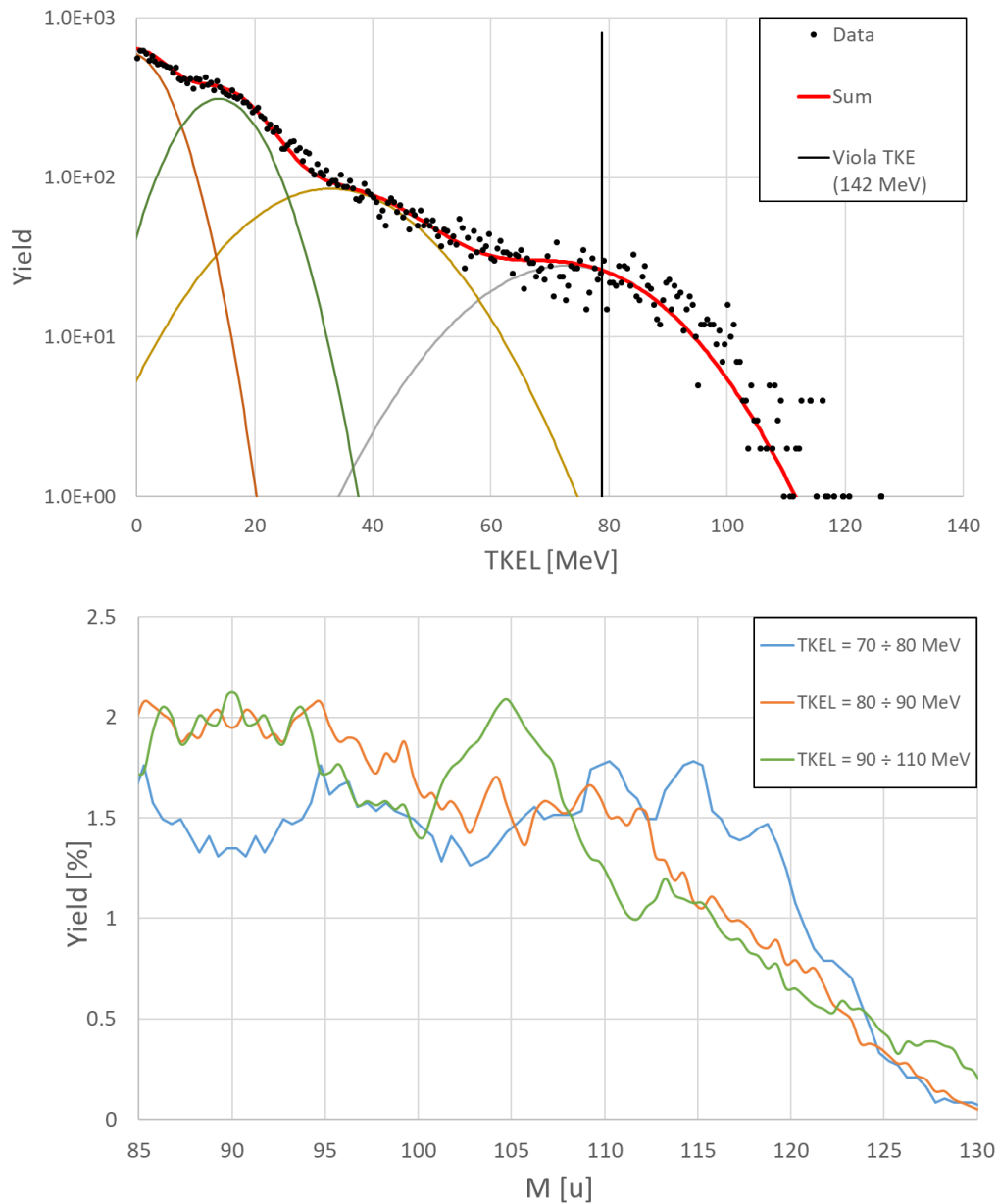


Fig 2.22 (Top) Experimental TKEL distribution of binary FMT products for the $^{68}\text{Zn} + ^{112}\text{Sn}$ reaction at $E_{\text{lab}} = 355 \text{ MeV}$. The experimental data have been decomposed in 4 different Gaussians: the first one, centered around E_{CM} corresponds to the elastic component; the second and third ones, centered around ~ 14 and $\sim 33 \text{ MeV}$ can be ascribed to quasi elastic and inelastic components; the fourth one, as the most dissipative process, can be ascribed to FF component. The red curve is the sum of the four different Gaussians. The marker highlights the TKEL in correspondence of the Viola TKE for symmetric mass split (142 MeV).

(Bottom) Experimental mass distribution of binary FMT products for different windows in TKEL: blue curve correspond to TKEL in the window $70 \div 80 \text{ MeV}$, orange curve $80 \div 90 \text{ MeV}$, green curve $90 \div 110 \text{ MeV}$. Intervals have been chosen to have a comparable counting statistics.

$^{64}\text{Zn} + ^{112}\text{Sn}$ at $E_{\text{lab}} = 300 \text{ MeV}$ leading to ^{176}Hg at $E_{\text{CN}}^* = 48 \text{ MeV}$

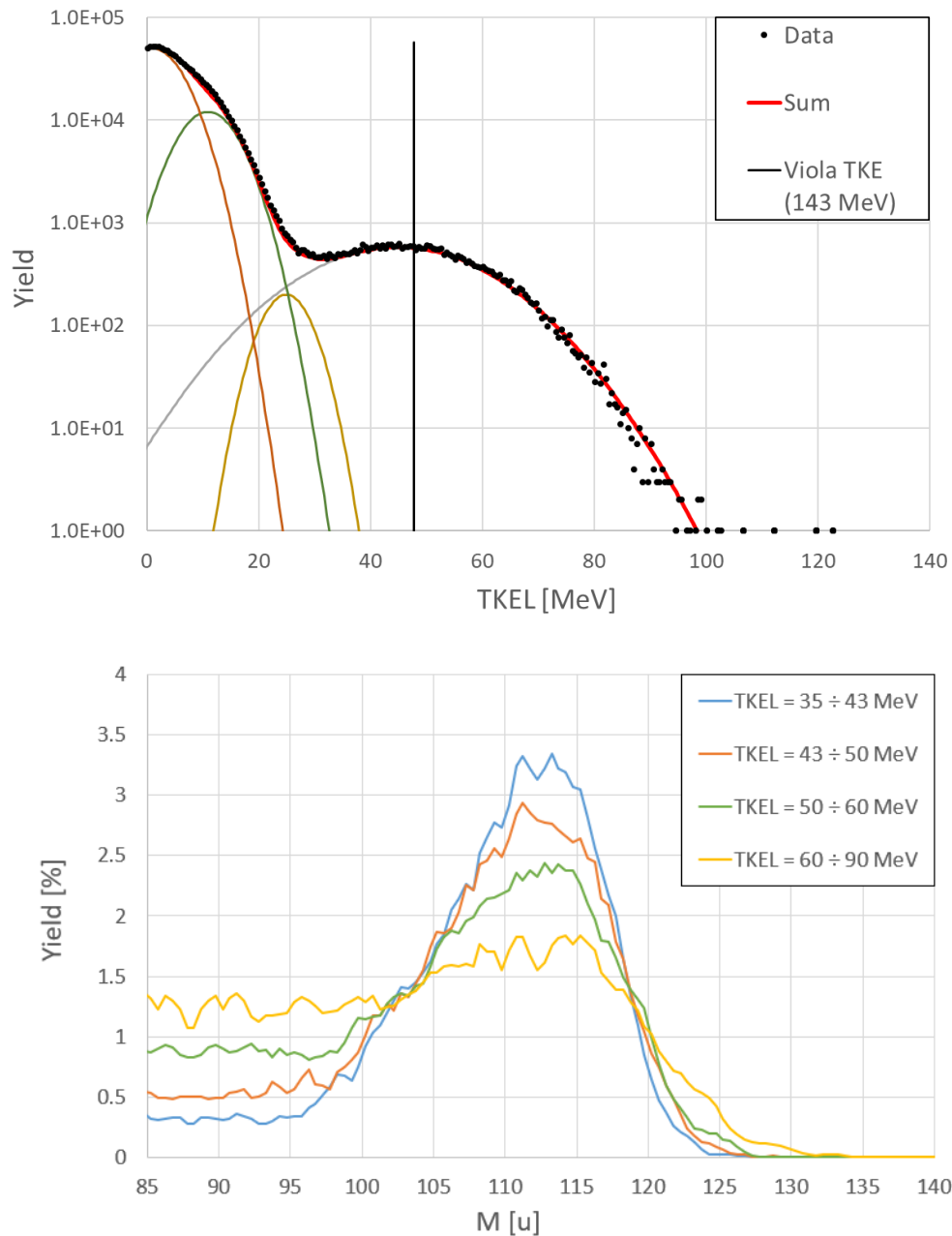


Fig 2.23 (Top) Experimental TKEL distribution of binary FMT products for the $^{64}\text{Zn} + ^{112}\text{Sn}$ reaction at $E_{\text{lab}} = 300 \text{ MeV}$. The experimental data have been decomposed in 4 different Gaussians: the first one, centered around E_{CM} corresponds to the elastic component; the second and third ones, centered around ~ 11 and $\sim 25 \text{ MeV}$ can be ascribed to quasi elastic and inelastic components; the fourth one, as the most dissipative process, can be ascribed to FF component. The red curve is the sum of the four different Gaussians. The marker highlights the TKEL in correspondence of the Viola TKE for symmetric mass split (143 MeV).

(Bottom) Experimental mass distribution of binary FMT products for different windows in TKEL: blue curve correspond to TKEL in the window 35 ÷ 43 MeV, orange curve 43 ÷ 50 MeV, green curve 50 ÷ 60 MeV, yellow curve 60 ÷ 90 MeV. Intervals have been chosen to have a comparable counting statistics.

$^{64}\text{Zn} + ^{112}\text{Sn}$ at $E_{\text{lab}} = 280 \text{ MeV}$ (symmetric CORSET geometry) leading to ^{176}Hg at $E_{\text{CN}}^* = 35 \text{ MeV}$

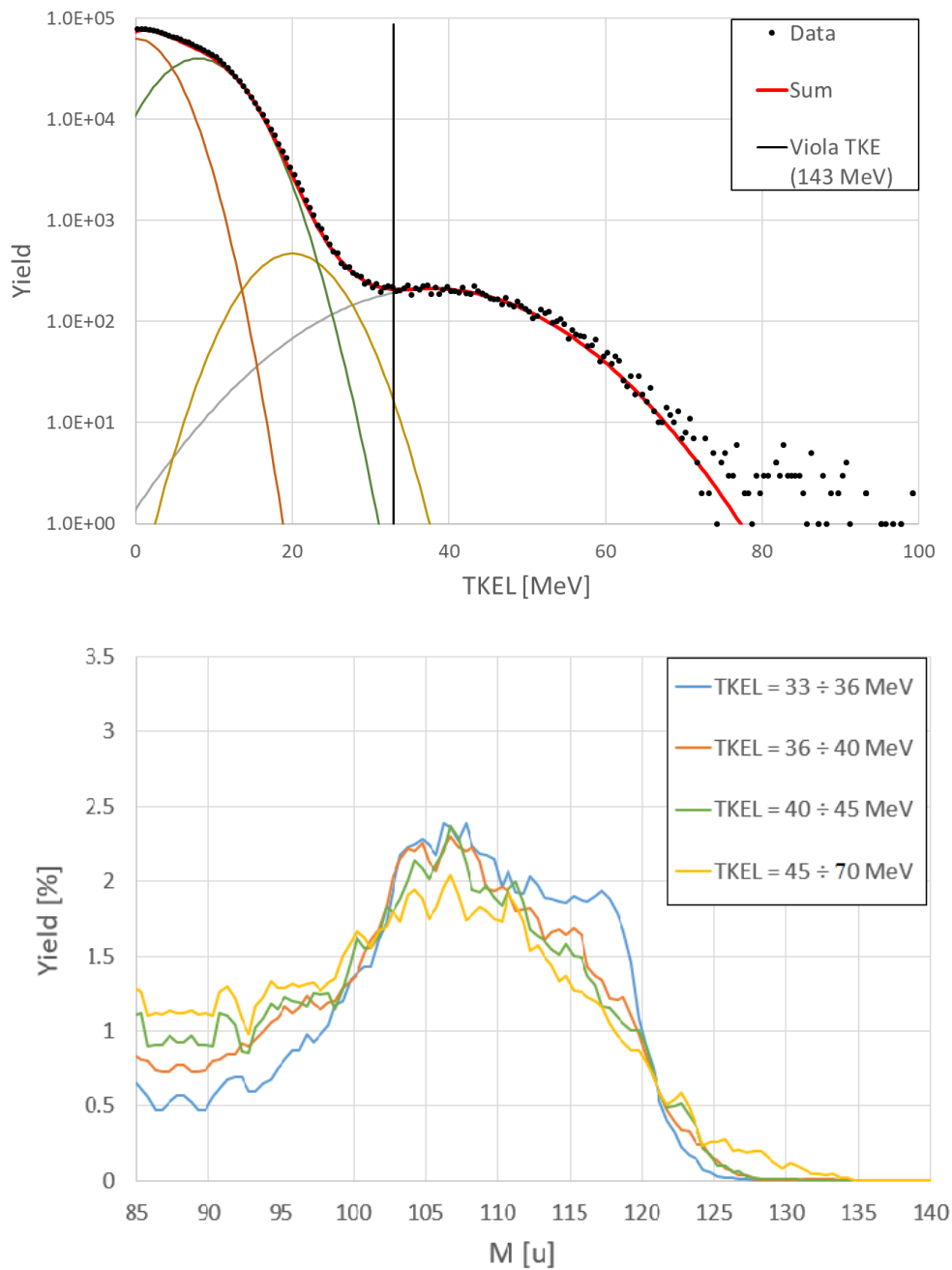


Fig 2.24 (Top) Experimental TKEL distribution of binary FMT products for the $^{64}\text{Zn} + ^{112}\text{Sn}$ reaction at $E_{\text{lab}} = 280 \text{ MeV}$. The experimental data have been decomposed in 4 different Gaussians: the first one, centered around E_{CM} corresponds to the elastic component; the second and third ones, centered around ~ 8 and $\sim 20 \text{ MeV}$ can be ascribed to quasi elastic and inelastic components; the fourth one, as the most dissipative process, can be ascribed to FF component. The red curve is the sum of the four different Gaussians. The marker highlights the TKEL in correspondence of the Viola TKE for symmetric mass split (143 MeV).

(Bottom) Experimental mass distribution of binary FMT products for different windows in TKEL: blue curve correspond to TKEL in the window 33 ÷ 36 MeV, orange curve 36 ÷ 40 MeV, green curve 40 ÷ 45 MeV, yellow curve 45 ÷ 70 MeV. Intervals have been chosen to have a comparable counting statistics.

$^{64}\text{Zn} + ^{112}\text{Sn}$ at $E_{\text{lab}} = 280 \text{ MeV}$ (asymmetric CORSET geometry) leading to ^{176}Hg at $E_{\text{CN}}^* = 35 \text{ MeV}$

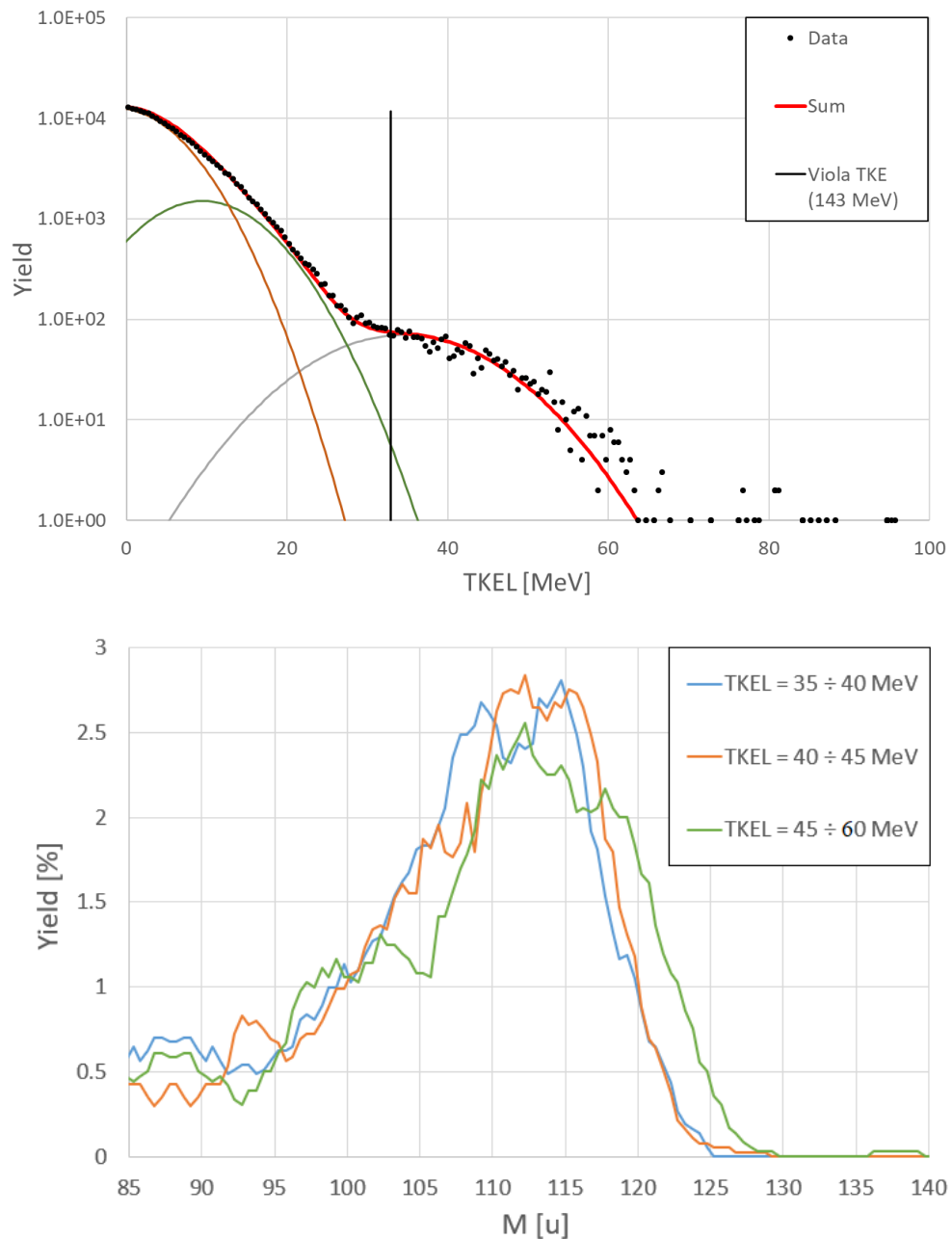


Fig 2.25 (Top) Experimental TKEL distribution of binary FMT products for the $^{64}\text{Zn} + ^{112}\text{Sn}$ reaction at $E_{\text{lab}} = 280 \text{ MeV}$ in the asymmetric geometry. The experimental data have been decomposed in 3 different Gaussians: the first one, centered around E_{CM} corresponds to the elastic component; the second one, centered around $\sim 10 \text{ MeV}$ can be ascribed to quasi elastic and inelastic components; the third one, as the most dissipative process, can be ascribed to FF component. The red curve is the sum of the three different Gaussians. The marker highlights the TKEL in correspondence of the Viola TKE for symmetric mass split (143 MeV).

(Bottom) Experimental mass distribution of binary FMT products for different windows in TKEL: blue curve correspond to TKEL in the window 35 ÷ 40 MeV, orange curve 40 ÷ 45 MeV, green curve 45 ÷ 60 MeV. Intervals have been chosen to have a comparable counting statistics.

$^{64}\text{Zn} + ^{112}\text{Sn}$ at $E_{\text{lab}} = 265 \text{ MeV}$ (symmetric CORSET geometry) leading to ^{176}Hg at $E_{\text{CN}}^* = 25 \text{ MeV}$

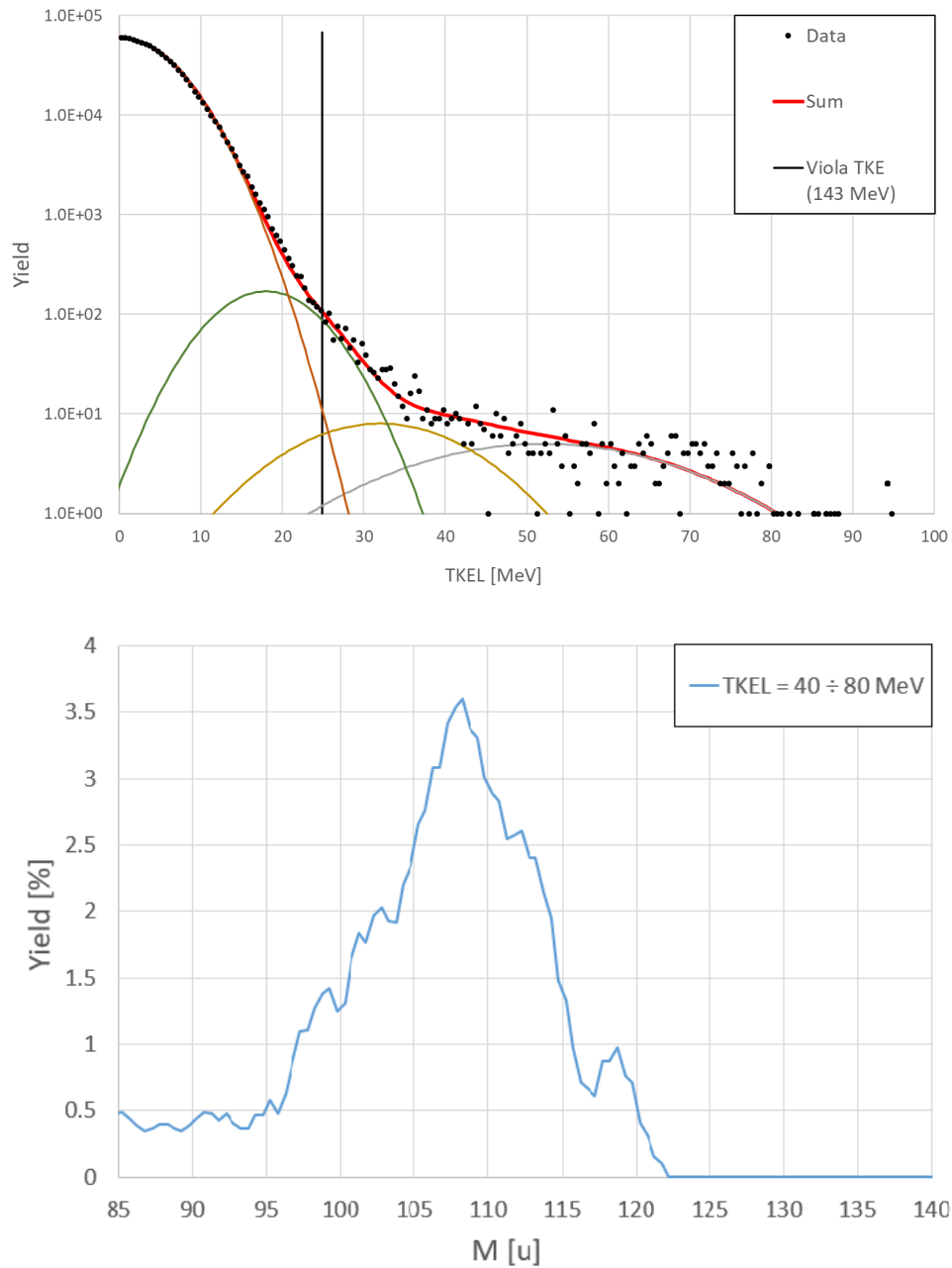


Fig 2.26 (Top) Experimental TKEL distribution of binary FMT products for the $^{64}\text{Zn} + ^{112}\text{Sn}$ reaction at $E_{\text{lab}} = 265 \text{ MeV}$. The experimental data have been decomposed in 4 different Gaussians: the first one, centered around E_{CM} corresponds to the elastic component. The identification of the other Gaussians is more uncertain, but it is reasonable to ascribe to FF the events after 40 MeV of TKEL. The red curve is the sum of the four different Gaussians. The marker highlights the TKEL in correspondence of the Viola TKE for symmetric mass split (143 MeV).

(Bottom) Experimental mass distribution of binary FMT products for TKEL in the window $40 \div 80 \text{ MeV}$.

2.3.4 Fission modes in $^{180,176}\text{Hg}$

Results shown in Figures from 2.21 to 2.26 are summarized in Figures 2.27 and 2.28. Figures 2.27 and 2.28 show the experimental symmetric-yield to peak-yield ratio for different values of TKEL for the CN ^{180}Hg and ^{176}Hg , respectively. The abscissa has been taken as the ratio between the weighted average TKEL of the considered interval and the TKEL corresponding to Viola TKE ($\text{TKEL}_{\text{VIOLA}}$), to compare reactions with different E_{CM} . With increasing TKEL, ^{180}Hg tends to a more symmetric mass split than ^{176}Hg . Moreover, for increasing excitation energy of the CN, ^{180}Hg tends to a more symmetric mass split than ^{176}Hg . This behavior agrees qualitatively with Moller's prediction presented in Figure 2.2, however the fission fragment mass distribution of ^{176}Hg appears to be much more asymmetric than predicted by Moller's calculations. A more detailed analysis follows.

To evaluate the presence of specific fission modes in the experimental data, the mass distributions calculated by Moller and collaborators [25] have been taken as a guideline to search for fission modes. The approach used here is 1) to decompose each computed mass distributions into different Gaussian contributions, each with an average corresponding to a fission mode, and afterwards 2) to attempt to reproduce the full experimental mass distribution with the same fission modes. This method is constrained by the fact that if a fission mode is identified, its average mass cannot change with the excitation energy being it a property of the fissioning nucleus. If found experimentally, it is also a manifestation that such nucleus was indeed formed in the nuclear reaction. This is not always guaranteed being the entrance channel dynamics very important in the fusion process.

As a first step, the calculated mass distributions have been fitted with the sum of three Gaussian contributions: one for symmetric mass mode and two for asymmetric mass mode. A total of three Gaussians are necessary: the lowest mass asymmetric peak, the symmetric peak and the higher mass asymmetric peak. Figure 2.29 shows the decomposition of the calculated mass distributions at three different excitation energies for ^{180}Hg . The best fits have been obtained minimizing the chi-square. Black dots are the calculation provided in ref [25], green line is the symmetric Gaussian component, the two orange lines are the asymmetric Gaussian components, and the red line is the sum of these Gaussians. The first striking unexpected feature is that to properly fit the data the mean of the Gaussian asymmetric contributions moves toward more symmetric

masses as the excitation energy increases. However, this behavior is not compatible with the concept of fission modes: each fission mode is due to a valley in the potential of the CN and its position is independent on the excitation energy of the fissioning nucleus. This indeed is already an indication that to reproduce the computed mass distributions an additional asymmetric fission mode is necessary.

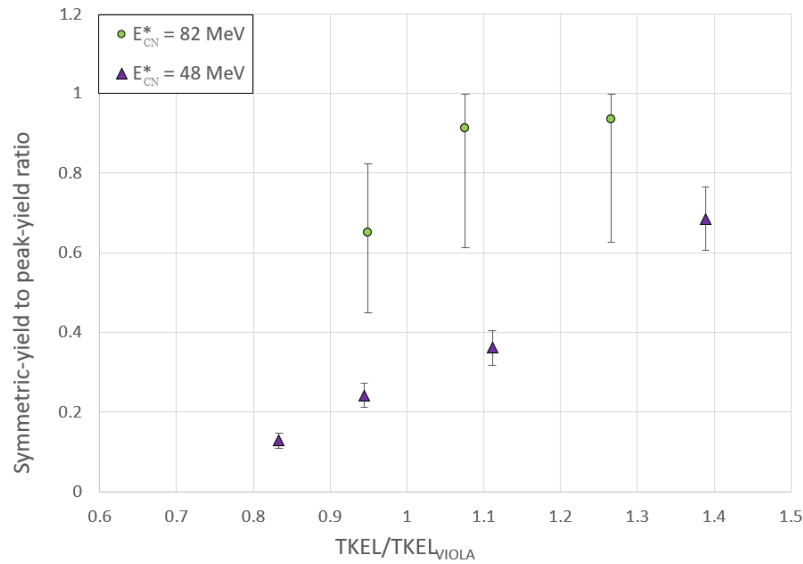


Fig 2.27 Symmetric-yield to peak-yield ratio versus TKEL to Viola TKEL (TKEL_{VIOLA}) ratio for $^{68}\text{Zn} + ^{112}\text{Sn}$ reaction at $E_{\text{lab}} = 355$ and 300 MeV leading respectively to excited ^{180}Hg with $E_{\text{CN}}^* = 82$ (green dots) and 48 MeV (purple triangles).

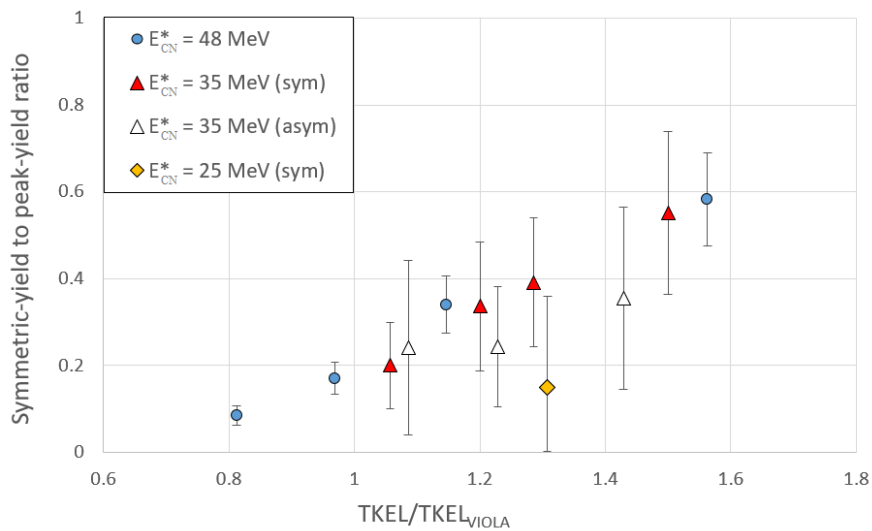


Fig 2.28 Symmetric-yield to peak-yield ratio versus TKEL to Viola TKEL (TKEL_{VIOLA}) ratio for $^{64}\text{Zn} + ^{112}\text{Sn}$ reaction at $E_{\text{lab}} = 300$, 280 and 265 leading respectively to excited ^{176}Hg with $E_{\text{CN}}^* = 48$ (blue dots), 35 (red triangles for symmetric configuration and empty triangles for asymmetric configuration) and 25 MeV (yellow diamonds).

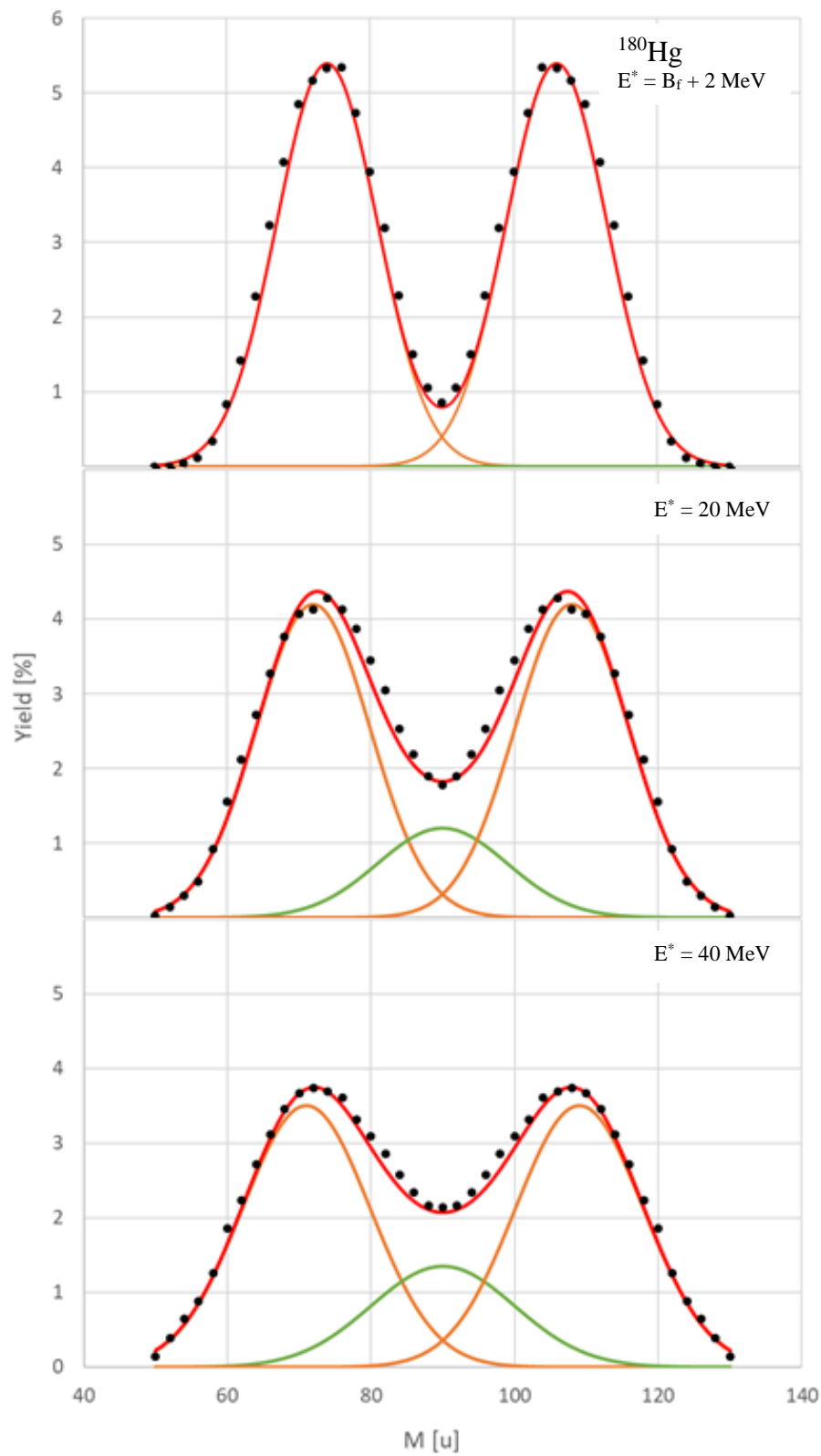


Fig 2.29 Decomposition of the calculated mass distributions for ^{180}Hg [25] (black dots) into the best combination of a symmetric and an asymmetric Gaussian components. Red line is the sum of the Gaussian curves.

The suspect that a third fission mode is occurring appeared well grounded after trying to fit the experimental distributions with only two modes as found in Figure 2.29. In each decomposition, each Gaussian has a fixed average as obtained from the decomposition of the calculated mass distribution with the excitation energy closest to the experimental one. Figure 2.30 shows an example of the experimental mass distribution for the TLF (black dots with error bars) decomposed into two Gaussian contributions (one for symmetric mass split, green line, and one for asymmetric mass split, orange line). Red line is the sum of the Gaussian curves; the blue line is the difference between the red line and the data. What immediately catches the eye is that, with this decomposition, there is a large component of the mass distribution that is not reproduced by these Gaussians. The more asymmetric region, centered around $A = 116$, can be due to QF or DI processes that are not well separated from the FF component. The more symmetric region, centered around $A = 100$ may mark the presence of a third fission mode present in this mass distribution.

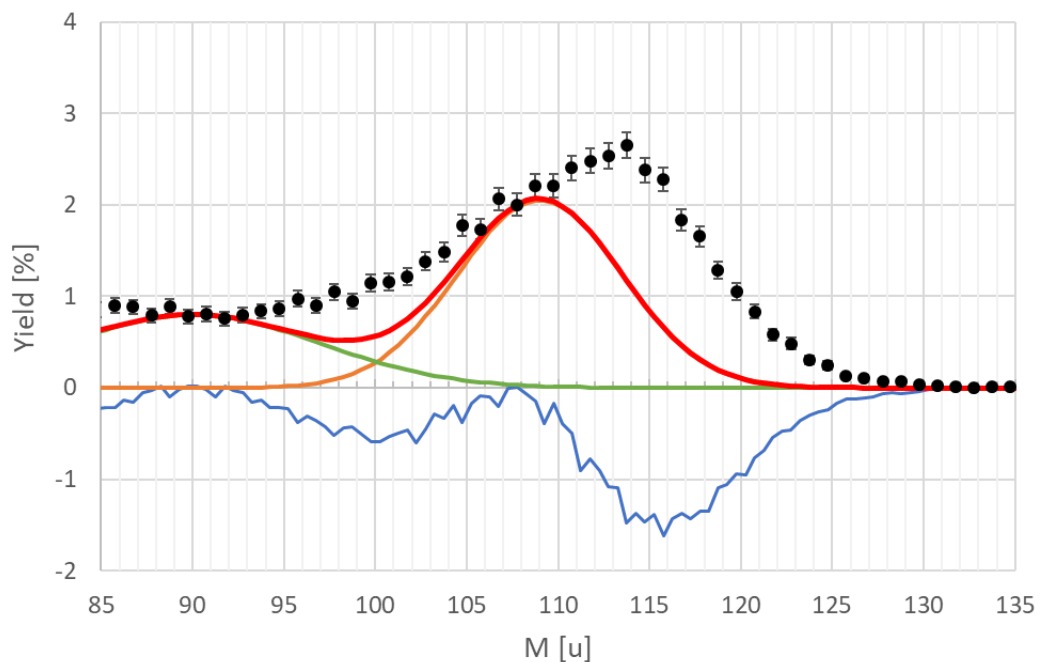


Fig 2.30 Decomposition of the experimental mass distributions of TLF for ^{180}Hg at $E^* = 48$ MeV (black dots with error bars) into a symmetric (green line) and an asymmetric (orange line) component. Red line is the sum of the Gaussian curves, blue line is the difference between the red line and the data.

The mass distributions of the other reactions present similar patterns, reinforcing the idea of the presence of a third fission mode, with $A \sim 99 - 100$. With this scheme in mind, the mass distribution calculated by Moller and collaborators have been decomposed into 3 different Gaussian components, one for symmetric mass split, one

for asymmetric mass split and A of the TLF around 100, one for asymmetric mass split and A of the TLF around 110. Figures 2.31 and 2.32 show the decomposition of the calculated mass distributions respectively for ^{180}Hg and ^{176}Hg and for three excitation energies. With this new decomposition, the three gaussian components maintain the same mean over the different excitation energies while their variance increase with excitation energy. In case of ^{180}Hg , we have the three possible fission modes centered on $A = 90$ for the symmetric split, green curve, on $A = 100$ (and the symmetric $A = 80$) for the asymmetric split, purple curve, and on $A = 109$ (and the symmetric $A = 71$) for the second asymmetric split, orange curve. In case of ^{176}Hg , we have the three possible fission modes centered on $A = 88$ for the symmetric split, green curve, on $A = 99$ (and the symmetric $A = 77$) for the asymmetric split, purple curve, and on $A = 110$ (and the symmetric $A = 66$) for the second asymmetric split, orange curve.

At this point, the experimental mass distributions have been decomposed by using these newly found hypothetical modes. The results are shown in Figures from 2.33 to 2.38. The color legend is analogue to the one in Figures 2.31 and 2.32: black dots with error bars are the experimental data, green curve is the symmetric component, purple curves are the first asymmetric component, orange curves are the second asymmetric component, red curve is the sum of the Gaussian components. An additional blue curve, for most asymmetric masses, represent the component of the mass distribution that, as in Figure 2.30, can be ascribed to QF and DI processes.

With three modes (one symmetrical and two asymmetrical) all the experimental mass distributions are now extremely well reproduced. What is clearly different is the relative contribution of the different modes and their width. The consequences and implications of this finding is discussed in the next session.

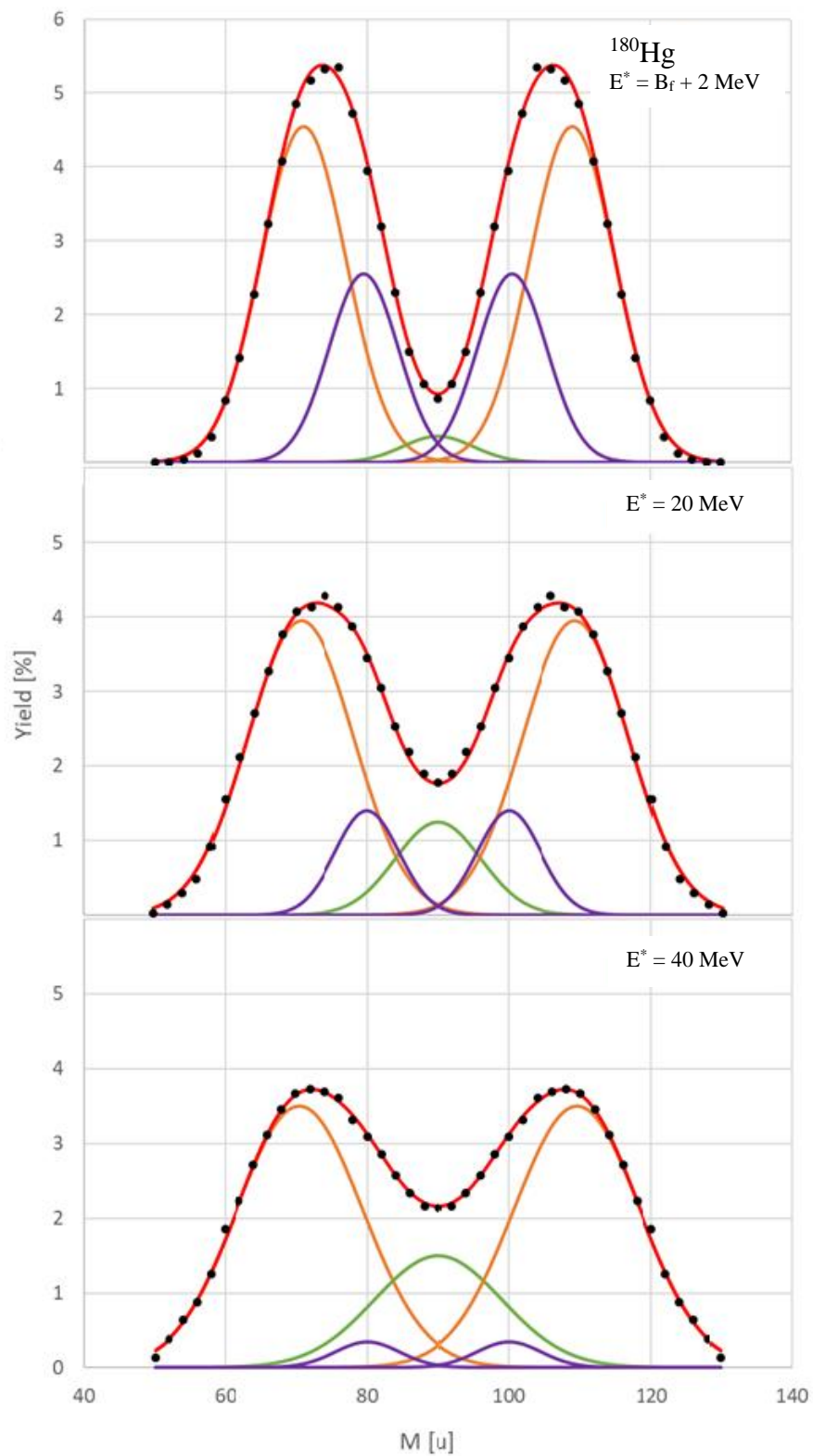


Fig 2.31 Decomposition of the calculated mass distributions for ^{180}Hg [25] (black dots) into the best combination of a symmetric and two asymmetric Gaussian components. Red line is the sum of the Gaussian curves.

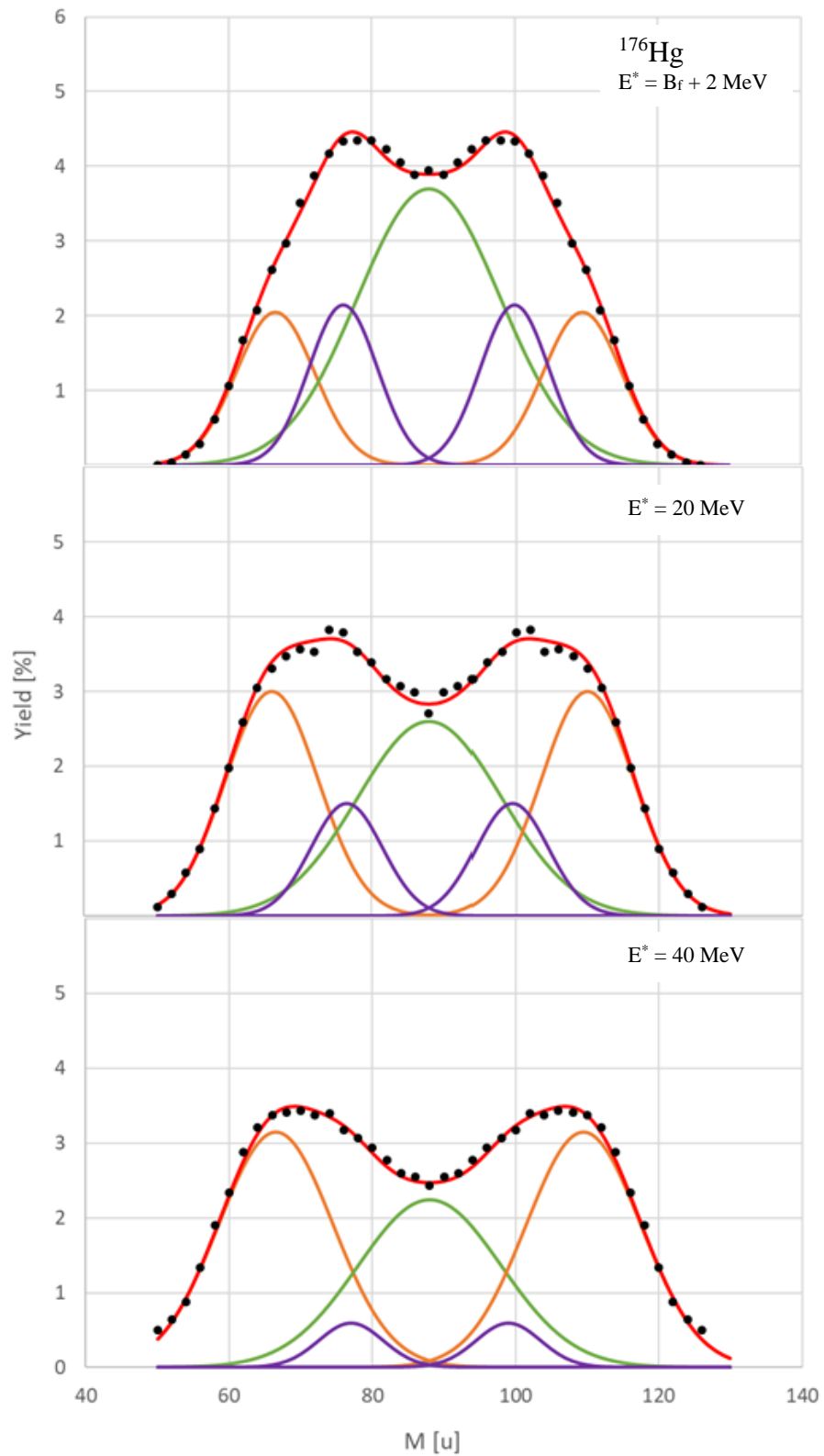


Fig 2.32 Decomposition of the calculated mass distributions for ^{176}Hg [25] (black dots) into the best combination of a symmetric and two asymmetric Gaussian components. Red line is the sum of the Gaussian curves.

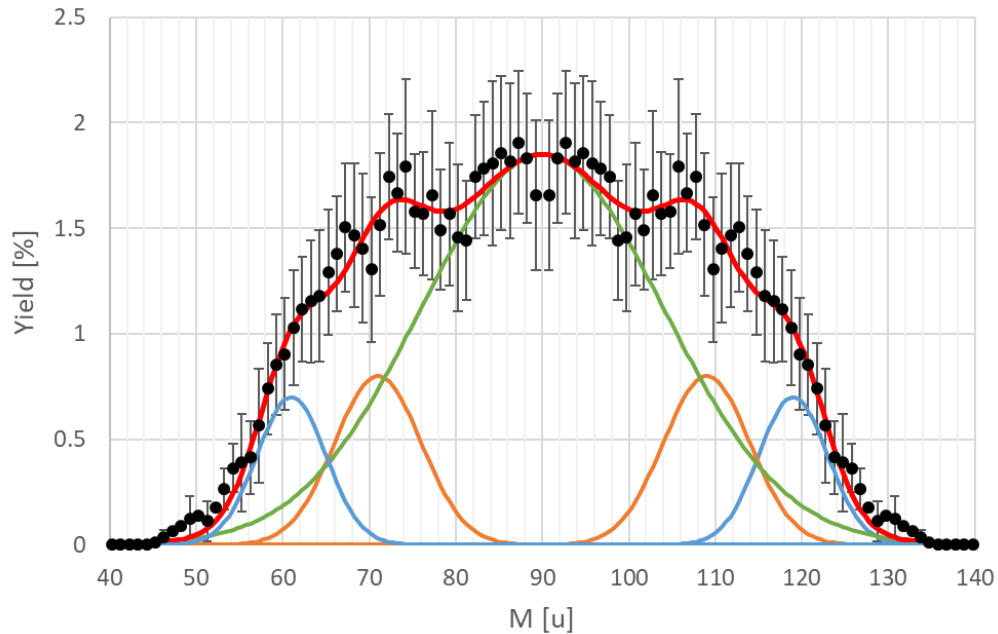
^{180}Hg $E^* = 82 \text{ MeV}$ 

Fig 2.33 Decomposition of the experimental mass distributions for ^{180}Hg at $E^* = 82 \text{ MeV}$ (black dots with error bars) into a symmetric (green line) and two asymmetric (orange and purple lines) components. Red line is the sum of the Gaussian curves.

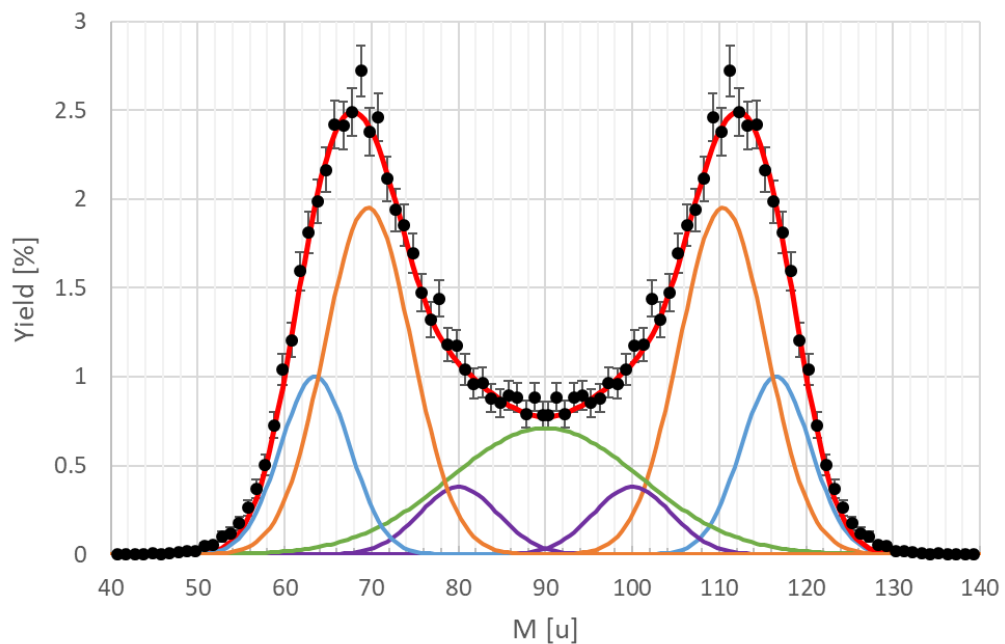
 $E^* = 48 \text{ MeV}$ 

Fig 2.34 Decomposition of the experimental mass distributions for ^{180}Hg at $E^* = 48 \text{ MeV}$ (black dots with error bars) into a symmetric (green line) and two asymmetric (orange and purple lines) components. Red line is the sum of the Gaussian curves.

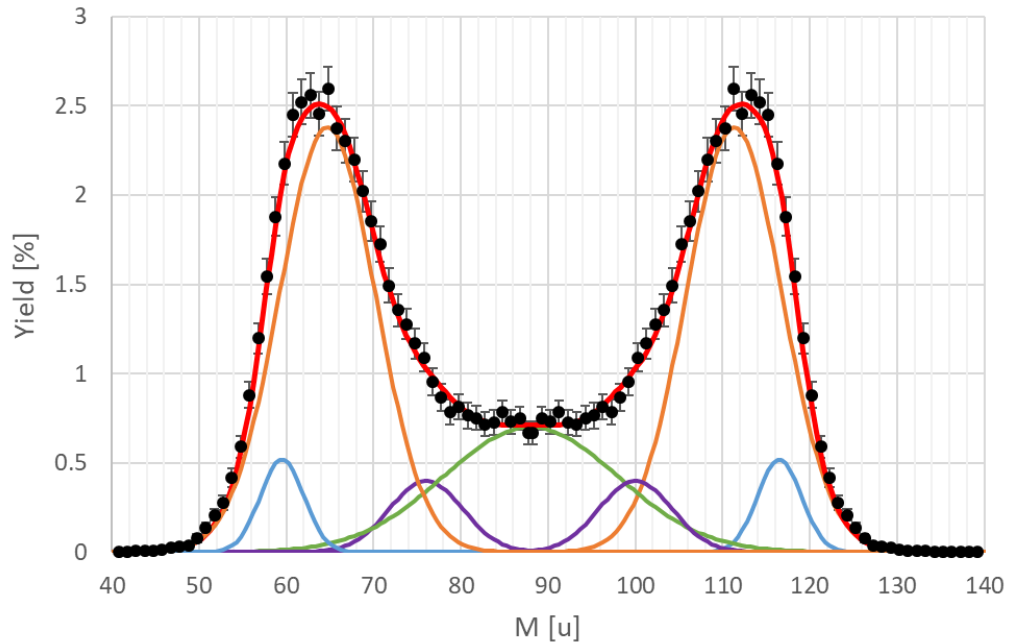
^{176}Hg $E^* = 48 \text{ MeV}$ 

Fig 2.35 Decomposition of the experimental mass distributions for ^{176}Hg at $E^* = 48 \text{ MeV}$ (black dots with error bars) into a symmetric (green line) and two asymmetric (orange and purple lines) components. Red line is the sum of the Gaussian curves.

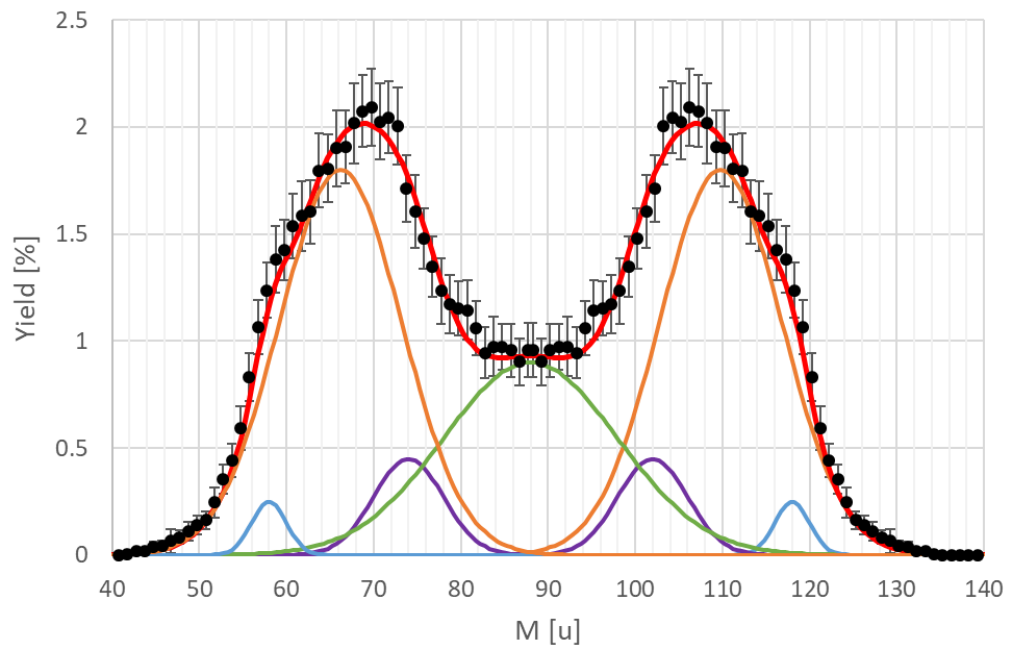
 $E^* = 35 \text{ MeV (symmetric)}$ 

Fig 2.36 Decomposition of the experimental mass distributions for ^{176}Hg at $E^* = 35 \text{ MeV}$, symmetric detection configuration, (black dots with error bars) into a symmetric (green line) and two asymmetric (orange and purple lines) components. Red line is the sum of the Gaussian curves.

$E^* = 35 \text{ MeV}$ (asymmetric)

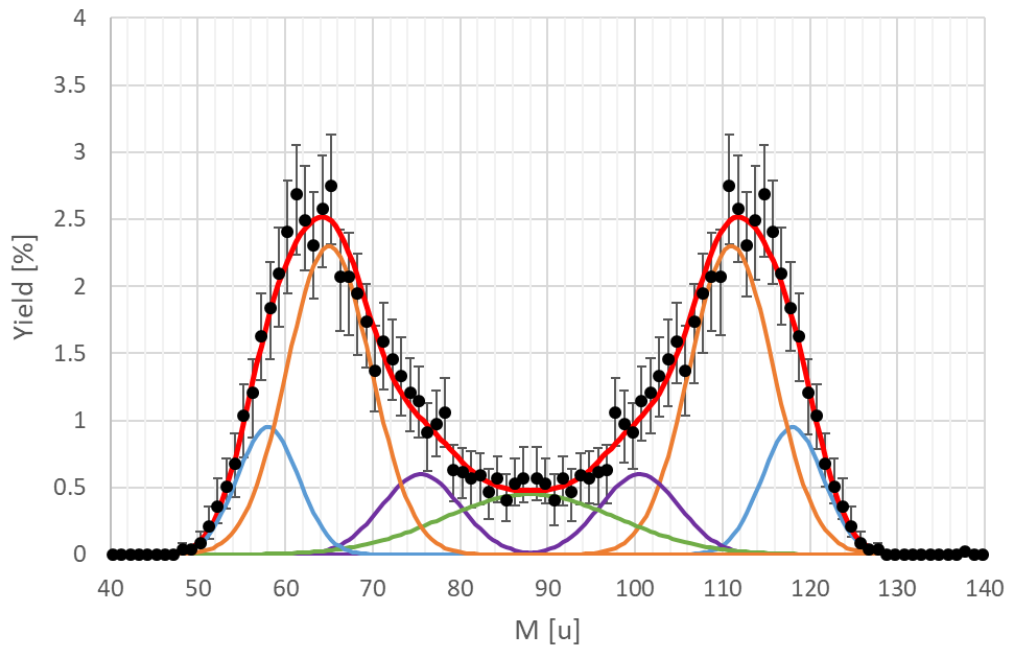


Fig 2.37 Decomposition of the experimental mass distributions for ^{176}Hg at $E^* = 35 \text{ MeV}$, asymmetric detection configuration, (black dots with error bars) into a symmetric (green line) and two asymmetric (orange and purple lines) components. Red line is the sum of the Gaussian curves.

$E^* = 25 \text{ MeV}$

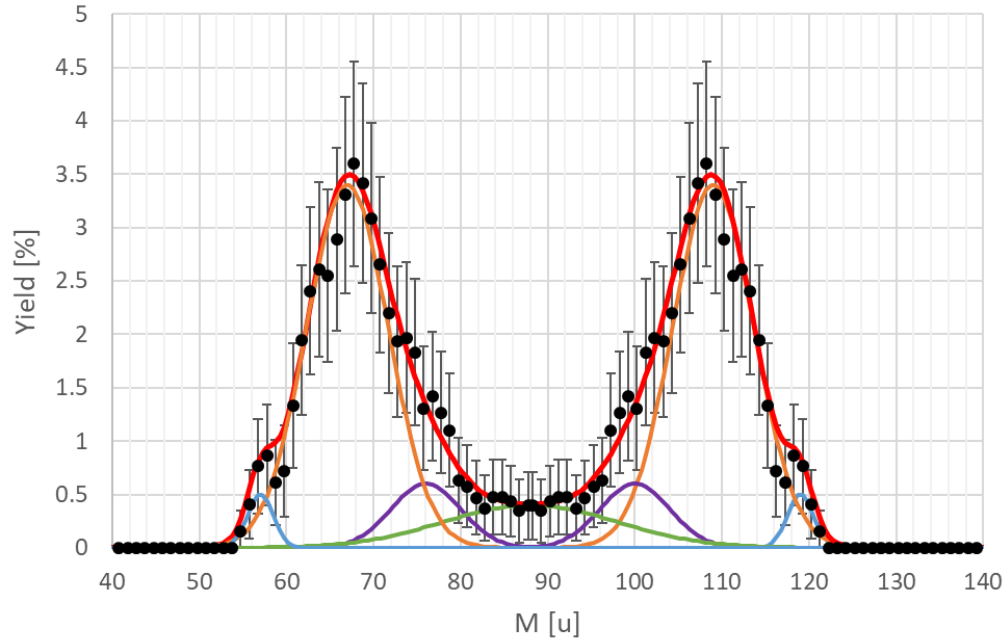


Fig 2.38 Decomposition of the experimental mass distributions for ^{176}Hg at $E^* = 25 \text{ MeV}$ (black dots with error bars) into a symmetric (green line) and two asymmetric (orange and purple lines) components. Red line is the sum of the Gaussian curves.

2.3.5 Discussion

The need of a third fission mode in the calculated mass distributions, suggested by the experimental data, provides an interpretative key to the fact that the mass distribution of ^{180}Hg becomes more symmetric with increasing excitation energy whereas the one of ^{176}Hg becomes more asymmetric, the main subject of this experiment.

A closer look at Figures 2.31 and 2.32 gives the clear path to interpret the different behavior of ^{180}Hg and ^{176}Hg .

In the case of ^{180}Hg , in the computed mass distributions (Figure 2.31), with increasing excitation energy, the calculated symmetric mode contribution becomes larger. However, the more asymmetric mode still remains dominant. The fact that the whole mass distribution becomes more symmetric is due to the increase of the symmetric component, but also to the weaker medium-asymmetric mode (the purple curve). The experimental mass distribution at $E^* = 48$ MeV is in agreement with this trend. For an even larger excitation energy ($E^* = 82$ MeV), the symmetric mode becomes dominant, the medium-asymmetric mode disappears, and the most-asymmetric mode clearly survives. This is consistent with the expectations. The shell effects are gradually quenched with increasing excitation energy, each mode disappearing at different excitation energy, but only the symmetric mode is last survivor. In this view, ^{180}Hg behaves as expected. There are some subtle differences still between the widths and the relative intensities of the modes in the experimental and computed distributions that will be discussed at the end. For now, we can conclude that the gross behavior with the excitation energy follows the expectation.

In the case of ^{176}Hg , the computed mass distributions (Figure 2.32), with increasing excitation energy, becomes more asymmetric. As stated before, this is considered at variance with what expected. The reason of this trend has to be searched in the competition of the three different modes identified by the combined analysis with the experimental data. The symmetric mode is truly reduced with increasing excitation energy, but the rate of the growing asymmetry is the consequence of the dropping of the mid-asymmetric mode and the strong increase of the most-asymmetric mode. Therefore, the symmetric mode is hindered by the most-asymmetric mode and partially by the mid-asymmetric mode. This is at variance with the behavior of ^{180}Hg .

When we turn now to the decomposition of the experimental mass distribution, we can compare the computed distribution at $E^* = 20$ MeV with the experimental one at E^*

= 25 MeV. Clearly, all three modes survive, however the relative intensity is strikingly different. In particular, the symmetric mode is strongly suppressed in favor of the most asymmetric mode. What is indeed more interesting is the evolution with the excitation energy. Going from $E^* = 25$ to 35 MeV the symmetric component grows, as expected, but at variance with the calculation. At $E^* = 48$ MeV we see a drop of its relative intensity (not a continuous growing) triggered, reasonably, by the increase of the most-asymmetric mode. The same behavior occurs, but to a minor extent, to the mid-asymmetry mode. It seems that the symmetric mode increases up to a certain point in the excitation energy after which it starts dropping. The dominance of the most-asymmetric mode is the cause of the hindrance of the mass symmetric mode. In the Moller's calculation, the symmetric mode is instead dominant at the lowest excitation energy and drops monotonically. In the experimental data, we observe its fast increase and afterwards a drop around 40 MeV. This behavior of ^{176}Hg is not reproduced in the calculations and is at variance with the regular behavior of ^{180}Hg .

A further comment concerns the width of the modes (Gaussian) and the computed intensity of the different modes. The widths of the modes give an indication of the width of the potential valleys: the larger the widths, the larger the width of the valleys. However, fluctuations in the width are also expected. This makes the width to change with the excitation energy. The relative intensity of the different modes is related to number of times a trajectory is walked through in the potential: the most populated trajectory gives rise to the most populated mode. The decision of which trajectory will be populated in a decay is matter of the dynamics of the decay. In Moller calculations, the dynamics is implemented with a simple model. For instance, no dissipation is included (viscosity is null). This, by itself, produces a bias in the relative intensity of the different modes, and consequently, in the shape of the mass distributions. To dig more in this detail, the analysis of the mass distributions should be done in parallel with the computed TKE distributions. However, these are not available. Regardless of this unimplemented features, it is clear that the experimental mass distributions are compatible with the same modes that reproduce the calculated mass distributions for both ^{176}Hg and ^{180}Hg . This is already an important result because it tells that the shell corrections occur in the same place in the potential as calculated. However, the relative intensities follow a different pattern in the case of ^{176}Hg . This means that the dynamics is still very important besides the shell corrections. This analysis reveals that ^{176}Hg behaves at variance with what expected. In particular, the relative strength of the

different fission modes changes quite surprisingly with the excitation energy. This finding of course requires further work for its confirmation. At the same time, it provides the motivations for searching a similar effect in other nuclei.

As a last point, it is worth to compare the Moller distributions with the ones obtained by fitting the data and removing the part due to the QF or quasi-elastic components (the blue curves). These comparisons summarize the whole picture. Some gross features are reproduced by the calculations, but the relative intensities of the different modes are not. The awkward behavior of ^{176}Hg is confirmed. As a result of this study, it is attributed to an unexpected competition among two main modes, the symmetric and the most-asymmetric one, with a minor role played by the mid-asymmetric mode.

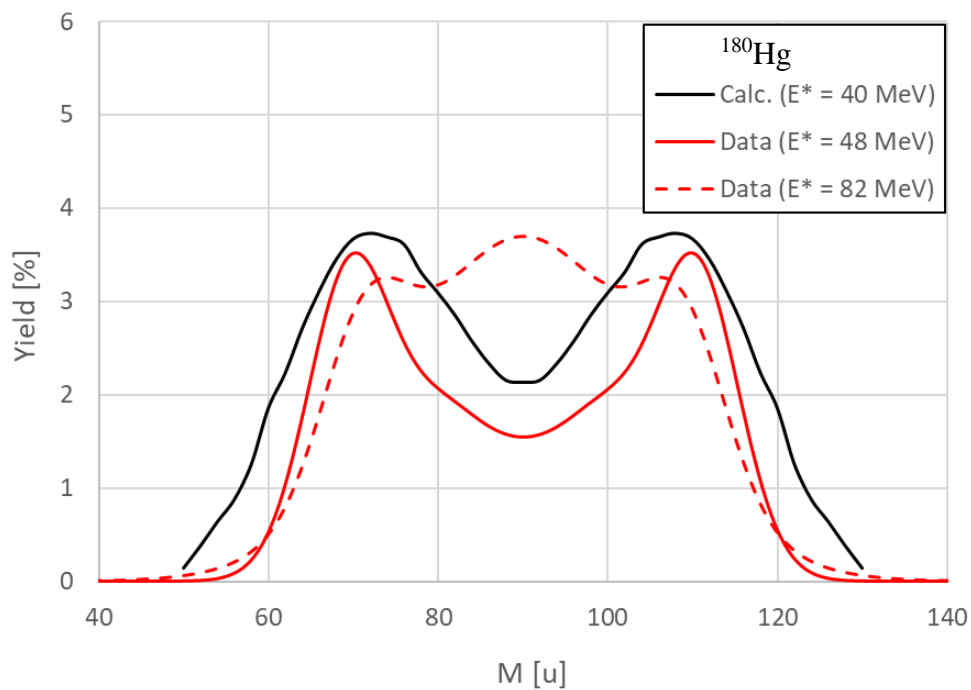


Fig 2.39 Experimental fission fragments mass distributions for ^{180}Hg at $E^* = 48$ (red solid line) and 82 MeV (red dashed line) compared to Moller's calculations for $E^* = 40$ MeV (black solid line).

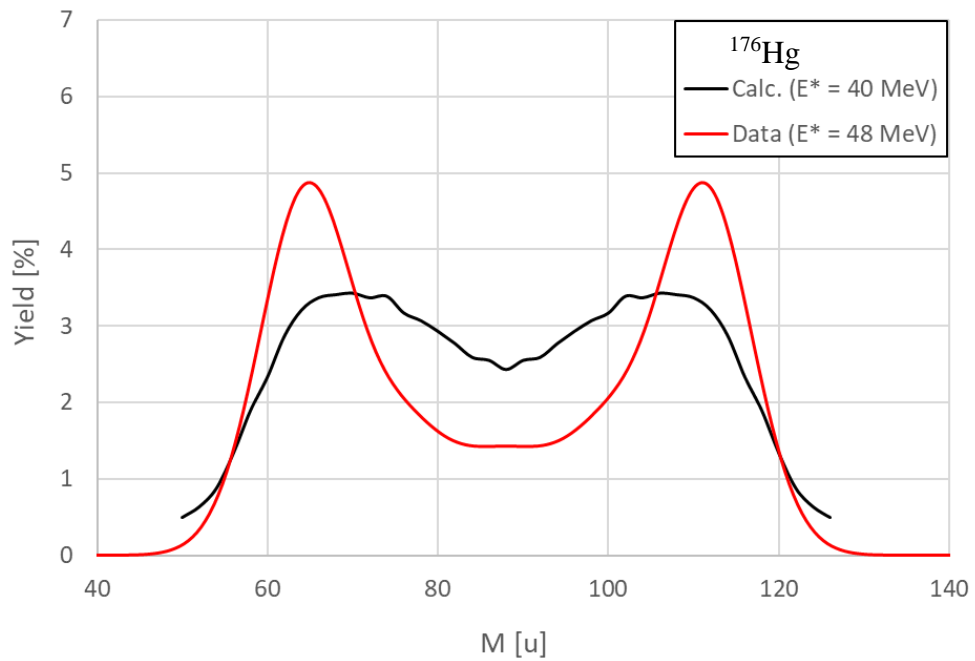


Fig 2.40 Experimental fission fragments mass distributions for ^{176}Hg at $E^* = 48$ MeV (red solid line) compared to Moller's calculations for $E^* = 40$ MeV (black solid line).

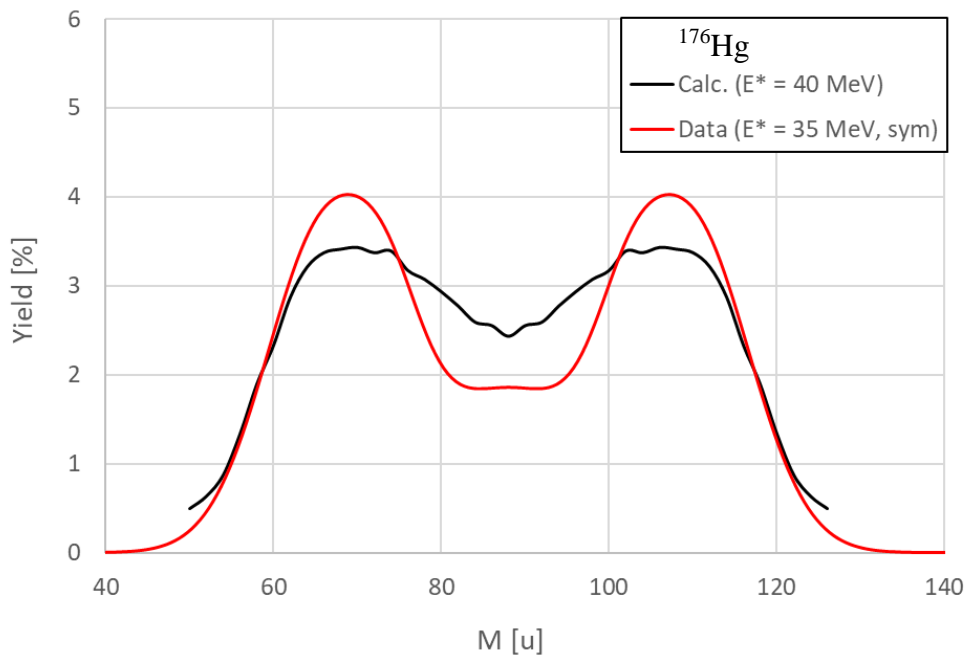


Fig 2.41 Experimental fission fragments mass distributions for ^{176}Hg at $E^* = 35$ MeV (red solid line) compared to Moller's calculations for $E^* = 40$ MeV (black solid line).

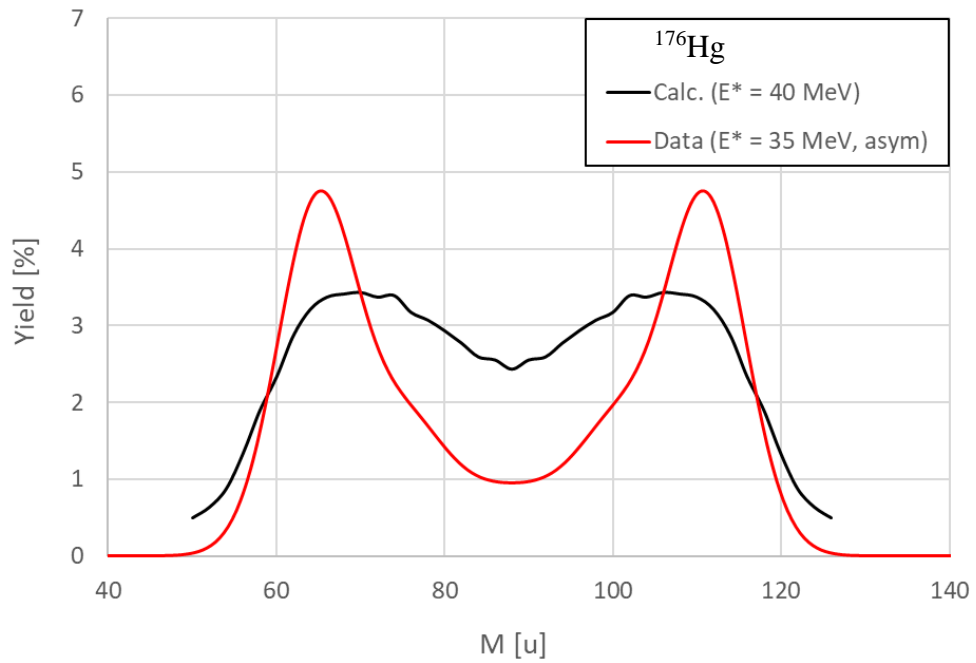


Fig 2.42 Experimental fission fragments mass distributions for ^{176}Hg at $E^* = 35$ MeV, asymmetric geometry, (red solid line) compared to Moller's calculations for $E^* = 40$ MeV (black solid line).

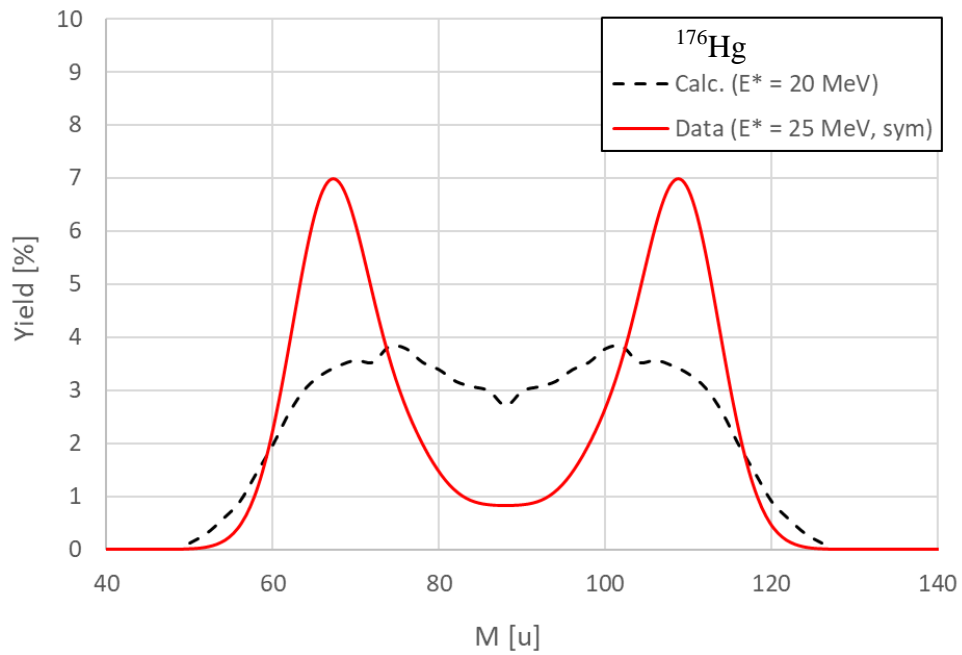


Fig 2.43 Experimental fission fragments mass distributions for ^{176}Hg at $E^* = 25$ MeV (red solid line) compared to Moller's calculations for $E^* = 20$ MeV (black dashed line).

Chapter 3 – Experiment $^{32}\text{S} + ^{197}\text{Au}$

3.1 Scientific motivation

Heavy-ion induced fusion reactions at bombarding energies around the Coulomb barrier have been very successfully used for the production of superheavy elements (SHE) [29, 30, 31]. To select the optimal reactions for the production of new elements heavier than Og and/or new isotopes around the superheavy island of stability the measurement of fusion cross sections is an essential step [32]. In fusion events, a compound nucleus may evolve toward fission or the formation of an evaporation residue (ER) after the evaporation of light particles. The fusion cross section is measured by summing the cross sections of these two decay channels. The fission cross section is usually measured by counting the number of fragments produced in binary reactions. In the case of reactions between massive nuclei necessary for the search of superheavy elements, the evaporation residues cross section is negligible with respect to the fission one. Therefore, it is sufficient to select and count the fission events to estimate the fusion cross section [14]. However, at energies around the Coulomb barrier, the quasi-fission reaction mechanism, which also gives rise to binary products, becomes dominant and counteracts the complete fusion, as seen in Section 1.3. CN fission and QF are both binary decay channels characterized by large nucleon exchange and energy dissipation. These common properties make the experimental separation between them difficult, especially in the case where both processes result in symmetric mass split, like in Figure 1.9. In order to achieve a signature providing a clear separation among the events of these two different processes, several techniques based on the analysis of different experimental observables of fission like fragments have been used.

3.1.1 Signatures of quasi-fission

The characterization of fission like fragments produced by CN fission and QF has been achieved by exploiting the properties of fission like fragments produced in reactions leading to the formation of the same composite system from different entrance channels. In the lack of comprehensive theoretical models, it is necessary to proceed empirically

by searching for correlations between observables in order to provide a systematic description and to extrapolate their behavior in unknown regions. One of the real doubts on the extrapolation reliability concerns the fact that nuclear properties in the regions of heavy and superheavy nuclei, challenging to access even with the most performant setups, may change dramatically just by adding few nucleons because of the sharp change due to the shell effects.

Typical patterns of the mass-TKE distributions, which elucidate the onset of the QF, are summarized in Figure 3.1 [14]. All reactions lead to the formation of the Hs composite system but entrance channels are vastly different. These reactions were chosen as a case study to provide a prompt view of some of the most relevant features of QF. From left to right, the entrance channel mass asymmetry decreases and Coulomb factor increases. The two reactions in the middle are expected to form the same CN at similar excitation energies from different entrance channels.

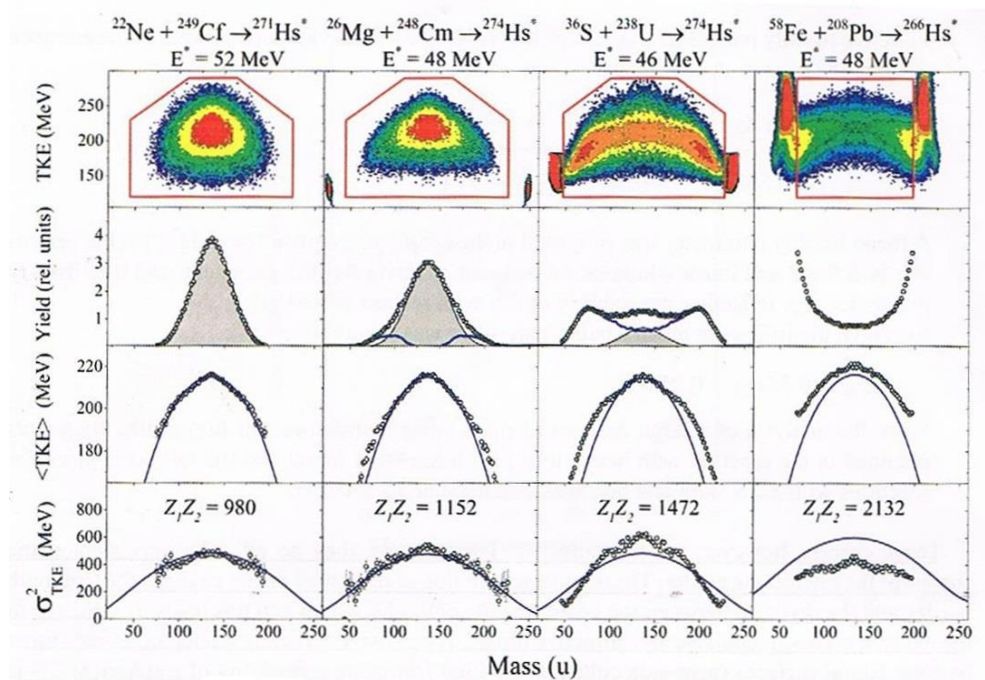


Fig 3.1 Mass-TKE distributions of binary product at energy above the Coulomb barrier. From left to right the entrance channel mass asymmetry decreases and the Coulomb factor Z_1Z_2 increases. Solid curves in the average TKE and its variance are the LDM expectation for CN fission. [14]

The area between the expected quasi-elastic region and the symmetric mass split region, typical of CN fission, gets filled with further binary products with the increases of the entrance channel asymmetry. In the case of the reaction $^{22}\text{Ne} + ^{249}\text{Cf}$, the mass distribution shows a Gaussian shape. In the reaction $^{26}\text{Mg} + ^{248}\text{Cm}$ the mass distribution

is nearly Gaussian with the appearance of two slight shoulders. These two reactions show mass-TKE distributions features that can be ascribed to the expectation of the LDM fission and therefore can be considered mainly originated by a CN fission process. With the decreasing mass asymmetry, the mass distributions of the fragments change quite remarkably: in the case of $^{36}\text{S} + ^{238}\text{U}$ the two asymmetric QF shoulders become more pronounced and for $^{56}\text{Fe} + ^{208}\text{Pb}$ the mass distribution becomes a pot-shaped.

Also quite striking is the difference in the shapes of the mass-TKE distributions observed in the two cases in which the same composite system ^{274}Hs is populated. The progression in the mass-TKE distribution, which makes one to invoke QF mechanism, is also reflected in the other two observables, the average TKE and the variance of the TKE distributions as a function of mass fragment σ_{TKE}^2 . Both these observables deviate from the expectation of the LMD model. In particular, the deviation observed in the reaction $^{56}\text{Fe} + ^{208}\text{Pb}$ makes one suspect that this QF process is dominant with respect to CN fission in the full mass range and results in colder fragments being the average TKE higher.

The mass asymmetry and the Coulomb factor of the entrance channel are reported to play a primary role in the rising of QF. However, microscopic features, such as shell closures, have quite a striking impact on the mass-TKE distribution, which is the main playground where to probe our knowledge of the shell effects. Moreover, microscopic features offer a key to interpret the competition between QF and CN fission and a way to estimate their relative contribution.

It is well known that in superheavy composite system QF mainly leads to the formation of asymmetric fragments with mass asymmetry ~ 0.4 [33]. This type of QF process is characterized by asymmetric angular distributions in the center of mass system and fast reaction times ($\sim 10^{-21}$ s). The TKE of these fragments is observed to be higher than that for CN fission and hence this process is less dissipative. This means that the nuclear temperatures involved are low and the fragments, usually defined as “colder fragments”, are produced at low excitation energies. Due to this reason shell effects in asymmetric QF are more pronounced.

Besides the asymmetric component, also the symmetric component may be affected by the presence of the QF process. Consequently, the question of whether the symmetric fragments originate from CN fission or QF process arises. Figure 3.2 shows the experimental mass distribution for fission-like fragments (black squares) produced in the reaction $^{36}\text{S} + ^{238}\text{U}$ (black squares). Panels a) and b) show two (among many)

possible decompositions of the same data into a fission component (red curve, taken as a LDM Gaussian) and a QF component (blue curve, taken as the remaining part of the mass distribution). As the LDM can predict the shape of the fission fragments mass distribution, but cannot predict the relative intensity of CN fission with respect to QF this model cannot be used to get indication on how to separate the two different processes in the symmetric mass region by considering the mass distribution or TKE distribution. Also the angular distribution for all those mass-symmetric fragments is symmetric with respect to 90° in the center of mass system. The overlap of CN fission and QF in the symmetric mass region constitutes an inescapable problem when CN fission cross section has to be estimated.

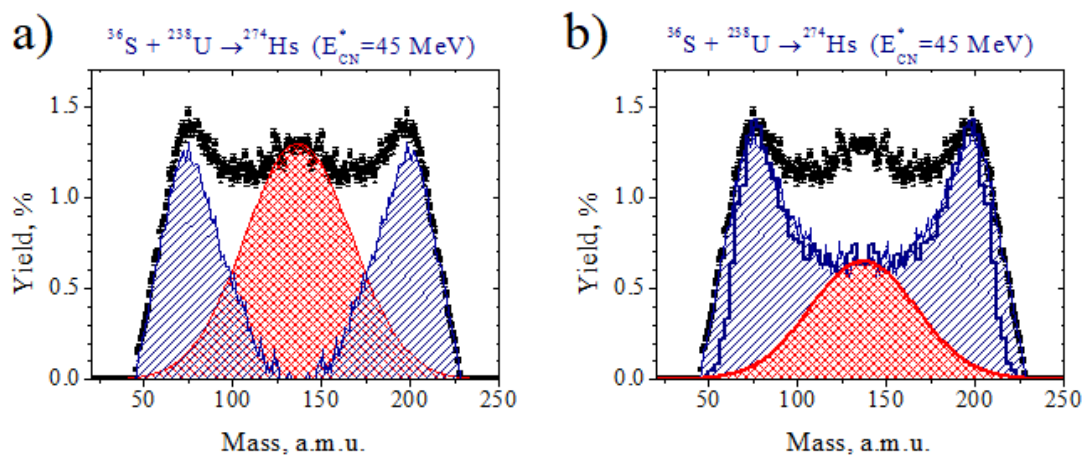


Fig 3.2 Experimental mass distributions for fission-like fragments (black squares) formed in the reactions $^{36}\text{S} + ^{238}\text{U} \rightarrow ^{274}\text{Hs}$ at energy below the Coulomb barrier. a) and b) show two (among many) possible decomposition of the same data into a CN fission component (red curve) and a QF component (blue curve). Data from [14]

That said, it appears clear that a disentanglement of CN fission and QF processes is very hard to achieve. This is possible only, to some extent, for the asymmetric part of the mass distribution. Furthermore, most of the analyses are based on the decomposition of mass and TKE distributions with the help of model predictions, so the experimental results are greatly model dependent. Consequently, mass, TKE and angular distributions with their variances do not represent a set of observable providing clear signatures for the correct disentanglement of the two processes. In addition, a complete picture describing the QF process features is still missing. Therefore, to better define the intriguing features of this transition region between direct and complete fusion nuclear reactions involving massive nuclei, large efforts by considering innovative experimental approaches and new theoretical models are still needed.

3.1.2 *Gamma ray probe*

The differences between these two processes mark the path towards the identification of better observables for their disentanglement. On one side there is CN fission, a process in which two nuclei fuse with the dissipation of all the relative motion energy, passing through an equilibrium stage consisting in the formation of a CN, with the successive decay; typical times are about $\tau \sim 10^{-19}s$. On the other side there is QF, a faster process with less mass transfer, less energy transfer and partial motion energy dissipation; typical times are about $\tau \sim 10^{-21} \div 10^{-20}s$. It is reasonable to think that for the slower process all the orbital angular momentum is transferred into internal degree of freedom of the CN and so the two fragments after the fission have an higher spin than the two fragments produced by QF.

The possible ways to probe angular momentum of the two fragments are neutrons and gamma rays emission. Neutrons have higher detection efficiency than gammas but to extract information on the angular momentum transported by neutrons it is necessary to use the statistical model. This implies a model dependent analysis. Furthermore, the availability of neutron detection systems are less common than gamma ones.

It is possible to probe angular momentum through gamma rays by means of the discrete gamma transitions of the fragments or the total number of gammas emitted per event (summing up statistical and discrete gamma rays), namely the gamma multiplicity, M_γ . The gamma multiplicity gives access to a more straightforward analysis: the larger the gamma multiplicity, the larger is the angular momentum and energy transferred. Furthermore, assumed that each gamma quanta takes away some average value of intrinsic angular momentum, a proportionality exists between the multiplicity and the highest spin populated.

3.1.3 *Performed experiment*

The possibility to establish a method that, by correlating the gamma ray multiplicity and the composite system spin, allows to identify the time scale corresponding to the reaction producing the event have to be experimentally verified. In this work, it has been considered as representative of the short time scale process the quasi-elastic (QE) reaction channel. As shown in Figure 3.1, fragments from the quasi-elastic channel in the mass-TKE matrix are well distinguishable from FF and QF products, in fact they are

located in the regions around the mass of the target and projectile nuclei. If the hypothesis that a higher angular momentum population corresponds to a large interaction time is valid, the gamma multiplicity measured in coincidence with the QE component should be smaller than the one in coincidence with the fission fragments in the symmetric mass region. This would prove the concept and would open the road to experiments that, by employing an additional probe, allow to distinguish between QF and CN fission events even in the symmetric mass region.

To explore this concept, the $^{32}\text{S} + ^{197}\text{Au}$ reaction, at the energy near the Coulomb barrier, $E_{lab}(^{32}\text{S}) = 166 \text{ MeV}$ ($E_{CM}/V_C = 0.997$), was proposed and performed at the Tandem ALTO accelerator at IPN Orsay (France). This reaction is characterized by a large fusion-fission cross section, and a negligible contribution from the QF. The central part of mass-TKE distribution corresponding to the symmetric scission is therefore dominated by fragments originated in FF process and would not be polluted with components from processes of nearby time scale. Consequently, the comparison between the gamma multiplicity in the QE channel and the fusion-fission channel would provide the best conditions to evaluate the validity of the concept described above.

In this experiment, the time-of-flight spectrometer CORSET was used to detect the fragments, and the ORGAM and PARIS arrays were used to detect gamma rays. In this way, the mass-TKE of the binary fragments and the gamma rays in coincidence can be extracted.

A description of the experimental setup and the analysis method used is provided in the following Sections.

3.2 *Experimental setup*

3.2.1 *CORSET*

Binary reaction products have been detected in coincidence by using the two-arm time-of-flight spectrometer CORSET. For a description of the apparatus, see Section 2.2.1.

The two arms of CORSET were at 68° and 66.5° from the beam axis. The start detectors for both the arms were at 60 mm from the target and the stop detectors at 210 mm from the start. The size of the CORSET stop detectors is 89 mm \times 68 mm, covering an angular acceptance of $\pm 12.0^\circ$ in the horizontal plane and $\pm 5.5^\circ$ in the vertical plane.

Beam monitor detectors were at 18° from the beam axis and at 130 mm from the target. The used target is a $40 \mu\text{g}/\text{cm}^2$ thick carbon foil used as backing with a $350 \mu\text{g}/\text{cm}^2$ thick layer of ^{197}Au placed at 90° with respect to the beam axis.

In Figure 3.3 is illustrated the geometry of the CORSET setup for the present experiment.

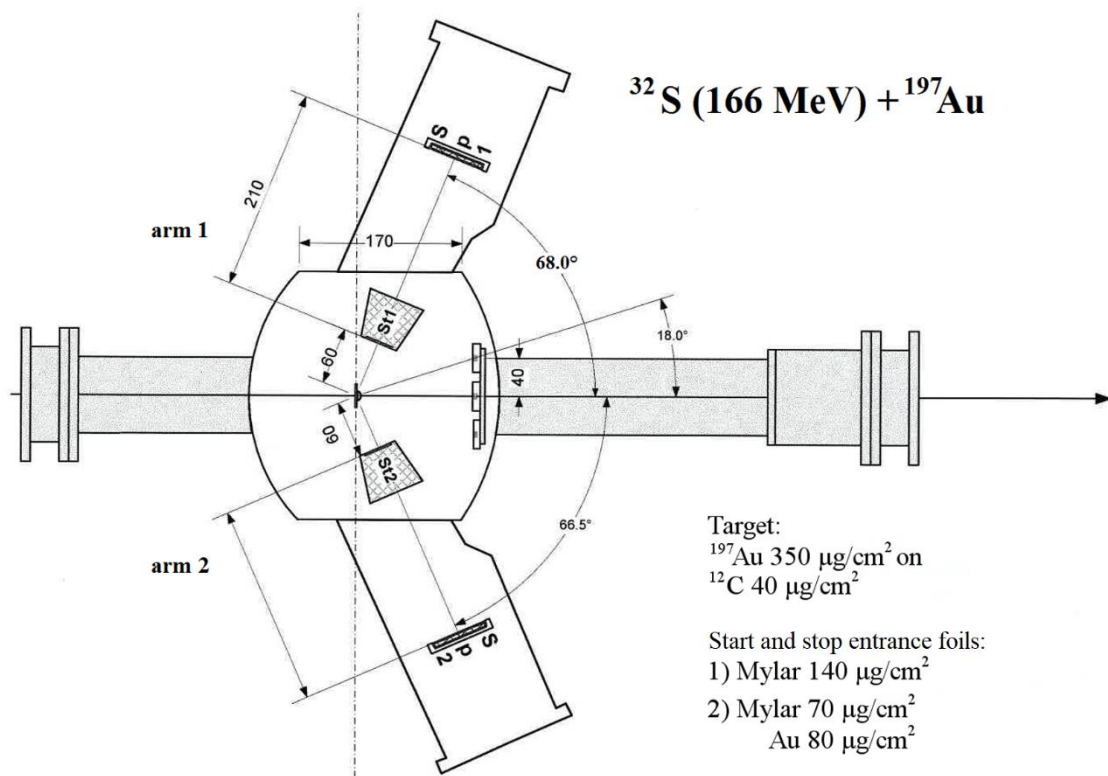


Fig 3.3 Geometry for the CORSET setup for the present experiment. In the bottom right corner are illustrated the characteristic of the target and of the start and stop foils.

3.2.2 ORGAM

ORGAM (ORsay GAMma Array) [34] is a closely-packed array of high-resolution germanium (Ge) detectors surrounded by bismuth germanate (BGO) scintillators. Figure 3.4 gives a schematic diagram of a single detector. The Ge detectors are large, coaxial, hyper pure n-type crystals, ~ 70 mm in diameter and ~ 75 mm in length. The liquid nitrogen cryostat keeps the detector at operative temperature.

Every Ge detector has a Compton suppression shield composed of ten optically isolated BGO scintillators, each with a photomultiplier readout. BGO detectors have a resolution (for 662 keV gamma rays) of 18 – 22% when the source is placed in the germanium detector position. The detectors are tapered over the front 3 cm out of their

lengths to allow closer packing when in the array.

In the present experiment, 10 ORGAM detector units were used, all placed at backward angles. Each detector has an angular opening of 20° . The target is positioned 181 mm from the front of the Ge crystals. The average geometrical efficiency is 0.6% per detector.

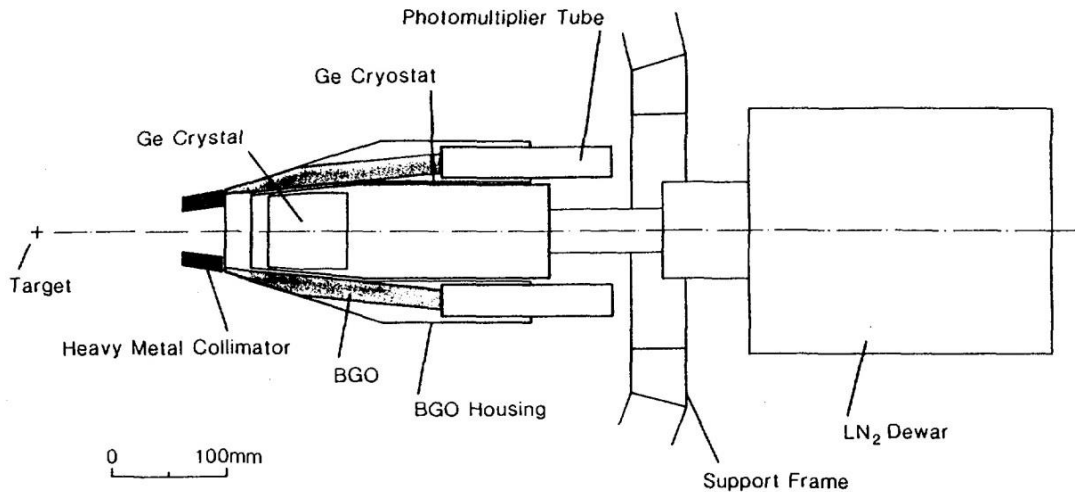


Fig 3.4 Schematic diagram of a single ORGAM element. [34]

3.2.3 PARIS

PARIS (Photon Array for the studies with Radioactive Ion and Stable beams) [35] is a high efficiency gamma-calorimeter detector array composed by $\text{LaBr}_3(\text{Ce})$ - $\text{NaI}(\text{Tl})$ phoswich base units. A phoswich, literally "phosphor sandwich", is a scintillation detection system consisting of two or more different scintillator crystals, with dissimilar pulse shape characteristics, optically coupled to each other and to a common photomultiplier tube. The primary crystal is thick enough to absorb the radiation of interest, while the secondary one, which is thicker, acts as a Compton suppression shield.

The individual phoswich detector element consists of a front $\text{LaBr}_3(\text{Ce})$ cubic crystal ($5 \times 5 \times 5 \text{ cm}^3$) optically coupled to a $\text{NaI}(\text{Tl})$ crystal ($5 \times 5 \times 15 \text{ cm}^3$) at the back. Every detector is coupled with a cylindrical photomultiplier tube (PMT), which collects the light outputs generated in both phosphor components. The phoswich is then hermetically sealed in a single aluminum case, coupled through a glass window to the PMT.

In the present experiment, 10 PARIS detectors were used, all placed at forward angles, packed in a 3×3 cluster plus a single detector. Figure 3.5 shows a picture of the cluster (left) and of the single detector (right). The center of the cluster was located at ~ 38 cm from the target, the single detector was located at ~ 30 cm from the target. The average geometrical efficiencies are 0.14% per single detector in the cluster configuration and 0.22% for the single detector.

To discriminate $\text{LaBr}_3(\text{Ce})$ from $\text{NaI}(\text{Tl})$ events, the electronic board “LaBrPro” [36] has been used. It provides a first Gaussian signal (also called “fast” signal) whose amplitude is proportional to the integral of the light signal from the fast leading edge up to the maximum, and a second Gaussian signal (also called “slow” signal) whose amplitude is proportional to the integral of the entire signal that correspond to the total energy released into the phoswich ($\text{LaBr}_3(\text{Ce})$ and $\text{NaI}(\text{Tl})$). The comparison of the fast and slow signals provides a method for the identification of Compton events between the two crystals of a single phoswich detector. The time information is given by a CFD.



Fig 3.5 On the left, a PARIS cluster. On the right, a single phoswich detector element.

3.2.4 Electronics and trigger

The circuit diagram of the double-arm ToF spectrometer is shown in Figure 2.7. For the description of the electronics used for the acquisition of the CORSET signals, see Section 2.2.2. The trigger, as in the experiment previously presented, is given by the coincidence between the two stop signals and at least one of the two start signals.

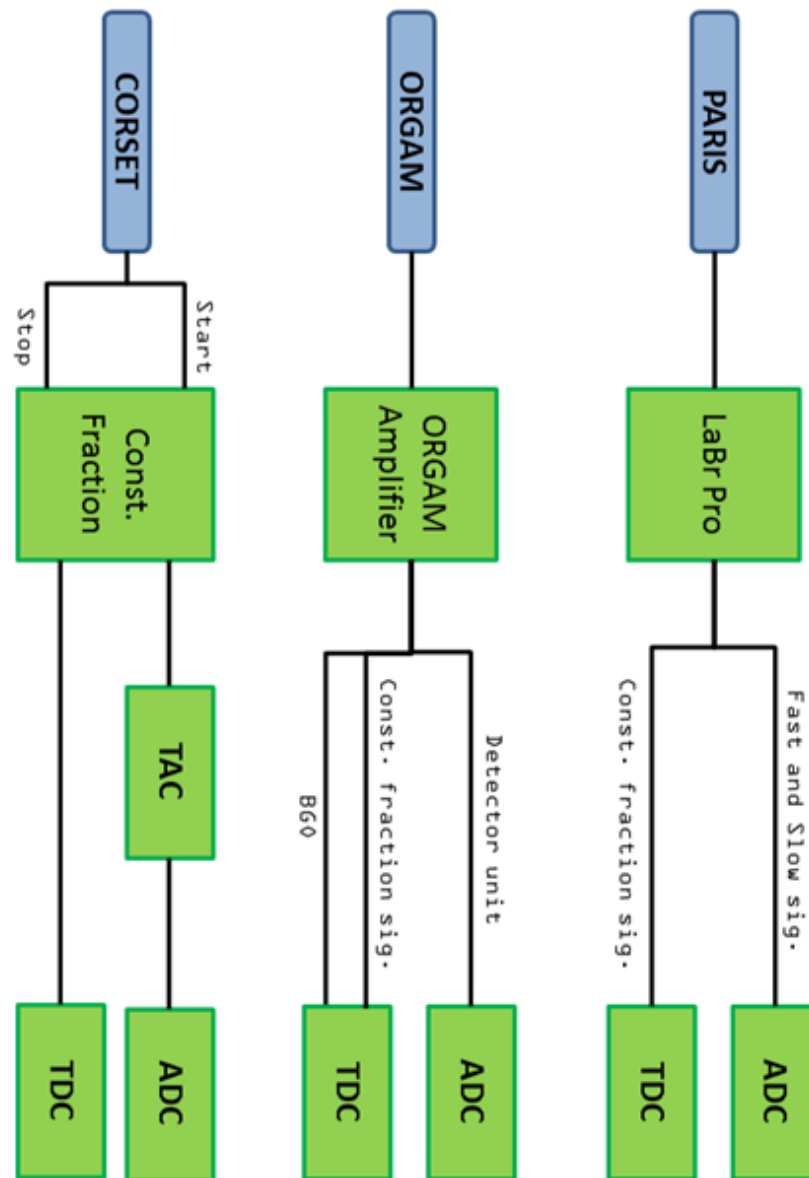


Fig 3.6 Block diagram of the used electronics.

The photon energy signals from ORGAM and PARIS detectors are transmitted to ADCs for the spectroscopic information. Signals from the Compton suppression shield are fed into CFDs together with energy signals and come to TDCs. This gives the time information for the Compton anticoincidence. Signals from the PARIS detectors, instead, are fed into the LaBrPro module, and, thus, are transmitted to ADCs. The constant fraction signal of LaBrPro is transmitted to TDC for time signal. The amplifications of the individual spectroscopic signals from ORGAM detectors were set to span a dynamic range from ~ 100 keV to ~ 2.5 MeV. In the case of PARIS, the

chosen dynamic range went up to ~ 20 MeV. Figure 3.6 shows a general block diagram for the electronics used in the present experiment. Signals from ADC and TDC were fed into the VIPERS data acquisition system (see refs [37-40]).

Used modules include ORTEC CFDs, mod. 935, and TACs, mod. 566; CAEN ADC, mod. V785, and TDC, mod. V775; SIS GmbH scaler SIS3800; commercial NIM modules (such as preamplifiers, amplifiers, delay generators, logic units, FIFO, trigger box, NIM/ECL translators).

3.2.5 *ORGAM and PARIS calibration*

Both ORGAM and PARIS detectors were calibrated with a ^{152}Eu source. The energy calibration for the ORGAM detectors has been done using 11 of the ^{152}Eu gamma ray peaks, with an energy resolution for the full-energy peak of 4 keV at 1408 keV. The energy calibration for the PARIS detectors (separately for the fast and slow signals) has been done using 4 of the ^{152}Eu gamma ray peaks (because of the different dynamic range, the least energetic peaks were in the pedestal and the least intense peaks were covered by near, more intense peaks), with an energy resolution for the full-energy peak of ~ 15 keV at 1408 keV.

To obtain the efficiency calibration spectra, the source was placed in the target position for about 10 minutes. The number of events for each full energy peak has been obtained by a Gaussian fit, cutting the background and correcting for the acquisition dead time. Given the activity of the source with its reference time and calculated the present activity, the efficiency curves have been obtained for each detector in the form:

$$\varepsilon(E) = A_1 e^{(-E/E_1)} + \varepsilon_1 \quad [3.1]$$

in which E is the gamma ray energy; A_1 , E_1 and ε_1 are parameters obtained by fitting the experimental data. The total photopeak efficiencies in the low energy range are 1.5% for the ORGAM array and 0.7% for the PARIS array.

Figures 3.7, 3.8, and 3.9 show the spectra for single detector (respectively detector number 1 from ORGAM, from PARIS -fast signal- and from PARIS -slow signal-) used for the energy calibration. The used peaks are marked with a number representing their energy in keV.

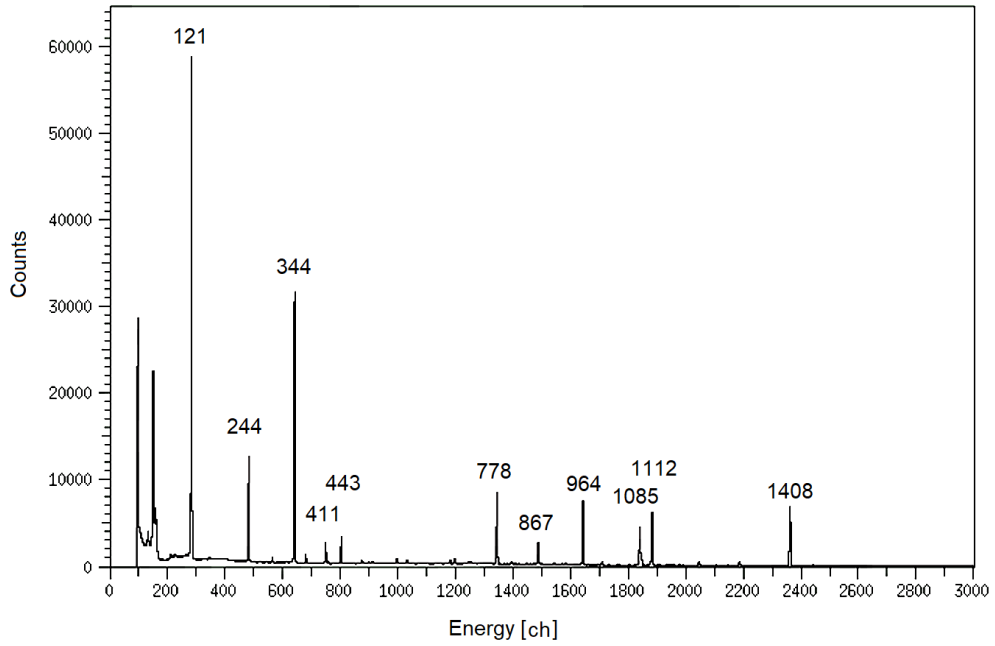


Fig 3.7 Calibration spectrum collected with an ORGAM Ge detector. The peaks used for the calibration are labelled with their energy in keV.

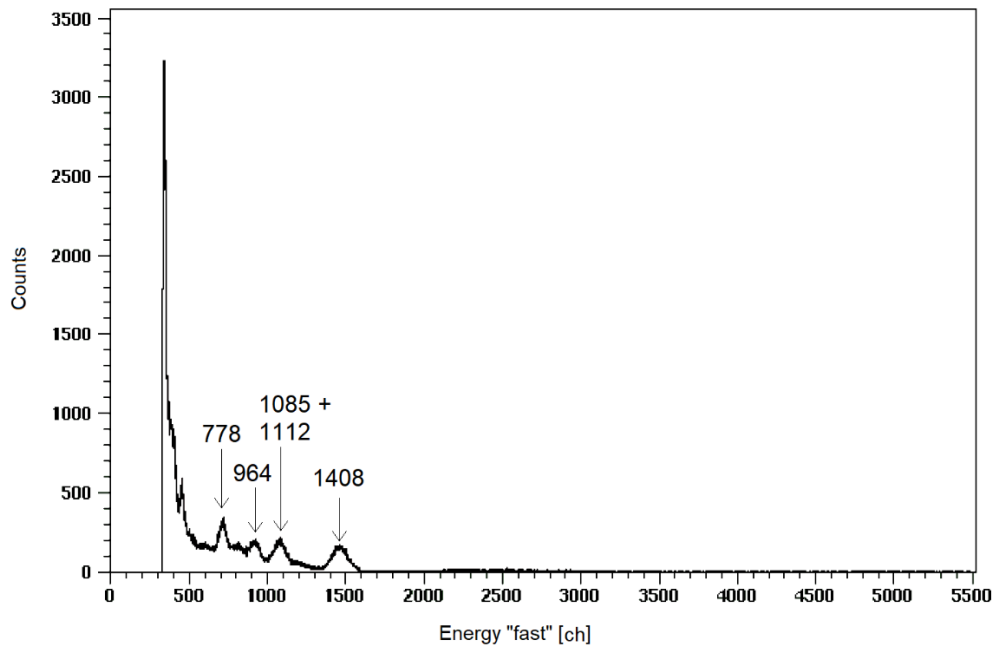


Fig 3.8 Calibration spectrum collected with a PARIS detector, relative to the fast signal from the LaBrPro module. The peaks used for the calibration are labelled with their energy in keV.

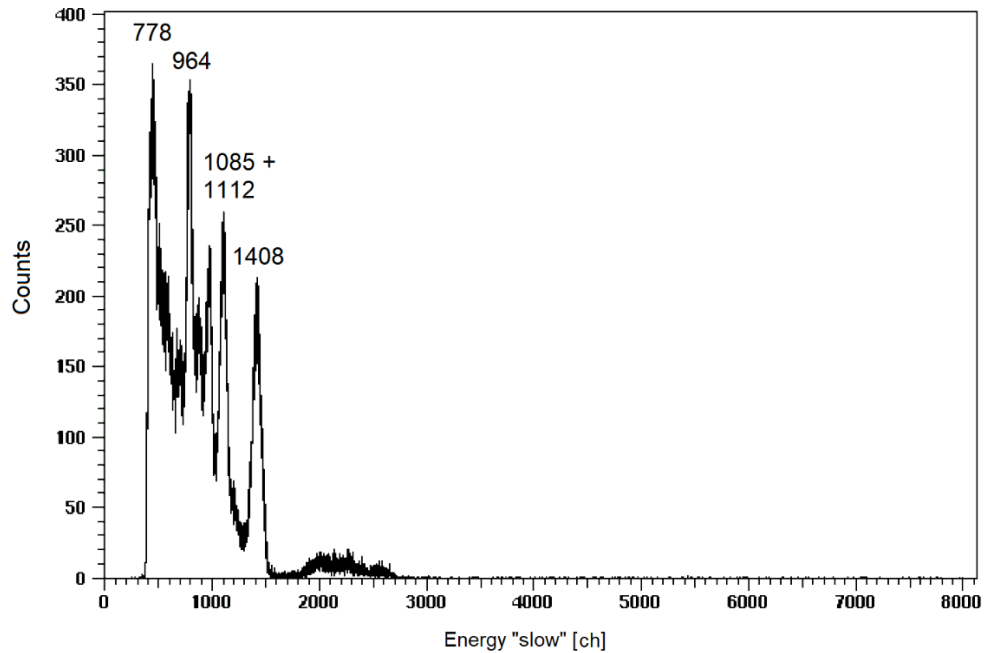


Fig 3.9 Calibration spectrum collected with a PARIS detector, relative to the slow signal from the LaBrPro module. The peaks used for the calibration are labelled with their energy in keV.

3.3 Results and discussion

3.3.1 Selection of binary reaction channels

The ultimate goal of the experimental program is to find a signature of the reaction dynamics in order to separate FF and QF products using γ -ray observables. In this study there is a wide profit in the measurements of mass and TKE of the coincident fragments.

The mass-TKE matrix for binary events is reconstructed from CORSET coincidence data. The measurements of the ToFs and the flight paths of the fragments are used to reconstruct the event-by-event velocity vectors of the two emerging fragments; then, from the two velocity vectors, masses and energies of each couple of fragments are reconstructed, as shown in Section 2.3.1. The mass-TKE matrix obtained in this experiment for center of mass angles at $(90 \pm 10)^\circ$ is shown in Figure 3.10 (top).

By considering only the FMT events, as shown in Section 2.3.1, it is possible to isolate the FF reaction products. The mass-TKE distribution in Figure 3.10 (bottom) is obtained requiring the FMT and selection of FF events in the velocity plot and can be considered as originated in FF reactions, being the QF component negligible in this reaction. The two loci on the left and right of the FF region, Fig 1 (top), can be ascribed

to the QE reaction. Preliminary results were already published in [41] and the present mass-TKE distribution in [42].

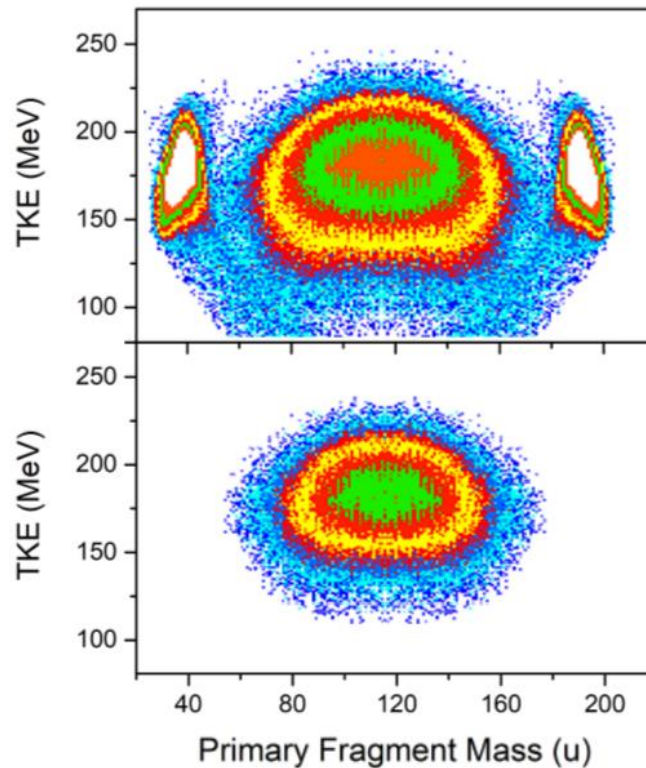


Fig 3.10 Mass-TKE matrix within the ^{32}S ($E_{\text{lab}} = 166 \text{ MeV}$) + ^{197}Au reaction without conditions (top) and applying the full momentum transfer condition, with an additional gate on fission fragments only (bottom). Data already published in [42].

3.3.2 Selection of gamma rays in coincidence with binary reaction channels

By gating on specific regions of the mass-TKE distribution for FMT events, one is able to select only gamma rays associated to each reaction mechanism, FF or QE. To extract gamma spectra, however, gamma ray events have to be properly processed. For instance, for both PARIS and ORGAM, gates have been considered on time signals to isolate the prompt gamma rays component of the energy spectra. The anti-coincidence condition between Ge and BGO detectors suppresses the Compton component of the ORGAM energy spectrum. Spectra resulting from this procedure are shown in Figure 3.11. Both spectra correspond to a single ORGAM detector: the red solid one is in coincidence with QE events; the black dashed one is the spectrum in coincidence with FF events. The most intense peaks in the QE gamma spectrum have been assigned to the

low-energy and low-angular momentum ^{197}Au transitions (marked in Figure with numbers from 1 to 4). These peaks are strongly suppressed in the spectrum in coincidence with FF events. This behavior represents an indication that a faster process transfers less angular momentum to the final fragments.

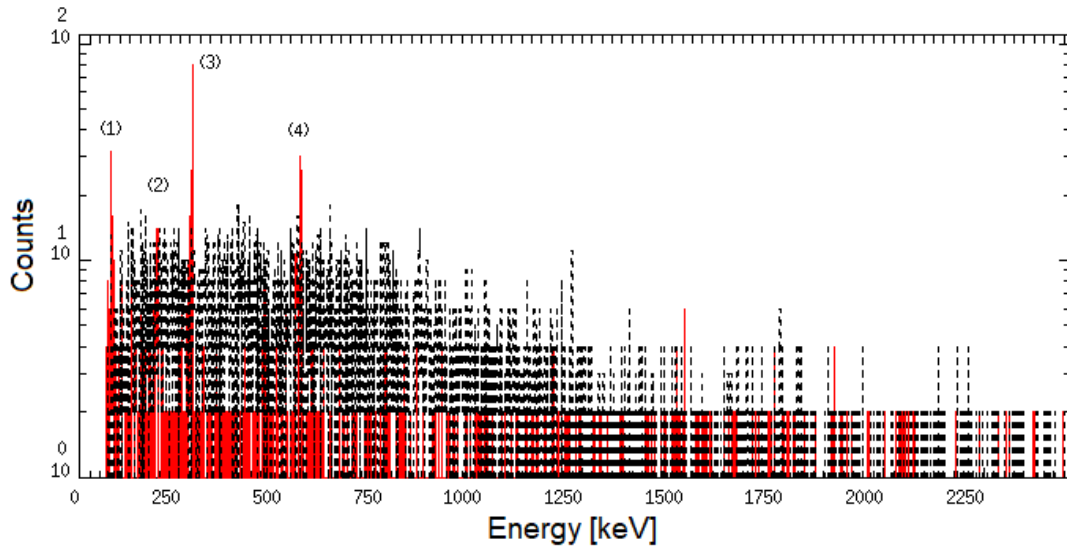


Fig 3.11 Gamma spectra detected in coincidence with quasi elastic events (red solid line) and with fission fragments (black dashed line) events. Marked peaks in the red spectrum are identified as ^{197}Au transitions. Energies of the peaks are, in order from (1) to (4): 77 ± 2 keV, 192 ± 3 keV, 280 ± 2 keV, 549 ± 4 keV. Candidates ^{197}Au gamma transitions are: 77.351 keV, 191.437 keV, 279.01 keV, 547.5 keV.

By taking advantage of the good separation of QE and FF events in the mass-TKE matrix, it is possible to estimate the QE and FF gamma fold distributions, namely, the distributions of the number of gamma rays detected per event, by gating on the mass-TKE distribution only. In addition to the previous processing of gamma rays, the fold extracted from PARIS detectors had to be corrected for cross-talk among the phoswiches packed in a 3×3 cluster configuration. The correction has been done using a simple algorithm: if two or more neighboring detectors produce signals in a single event, their total contribution to the fold is considered to be 1. Background has been also subtracted. An estimate of background gives 1.5% for ORGAM and 0.5% for PARIS.

3.3.3 The gamma ray fold distributions

Figure 3.12 shows the comparison between the gamma fold distributions obtained with PARIS alone (green line), ORGAM alone (red line) and PARIS+ORGAM considered as

a single array (labeled as TOT, blue line) in coincidence with all binary FMT events. For each distribution the yields are normalized to the yield without gamma rays in coincidence (gamma fold = 0). No efficiency correction is performed on these data. Average fold values are: 0.03 ± 0.02 for PARIS alone, 0.09 ± 0.03 for ORGAM alone and 0.12 ± 0.04 for PARIS+ORGAM combined (TOT). These averages are consistent with the fact that PARIS and ORGAM have different efficiencies.

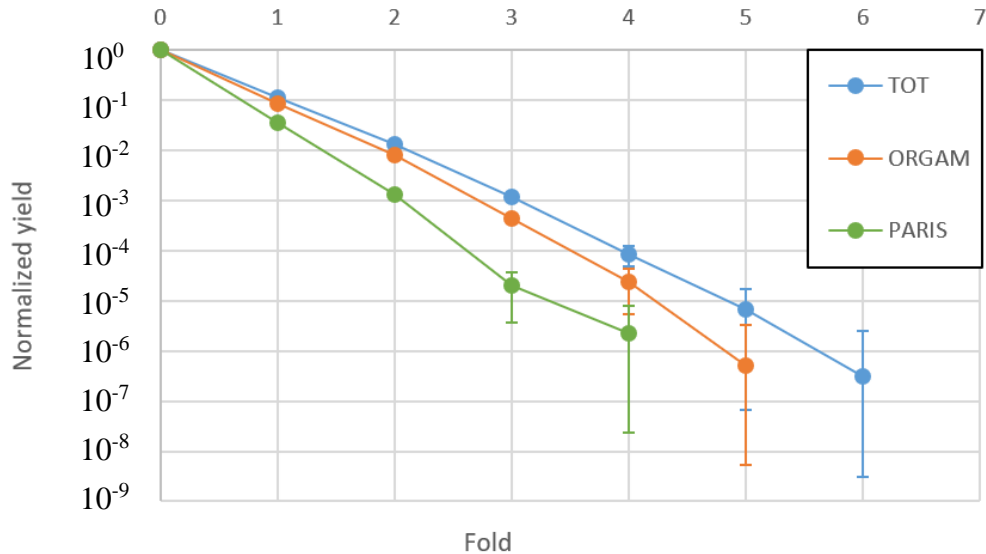


Fig 3.12 Gamma fold distributions for gamma rays obtained with PARIS alone (green line), ORGAM alone (red line), and PARIS and ORGAM considered as a single array (labeled as TOT, blue line) in coincidence with all binary events. Counts are normalized for comparison.

To verify that the differences between the three distributions are only due to the efficiency and not to other effects (*i.e.* corrections for the cross-talk or background for the different arrays), ORGAM and PARIS gamma fold distributions have been processed by taking into account the energy averaged total efficiencies of ORGAM and PARIS independently. The efficiencies are $\varepsilon_P = 0.6\%$, $\varepsilon_O = 1.3\%$ $\varepsilon_{TOT} = \varepsilon_P + \varepsilon_O = 1.9\%$ for PARIS, ORGAM and PARIS+ORGAM combined, respectively.

Figure 3.13 shows the comparison the ORGAM fold distribution with the one of PARIS (labelled PARIS(1)) corrected for the efficiency ratio between ORGAM and PARIS. The ansatz is that if the two arrays measure the same fold distribution, the ratio between the yields of each fold $Y_O(\text{fold}) = Y_P(\text{fold})$ is given by the ratio of the efficiencies to the fold power, namely:

$$Y_O/Y_P = (\varepsilon_O/\varepsilon_P)^{(\text{fold})} \quad [3.2]$$

The new fold distribution labeled as PARIS (1) in Figure 3.13 turns out to be in excellent agreement with the ORGAM fold distribution.

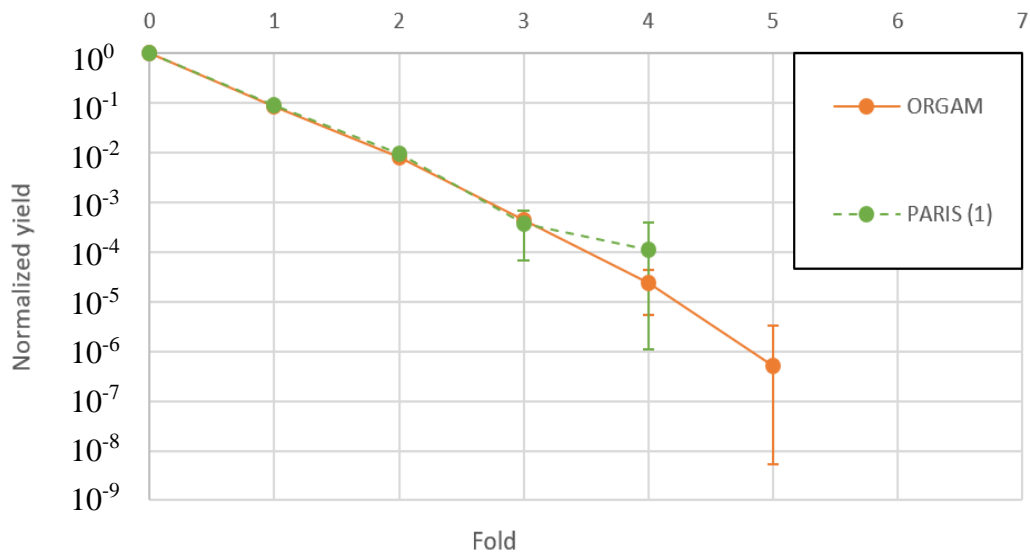


Fig 3.13 Gamma fold distribution for gamma rays detected in coincidence with binary events by ORGAM (red line), and PARIS, renormalized for the efficiency ratio (PARIS (1), green line). Counts are normalized for comparison.

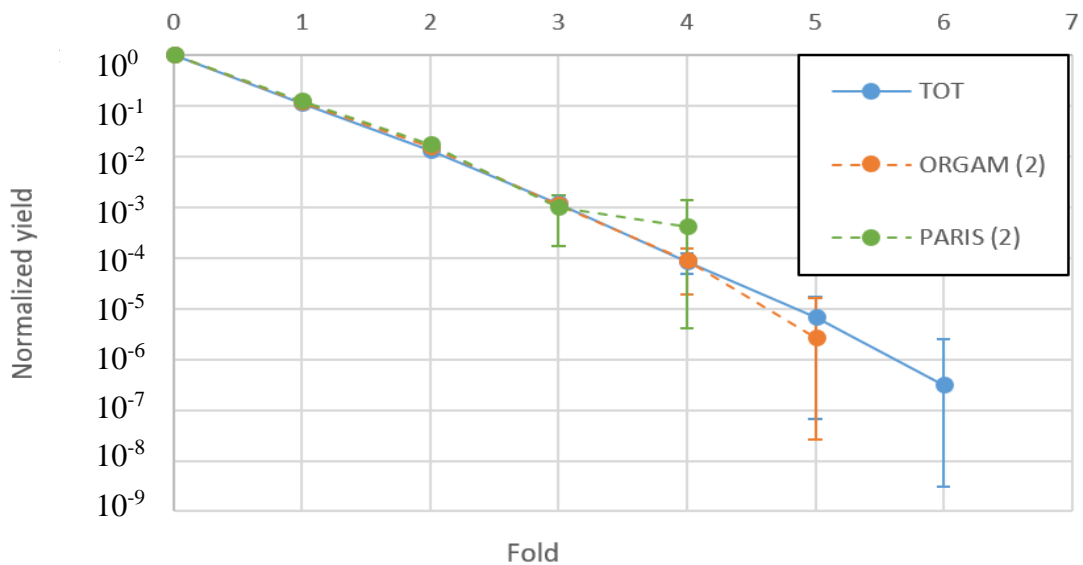


Fig 3.14 Gamma fold distribution for gamma rays detected in coincidence with binary events by ORGAM and PARIS together (blue line) compared to PARIS and ORGAM distributions, renormalized for efficiency (ORGAM (2), red line, and PARIS (2), green line). Counts are normalized for comparison.

To complete the check, both ORGAM and PARIS fold distributions were processed in the same way as above but now referring to the total detection efficiency. The new distributions, ORGAM (2) and PARIS (2), are shown in Figure 3.14 compared to the TOT fold distribution. The average fold values for these new distributions are $0.13 \pm$

0.06 for PARIS(2) and 0.13 ± 0.04 for ORGAM(2), in good agreement with TOT average fold value (0.12 ± 0.04). The positive outcomes of these stringent tests gives confidence that it is possible to manage the different characteristic features of ORGAM and PARIS in a proper way. Therefore, PARIS and ORGAM can be managed as a single array and work out directly on the total fold distribution. It is possible to further note, as expected, that when considered as a single array, PARIS and ORGAM combined can measure a larger fold than when they are taken singularly. Consequently, it is convenient to combine gamma ray detectors when there is an interest in the measurements of high-fold processes.

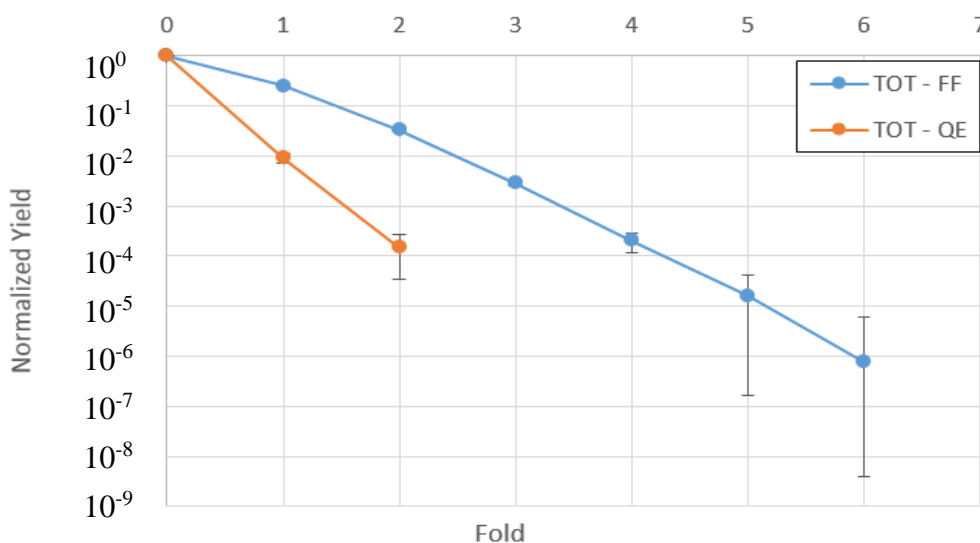


Fig 3.15 Gamma fold distributions detected with PARIS and ORGAM together in coincidence with quasi elastic products (“QE”, blue) and fission fragments (“FF”, red). Counts are normalized for comparison.

Finally, the TOT fold distributions of gamma rays detected in coincidence with FF and QE products were extracted and are compared in Figure 3.15. The gamma fold distribution of quasi elastic events drops much faster than the FF one, by orders of magnitude. Furthermore, in FF events, up to 6 gamma rays have been detected in coincidence, whereas in QE events 2 was the maximum fold observed. The average fold associated to fusion-fission events is 0.26 ± 0.07 , the average fold associated to quasi-elastic events is 0.009 ± 0.004 . Under the hypothesis that the gamma detection efficiency does not change sensibly with the binary channel (QE or FF) these data confirm that the gamma fold distribution could represent an observable sensitive to the reaction time scale. For a faster process a lower amount of orbital angular momenta is expected to be transferred than in a slower process. This translates in a smaller average gamma fold for the faster process.

3.3.4 *The response matrix of ORGAM + PARIS*

The conversion of the measured fold distribution into the real multiplicity distribution is usually a complex task which requires some well-constrained guesses. The complexity is due to the fact that the detected number of gammas in each event is less than the number of gammas truly emitted in an event because of the limited (intrinsic and geometrical) efficiency of the detectors. For instance, $\text{fold} = 1$ means that only one gamma ray is detected out of the many (unknown number) emitted. Therefore, $\text{fold} = 1$ is the overlap of a distribution of an unknown number of gamma rays being the process of detection of stochastic origin. In other words, it is necessary to calculate what is the probability that $\text{fold} = 1$, for instance, is due to a multiplicity of 1; 2; 3... n gamma rays truly emitted. This is also called the response function of the gamma detecting array. In general, one can expect that increasing the number of gammas truly emitted also the probability of detecting more than one gamma ray increases. However, the rate of such increment is strongly dependent on the detector efficiency. Thus, to obtain an estimate of the multiplicity distribution, since the fold distribution has been measured, the response function should be inverted.

To compute the response function in a way to include the characteristic features of ORGAM + PARIS setup, namely the geometrical plus the intrinsic efficiency and the dependence of the intrinsic efficiency on the energy of the gamma rays as measured, a Monte Carlo simulation code has been prepared. This code generates a matrix $P(F, M)$ that gives the conditional probability that F gamma rays are detected out of M emitted in the physical event, within an interval of values selected by the user $[M_{\gamma, \min}, M_{\gamma, \max}]$. Namely, the code calculates what is the probability that a fold F comes from a multiplicity M_{γ} .

The code works by generating M_{γ} gamma rays per event, from a user-defined distribution limited in the range $M_{\gamma, \min}$ to $M_{\gamma, \max}$, each with a randomly generated direction and energy. The directions are generated isotropically and the energies are generated according to a user defined distribution. Afterwards, the code checks how many gamma rays are detected by comparing the direction of each gamma ray with the detectors positions and geometrical openings given by the user. For each gamma ray firing a detector, the code compares a randomly generated number in the interval $[0, 1]$ with the intrinsic efficiency of the fired detector. The intrinsic efficiencies have been

experimentally measured and implemented in the code according to the equation 3.1. If the random number is lower than the efficiency, the gamma ray is considered to be detected, otherwise not. Given the number F of gamma rays detected out of M_γ gamma rays generated and repeating the process enough times to have a sufficient precision, the matrix $P(F, M_\gamma)$ is generated.

To test the validity of this method, a comparison have been made with the results of the formula proposed in ref. [43] for the probability $P(F, M_\gamma)$:

$$P(F, M_\gamma) = a_F P(F, M_\gamma - 1) + b_F (F - 1, M_\gamma - 1) + c_F P(F - 2, M_\gamma - 1) \quad [3.3]$$

with:

$$a_F = 1 - (N - F)\varepsilon \left(1 + \omega \frac{F}{N - 1}\right)$$

$$b_F = (N - F + 1)\varepsilon \left(1 - \omega \frac{N - 2F + 1}{N - 1}\right)$$

$$c_F = (N - F - 2)\varepsilon \omega \left(\frac{N - F + 1}{N - 1}\right)$$

being M_γ the multiplicity, F the number of triggered detectors out of N total detectors with equal energy-independent efficiency (ε), and equal cross-talk probability (ω), with $P(F, M_\gamma) = 0$ for $F < 0$ and $M_\gamma \leq 0$ and $P(F, M_\gamma) = 1$ for $F = M_\gamma = 0$. (The notation has been changed with respect to the original reference for uniformity reasons). The term accounting for cross talk in this formula has been put to 0, having the experimental cross-talk already been accounted for in the data.

This formula is based on a recursive algorithm and includes a total efficiency independent from the gamma ray energy. In the first test, the same dummy value for the detector efficiency has been used in both the formula and the Monte Carlo code. To make the test independent from the gamma ray energy, the intrinsic efficiency was set equal to 1, namely, it was considered the geometrical efficiency only. Furthermore, the input M_γ distribution is uniform in $[M_{\gamma, \min}, M_{\gamma, \max}]$. Figure 3.16 shows the comparison between the results of two different methods of computing the probability $P(F, M_\gamma)$ for 3 different values of the fold: 0, 1, and 2. As expected, the results obtained with the two methods are indistinguishable. The trends of the curves are in agreement with the expectation: the probability of detecting more than one gamma ray increases as the

multiplicity increases and the maximum of the curve for each fold moves toward larger multiplicities.

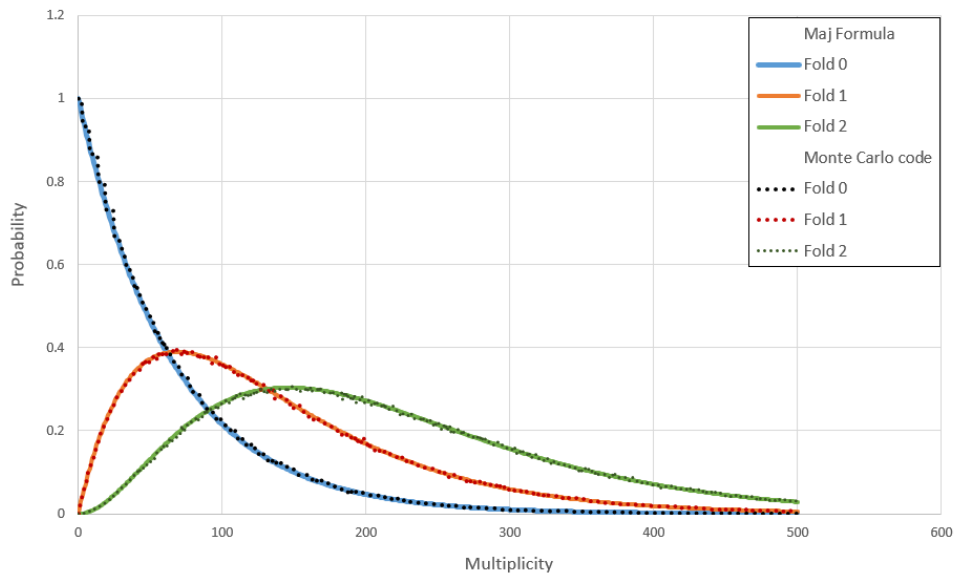


Fig 3.16 Comparison between the multiplicity distribution computed with the Monte Carlo code (dots) and the formula 3.3 from ref [43] for 3 different values of fold. The efficiency used is only geometrical.

To check the effects of the gamma ray energy dependence of the efficiency, another comparison has been made between the two methods. In the formula 3.3 only an average energy-independent efficiency is accounted for. For this case, it has been used the efficiency obtained as the average over the full energy range (weighted for the experimental gamma energy spectrum) and over different detectors. In the code it is possible to take advantage of the intrinsic flexibility of a Monte Carlo approach and for each detector the relative measured efficiency curve has been considered. This flexibility is essential because ORGAM and PARIS detectors are characterized by very different intrinsic efficiencies. This means that in a single tool it is possible to include detectors with different performances. In the test, the energy spectrum is chosen as a flat distribution between 150 and 3000 keV. Figure 3.17 shows the comparison between the two different methods for 3 different values of the fold: 0, 1, and 2. It is clear that there are only slight differences between the two methods which seem to disappear for increasing fold values above 2.

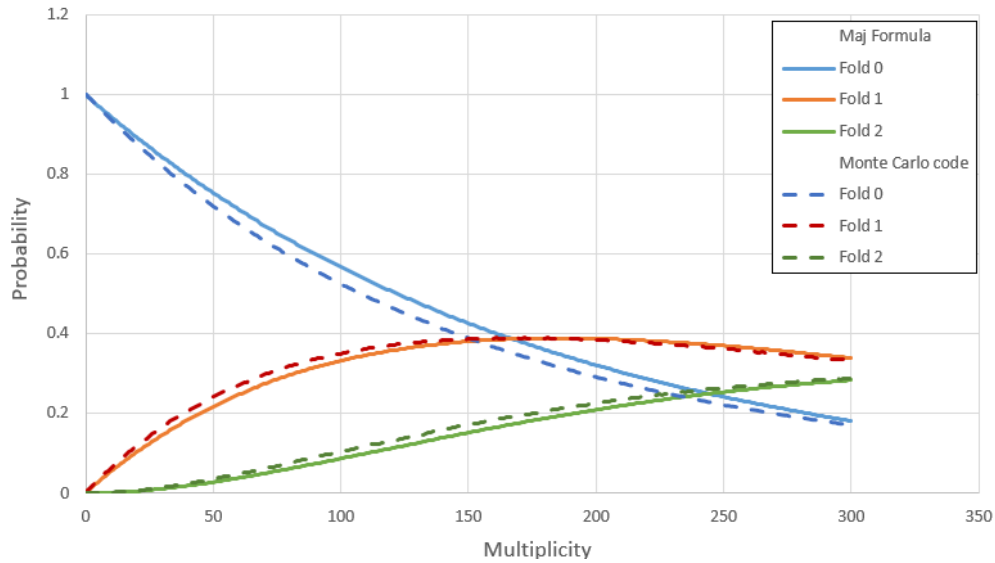


Fig 3.17 Comparison between the calculation of the probability $P(F, M)$ made with the new code, which now includes the dependence of the detection efficiency on the gamma ray energy and the formula 3.3 from ref [43] for 3 different values of fold. Solid lines are the prediction of the formula, dashed lines are the results of the Monte Carlo code.

Therefore, a tool to compute the fold distribution for known multiplicity distribution, has been successfully developed. In the tests above, an input uniform multiplicity distribution has been used within a user defined interval $[M_{\gamma, \min}, M_{\gamma, \max}]$. In principle, any shape can be used. Essentially, it has been set up a filter (that mocks the experimental setup) that tells us what is the probability of detecting F gammas when M are emitted in an event. However, for the study purpose the process has to be inverted, namely, the goal is to extract the M_{γ} distribution for a given or measured fold distribution. This inversion is not straightforward and it is more convenient to find a motivated reasonable guess for the true multiplicity distribution and compare the computed fold distribution (via the response function) with the measured one. Therefore, a guess is needed for the multiplicity distribution which should be grounded on some physical information.

3.3.5 From gamma ray fold to multiplicity

In order to find the best guess for the multiplicity distribution the method proposed by Ockels [44] has been used. This method provides a rapidly converging algorithm to compute the first few moments of the multiplicity distribution given the measured fold distribution and the efficiency of the gamma ray detecting array. The algorithm is based on the calculation of the probability of observing no gammas in $(N - n)$ detectors, where

N is the total number of detectors and n the triggered detectors.

Compared to other methods present in literature (see refs [45-47]), this method gives more precise results for lower values of the maximum observed fold. In the case presented in ref [44], the authors extracted ~95% of the information of the first 3 central moments of the multiplicity distribution from the probabilities up to fold = 6 (the percentage is evaluated from the cumulative contribution to the central moments of the terms containing the fold probabilities). In general, the largest is the fold measured, the larger is the number of moments that can be computed.

The equation used for the extraction of the multiplicity distribution moments is:

$$\begin{aligned} \frac{\ln\langle G_n \rangle_{exp}}{y_n} = \langle M \rangle + y_n \frac{\mu_2}{2!} + y_n^2 \frac{\mu_3}{3!} + y_n^3 \frac{\mu_4 - \mu_2^2}{4!} \\ + y_n^4 \frac{\mu_5 - 10\mu_3\mu_2}{5!} + \dots \end{aligned} \quad [3.3]$$

where μ_j is the j -th moment of the distribution with respect to the average, $\langle G_n \rangle_{exp}$ and y_n are related respectively to the experimental probabilities $\langle P_F \rangle_{exp}$ of observing a given F and to the detection efficiencies (ε , considered to be independent from the gamma energies and the same for all detectors) as follow:

$$\begin{aligned} \langle G_n \rangle_{exp} &= \sum_{F=0}^n \binom{n}{F} \binom{N}{F}^{-1} \langle P_F \rangle_{exp} \\ y_n &= \ln(1 - (N - n)\varepsilon) \end{aligned}$$

(The notation has been changed with respect to the original reference for uniformity reasons).

By using Equations 3.3 (truncated to the term in μ_4) the value of the first 3 moments of the gamma multiplicity distributions associated to FF and QE fold distributions in Figure 3.15 have been obtained. The efficiency parameters used in the formula were obtained as the average over the energy (weighted for the experimental gamma energy spectrum) and over different detectors. Table 3.1 shows the different values obtained for the moments of the two gamma multiplicity distributions.

Although the 3rd moment precision is very low - this should be due to the big error in the experimental probabilities for the higher FF folds (fold = 5 and 6) and to the too low maximum observed QE fold (fold_{max} = 2), even if the error is not greater than the

parameter - a higher gamma multiplicity is associated to fusion-fission. Consequently, this study demonstrates that gamma multiplicity distribution unambiguously represents an observable sensitive to the reaction time scale.

Tab 3.1 Momenta of the multiplicity distribution associated with fusion-fission (FF) and quasi elastic (QE) events.

Moments	$\langle M \rangle$	μ_2	μ_3
FF	12.5 ± 0.4	23 ± 6	100 ± 200
QE	0.46 ± 0.05	1.0 ± 0.5	1.2 ± 0.6

The obtained parameters (1st and 2nd momenta) have been used in the reconstruction of the multiplicity distributions. In both the FF and QF channels, it has been used the negative binomial distribution function, a 2-parameters asymmetric probability distribution for discrete variables, well suited for the description of a multiplicity distribution [48]. The probability mass function is given by:

$$P(k) = \binom{k+r-1}{k} (1-p)^r p^k \quad [3.4]$$

with p and r related to the average and the variance of the distribution through the following:

$$\mu_1 = \frac{pr}{1-p}$$

$$\mu_2 = \frac{pr}{(1-p)^2}$$

As p and r assume non-integer values in the present case, the factorials have been calculated through the gamma function. Figures 3.18 and 3.19 show the plot of the negative binomial distributions in case of FF and QE respectively with parameters given in Table 3.1. Min and Max in the legend correspond to the limiting distributions due to the errors in the moments.

These multiplicity distributions have been converted back into fold distribution using the Monte Carlo code presented in Section 3.3.4 and compared to the experimental data. Figures 3.20 and 3.21 show the comparison between the experimental fold distribution and the minimum and maximum multiplicity distribution presented in Figures 3.18 and 3.19, for CNF and QE events, respectively.

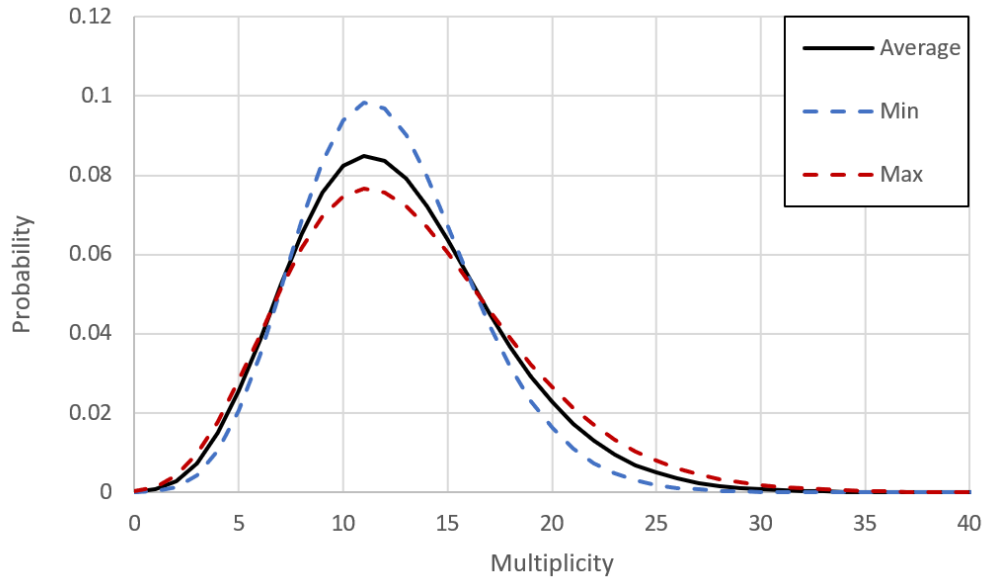


Fig 3.18 Gamma ray multiplicity distribution associated to FF events reconstructed through the method proposed in ref [44] and assuming a negative binomial distribution (black solid line). The min and max curve in the legend correspond to the limiting distributions due to the errors in the shape parameters as in Table 3.1.

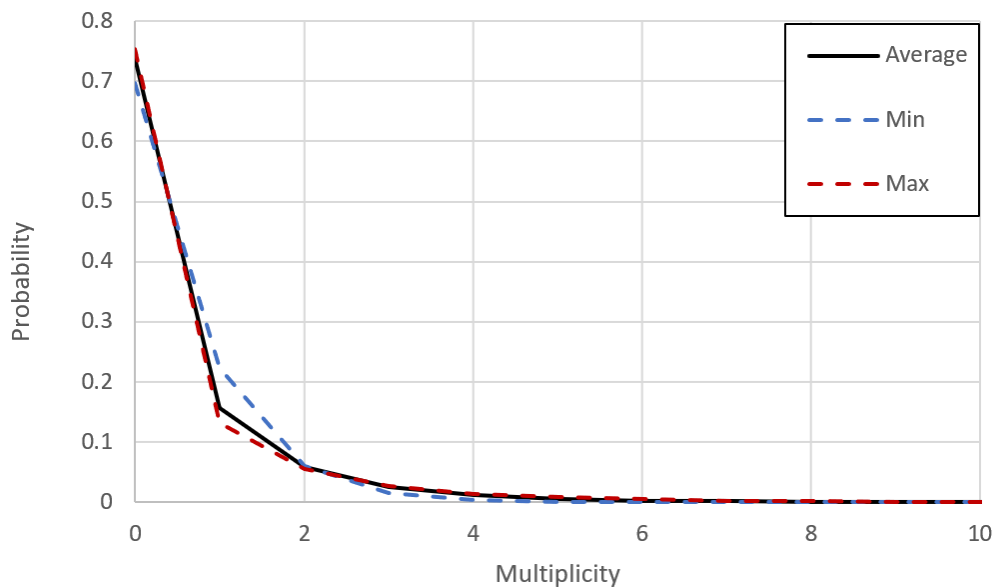


Fig 3.19 Gamma ray multiplicity distribution associated to QE events reconstructed through the method proposed in ref [44] and assuming a negative binomial distribution (black solid line). The min and max curve in the legend correspond to the limiting distributions due to the errors in the shape parameters as in Table 3.1.

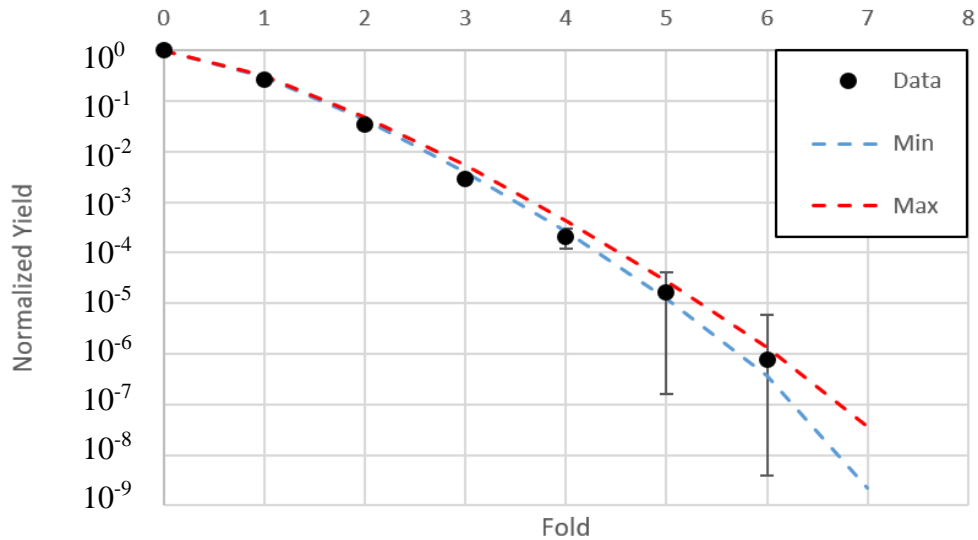


Fig 3.20 Experimental gamma ray fold distribution associated to FF events (black dots) compared to the min and max multiplicity distribution presented in Figure 3.18 converted back into fold distribution through the Monte Carlo code (blue and red dashed lines).

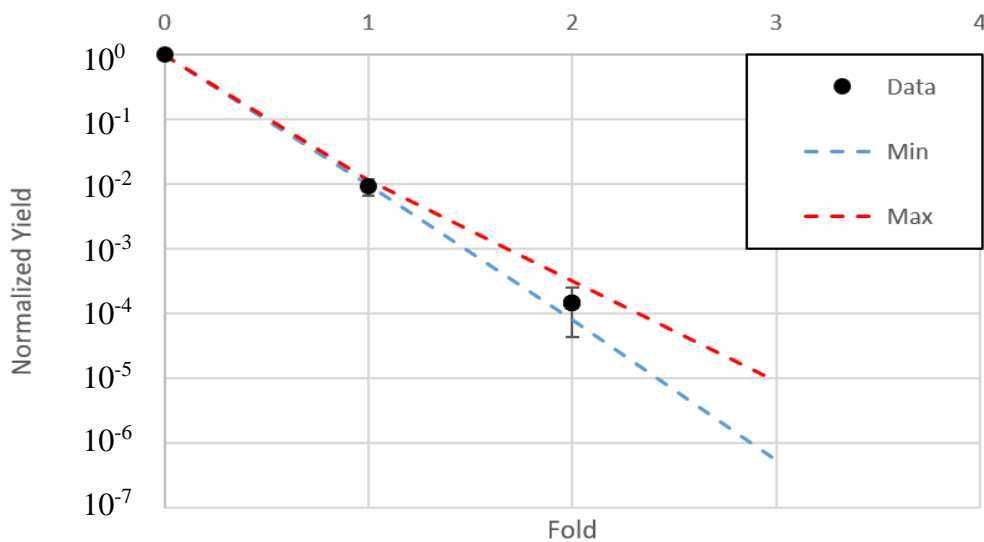


Fig 3.21 Experimental gamma ray fold distribution associated to QE events (black dots) compared to the min and max multiplicity distribution presented in Figure 3.19 converted back into fold distribution through the Monte Carlo code (blue and red dashed lines).

3.3.6 Comparison with simulations

These results are of great importance because, if this reconstruction is well made, it means that with a gate on high multiplicity events it is possible to separate processes with different time scales, in this case quasi elastic and fusion-fission.

To gain confidence in the good agreement shown in Figures 3.20 and 3.21, it has been chosen to simulate the fission process and the related gamma ray emission with the GEF (GEneral description of Fission observables) code [49]. In the simulation the input

parameters in GEF have been fixed by considering interaction potential calculation for the average angular momentum of the compound nucleus ($I_{\text{rms}} = 12.4 \hbar$) and using the excitation energy ($E^* = 43.5 \text{ MeV}$) from simple kinematic calculation, known the fusion Q-value.

To verify the correctness of the input parameters, the simulated mass distribution, TKE distribution and gamma energy spectra have been compared to the experimental data. In order to properly compare the two different results, the experimental mass and TKE distributions have been corrected for kinematic efficiency of the CORSET detectors. The gamma energy spectrum used is the sum of the spectra detected with the ORGAM detectors and corrected for the detection efficiencies. Figure 3.22, Figure 3.23 and Figure 3.24 show respectively the experimental mass distribution, the experimental TKE distribution and the experimental gamma ray energy spectrum compared to GEF simulations. The GEF simulated observables have been renormalized for the comparison.

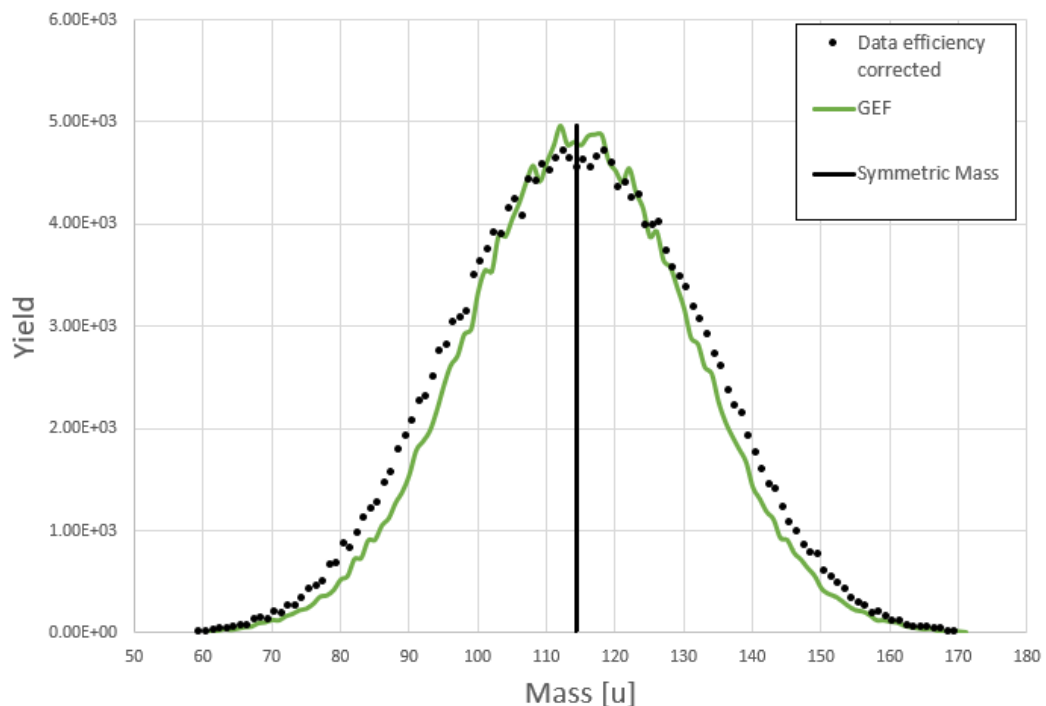


Fig 3.22 The experimental mass distribution efficiency corrected (black dots) compared to GEF simulation. The vertical black line indicates the symmetric mass split.

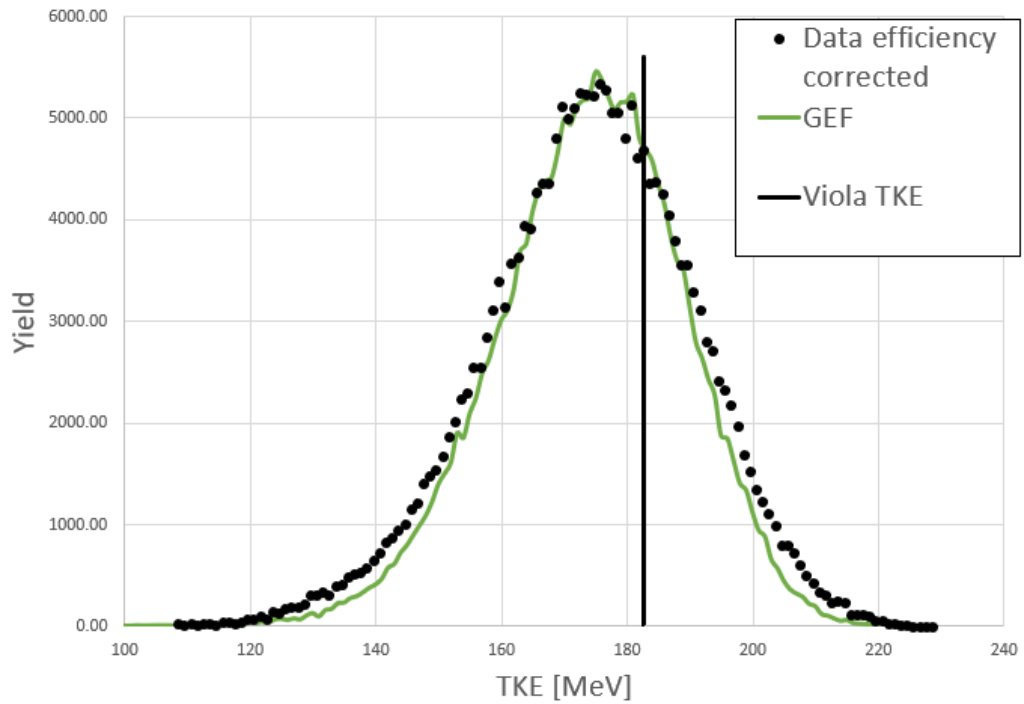


Fig 3.23 Experimental TKE distribution efficiency corrected (black dots) compared to GEF simulation. The vertical black line indicates the Viola TKE_s as defined by Equation 1.12.

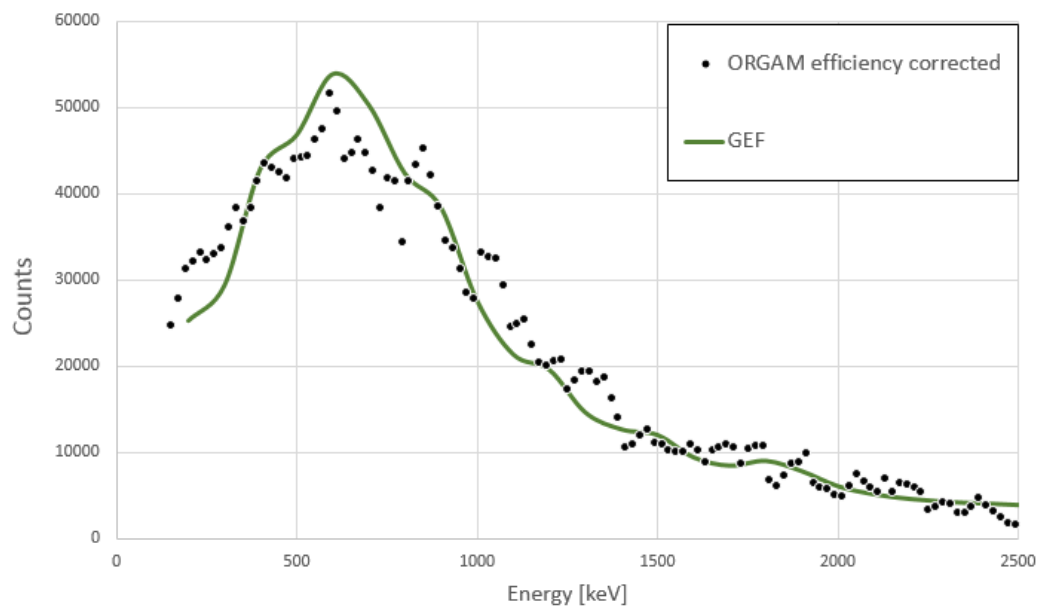


Fig 3.24 Experimental gamma ray energy spectrum (black dots) detected by ORGAM detectors and efficiency corrected compared to GEF simulation.

Next, gamma multiplicity distributions were compared. Figure 3.25 shows the multiplicity distribution simulated with GEF (green solid line) compared to the min and max multiplicity distributions (blue and red dashed lines). The average multiplicity for the GEF simulated distribution is 12.5, in perfect agreement with the average multiplicity presented in Table 3.1. The simulated multiplicity distribution has been converted into fold and compared to experimental data, as shown in Figure 3.26. Experimental data are represented with black dots with errors, green solid line is the GEF simulated multiplicity distribution converted into fold by the Monte Carlo code and blue and red dashed lines are the min and max distributions obtained with the method presented in ref [44]. The average fold value associated with GEF simulation is 0.30 (to be compared with 0.26 ± 0.07).

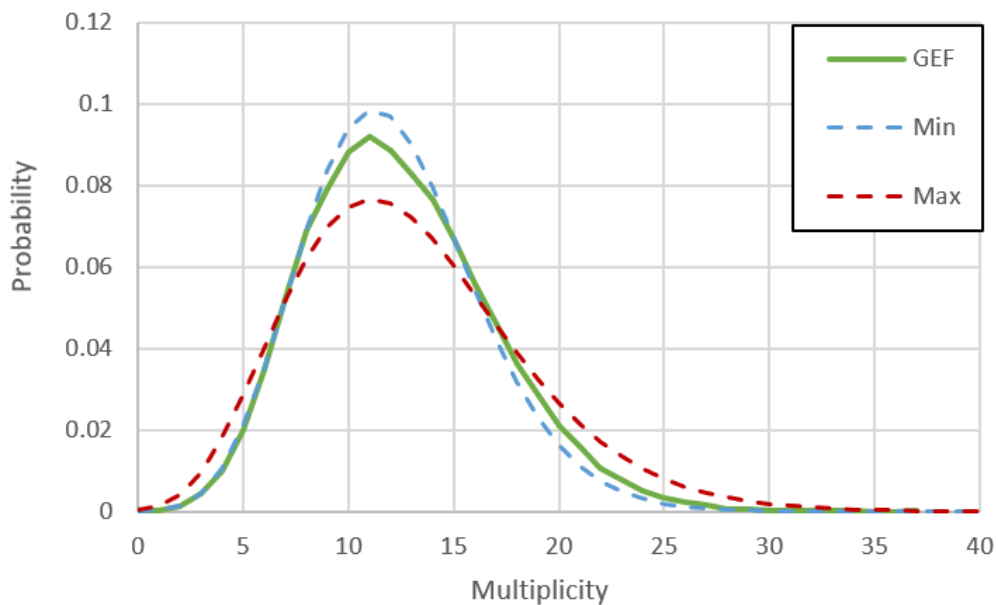


Fig 3.25 Gamma ray multiplicity distribution associated to FF events simulated by GEF (green solid line), compared to the multiplicity distribution min and max (blue and red dashed lines).

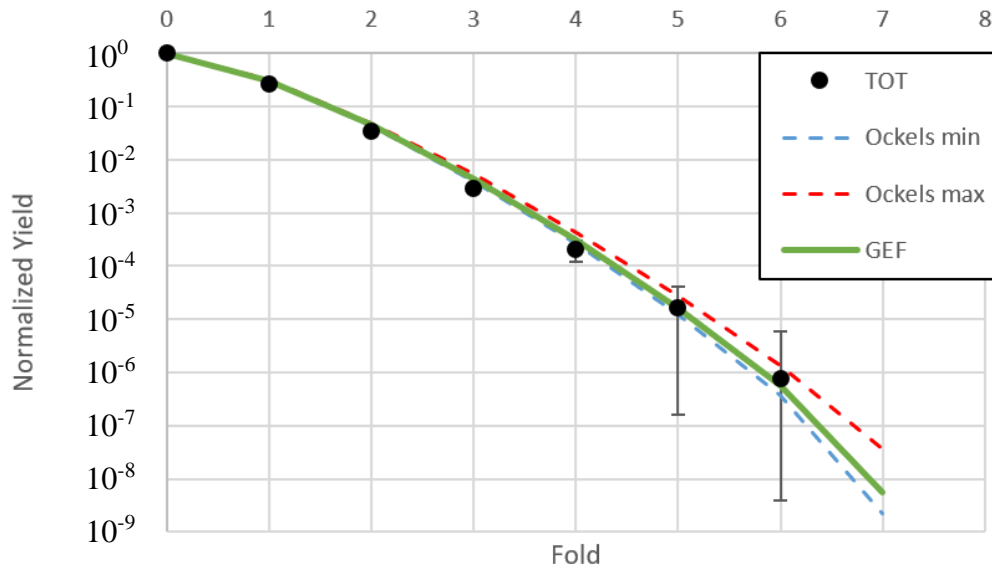


Fig 3.26 Experimental gamma ray fold distribution associated to FF events (black dots) compared to the GEF simulated multiplicity distribution converted into fold through the Monte Carlo code (green solid curve) and min and max fold distributions (blue and red dashed lines).

3.3.7 Angular momentum transfer

The next and final task of this data analysis is to estimate, from the measured multiplicity distributions, the amount of the initial orbital angular momentum that is transformed into the angular momentum of the final fragments in the FF and QE channels, $|\vec{l}_i - \vec{l}_f|$. \vec{l}_i and \vec{l}_f are, respectively, the entrance and exit channel orbital angular momenta and are related, by the conservation law, to the spin of the two fragments at the scission point, \vec{J}_1 and \vec{J}_2 , namely:

$$\vec{l}_i = \vec{J}_1 + \vec{J}_2 + \vec{l}_f = \vec{J} + \vec{l}_f \quad [3.5]$$

For the average values one obtains:

$$\langle J \rangle = \langle \vec{l}_i - \vec{l}_f \rangle \quad [3.6]$$

In other words, $\langle J \rangle$ is the average angular momentum transferred from the orbital angular momentum to the intrinsic spin of the fragments, the central observable in this work. M_γ distributions include contributions from both fragments but is independent from the relative orientation of their respective angular momenta \vec{J}_1 and \vec{J}_2 . Therefore $\langle M_\gamma \rangle$ depends on the average angular momentum $\langle J \rangle$ at scission point

The conversion from $\langle M_\gamma \rangle$ to $\langle J \rangle$ involves however some uncertainties. It is generally assumed that the fragments deexcite in two steps. First, emission of light particles, that carry away some angular momentum, and then gamma ray emission when the excitation energy becomes low enough to hinder particle emission. At this second stage, most of the decays proceed via stretched $E2$ transition, corresponding to a spin change $2 \hbar$, while a small number proceed via statistical gamma rays by dipole transitions which correspond to an average spin change $0.5 \hbar$. The total amount of orbital angular momentum transferred into intrinsic angular momentum l_f is given by:

$$\langle J \rangle = \langle \Delta I_{lp} \rangle + \langle \Delta I_\gamma \rangle \quad [3.7]$$

where ΔI_{lp} and ΔI_γ are the angular momentum carried away by the light particles and rays, respectively. Therefore, the measured $\langle M_\gamma \rangle$ is a function of $\langle J \rangle$ but also of the excitation energy at scission point. Because of Equation 3.7, the conversion $\langle M_\gamma \rangle$ to $\langle J \rangle$ suffers from the lack of knowledge of the spin removed by the evaporated particles and the average multiplicities of the gamma ray transitions. In the FF channel, at the low energy of our reaction, mostly neutrons are evaporated. From the data analysis performed in [50], an average of 6 neutrons are emitted per fission decay, as confirmed by GEF calculations, and can carry away on average $0.5 \hbar$. Therefore, $\langle \Delta I_{lp} \rangle = \langle N_n \rangle \langle l_n \rangle \approx 3 \hbar$, where $\langle N_n \rangle$ is the average number of evaporated neutrons and $\langle l_n \rangle$ is the average angular momentum carried away by a single neutron.

Tab 3.2 Estimate of the orbital angular momentum transferred $\langle J \rangle$ according to Equation 3.7 in the QE and FF channels. $\langle l_n \rangle$ is the average angular momentum carried away by a single neutron and $\langle N_n \rangle$ the average number of evaporated neutrons per fission events from fragments. $\langle M_\gamma \rangle$ is the experimental average multiplicity and α the average number of statistical gamma ray (dipole) transitions.

	$\langle l_n \rangle$	$\langle N_n \rangle$	$\langle \Delta I_{lp} \rangle$	$\langle M_\gamma \rangle$	α	$\langle \Delta I_\gamma \rangle$	$\langle J \rangle$
FF	$0.5 \hbar$	6	$3 \hbar$	12.5	3	$13 \hbar$	$16 \hbar$
QE	$0 \hbar$	0	$0 \hbar$	0.5	0	$0 \hbar$	$1 \hbar$

Accordingly, for the gamma rays it has been used a common and well-known expression [51]:

$$\langle \Delta I_\gamma \rangle = 2(\langle M_\gamma \rangle - 2\alpha) \quad [3.8]$$

where α is the average number of statistical (dipole) transitions. In this picture, stretched E2 transitions take away most of the angular momentum. By reviewing the pertinent literature, it has been used the values of $\alpha = 3$ as in Table 3.2, which also shows the transferred angular momentum as computed from Equation 3.8.

In the QE channel, the two nuclei barely overlap and their kinetic energies and masses are not altered appreciably. Therefore, the nuclei, after a transfer of few nucleons, continue along Coulomb-like trajectories given the expected relatively low dissipation of energy and angular momentum. The outgoing nuclei is not expected to carry enough excitation energy to induce neutron evaporation. Furthermore, only the very first few levels of the outgoing fragments can be excited. Consequently, during the gamma decay a gamma ray is expected to carry away, on the average, $1.5 \hbar$ of angular momentum. Given the measured $\langle M_\gamma \rangle = 1$ and $\sigma_{M_\gamma} = 1$, it can be reasonably deduced a narrow window of transferred angular momentum between 1 and $3 \hbar$ in the QE channel.

From Table 3.2 it is quite evident a striking difference between the angular momentum transferred in the FF and QE channels that holds regardless of the assumptions underlying Equations 3.7 and 3.8. This strong contrast could be expected from the average gamma multiplicities measured in the two channels, the implications of which will be discussed in the next Section.

As a further support to the whole procedure used to measure the $\langle M_\gamma \rangle$ and to connect it to the transferred angular momentum, is it possible to observe that the result presented in this work is in noteworthy agreement with the systematics proposed by Ogihara *et al.* [52] which connects the excitation energy of the fission fragments to the average angular momentum transferred to the fission fragments $\langle J \rangle$. According to the authors, it is possible to extract $\langle J \rangle$ as:

$$\langle J \rangle = 0.11 \langle E_f^* \rangle / MeV + 7.5 \hbar \quad [3.9]$$

where $\langle E_f^* \rangle$ is the average excitation energy of the two symmetric fragments. From the data analysis performed in [50], the average excitation energy of the symmetric fragments is $\sim 40 MeV$, as confirmed by calculations using the equations presented in ref. [52]. This brings to an expected value of $\langle J \rangle = 16.3 \hbar$, in great agreement with the analysis presented in this work.

3.3.8 Discussion

In the present measurements the average gamma multiplicity $\langle M_\gamma \rangle$ is used to determine the amount of angular momentum $\langle J \rangle$ introduced into internal rotation of the fragments produced in two-body decays over the full range of impact parameters, from fusion-fission to quasi-elastic reactions. It is found that in the FF channel $\langle J \rangle$ is much larger than in the QE channel. This result is understandable on the basis of the known picture of the FF and QE reaction paths. Classically, the conversion of orbital angular momentum of the entrance channel \vec{l}_i into intrinsic angular momentum of the fragments is described as the result of tangential friction. In a first step, the nuclei slide on each other and viscous forces set in a torque which puts them into rotation.

For angular momenta close to the maximum, the two nuclei undergo grazing collisions. Since the two nuclei barely overlap the kinetic energies and masses are not altered appreciably, and the nuclei continue along Coulomb-like trajectories. Hence, the reaction mechanism is confined to a very narrow gap of orbital angular momentum around the grazing angle and only few nucleons are exchanged during a rather short interaction time.

For smaller impact parameters, or lower l waves, the closer contact leads to stronger damping of the kinetic energy and more extensive mass transfer. In these conditions, tangential forces continue to act until the system reaches a rolling stage in which the peripheral velocities are matched. Then, the rolling friction slows down the rotation of the nuclei until they form a rigid body (sticking condition) [2].

According to this view of the angular momentum transfer, one expects a rapid increase of the angular momentum transferred to the fragments with increasing interaction time until the rolling state is reached. The maximum value that J can reach, at the sticking point, is given by:

$$J = \frac{I_1 + I_2}{I_1 + I_2 + I_{rel}} l_i \quad [3.10]$$

where I_1 and I_2 are the moment of inertia of the fragments and I_{rel} is the moment of inertia of the relative motion.

The important point to remark here is that an increase of angular momentum transfer (or energy loss) is correlated to a growing interaction time, with the maximum dissipation of angular momentum and energy corresponding to complete fusion.

Afterward, the fused system may evolve as an evaporation residues or decays into fission. In any case, the complete fusion requires interaction times longer than peripheral reactions.

It is possible to check the consistency of the data in Table 3.2 with the above picture in mind. In the QE channel (the faster process) $\langle J \rangle$ is only few units of \hbar , namely almost no transfer of angular momentum occurs. Since this reaction is confined around the grazing angle $l_{gr} = 25 \hbar$, l_f remains confined around $25\hbar$ and $TKE \approx E_{CM}$. In the FF channel (the slower process), being l_i fully transformed into intrinsic spin, $\langle l_i \rangle \approx \langle J \rangle = 16 \hbar$. In the hypothesis of a triangular distribution, $\langle l_i \rangle = 16 \hbar$ corresponds to a maximum orbital momentum $\langle l_{max} \rangle = 24 \hbar$. In other words, the whole in-going orbital angular momentum distribution is exhausted by the FF and QE channels.

A further check on the outgoing orbital angular momentum l_f comes from the evaluation of the TKE. With the assumption of rigid rotation of the dinuclear complex at scission, the total kinetic energy of the fragments can be expressed as the sum of their Coulomb repulsion and rotational energies:

$$TKE = \frac{Z_1 Z_2 e^2}{d} + \frac{l_f(l_f + 1)\hbar^2}{2\mu d^2} \quad [3.11]$$

where d is the separation distance of the fragments at scission and l_f is their relative orbital angular momentum. By taking the TKE for symmetric mass split and considering the final fragment with ellipsoidal shape (with their axes of symmetry along the axis joining their center) having a deformation parameter $\beta = 0.6$, it results $l_f = 0$. This result is in agreement with the hypothesis that the whole in-going orbital angular momentum is dissipated and appears as spin of the fragments.

Chapter 4 – Conclusions and perspectives

4.1 Experiment $^{64, 68}\text{Zn} + ^{112}\text{Sn}$

Mass distributions for binary fragments were measured in the systems $^{64, 68}\text{Zn} + ^{112}\text{Sn}$ at different bombarding energies. The observations suggested an interpretative key to the fact that the mass distribution of ^{180}Hg becomes more symmetric with increasing excitation energy whereas the one of ^{176}Hg becomes more asymmetric, the main subject of this experiment.

In the case of ^{180}Hg , in the computed mass distributions, the calculated symmetric mode contribution becomes larger with increasing excitation energy. However, the more asymmetric mode, centered at $A = 71$ and 109 , has been observed to remain dominant. The fact that the whole mass distribution becomes more symmetric has been explained with the concurrent increase of the symmetric component and the weaker medium-asymmetric mode, centered at $A = 80$ and 100 . With further increase of the excitation energy, the symmetric mode becomes dominant, the medium-asymmetric mode disappears, and the most-asymmetric mode clearly survives. This is consistent with the expectations that the shell effects are gradually quenched with increasing excitation energy, each mode disappearing at different excitation energy, but only the symmetric mode is last survivor.

In the case of ^{176}Hg , the computed mass distributions, with increasing excitation energy, become more asymmetric. The competition of the different three modes identified by the combined analysis with the experimental data held the key for the interpretation of this behavior: the symmetric mode is reduced with increasing excitation energy, but the rate of the growing asymmetry is the consequence of the dropping of the mid-asymmetric mode, centered at $A = 77$ and 99 , and the strong increase of the most-asymmetric mode, centered at $A = 110$ and 66 . Therefore, the symmetric mode is hindered by the most-asymmetric mode and partially by the mid-asymmetric mode, at variance with the behavior of ^{180}Hg . The comparison with experimental data showed a curious drop, at a certain excitation energy, of the relative intensity of the symmetric mode (and not a continuous growing) triggered, reasonably, by the increase of the most-asymmetric mode. The same behavior occurs, but to a minor extent, to the mid-asymmetry mode. The dominance of the most-asymmetric mode is

the cause of the hindrance of the mass symmetric mode. This behavior is not reproduced in the calculations. However the finding in the experimental data of the same modes that reproduce the calculated mass distributions for both ^{176}Hg and ^{180}Hg is already an important result because it tells that the shell corrections occur in the same place in the potential as calculated. From this analysis, we can confirm that ^{176}Hg behaves at variance with what expected. In particular, the relative strength of the different fission modes changes quite surprisingly with the excitation energy. This finding of course requires further work for its confirmation.

4.2 Experiment $^{32}\text{S} + ^{197}\text{Au}$

Gamma rays multiplicity M_γ distributions were measured in the system $^{32}\text{S} + ^{197}\text{Au}$ in coincidence with the QE and FF fragments. The aim is to show that, by selecting a faster and a slower process in the Mass-TKE matrix, the slower process is characterized by a larger transfer of the in-going orbital angular momentum. The interpretation of the data is supposed to rely on the fact that QE and FF reaction paths are known to be at the extreme of the interaction time scale: the fastest and the slowest, respectively. It is found that the average values of such M_γ distributions are consistent with a full transfer of the in-going orbital angular momentum l_i to the spin of the fragments on the FF channel, whereas only a few units of \hbar are transferred to the QE fragments.

The observation that the average gamma rays multiplicity $\langle M_\gamma \rangle$ is larger for the slower reaction channel gives support to the expectation that increasing amounts of orbital angular momentum can be transferred only by selecting slower and slower processes. It is important to remark that the observed quantities are the lower moments of the multiplicity distribution (mean and variance). These quantities cannot therefore be obtained on an event-by-event basis, but only as an average over a sample of events. Consequently, those averages cannot be used for the reverse process of data analysis, namely, the selection of a slower process by gating on the multiplicity distribution. However, the most direct observable is the gamma fold distribution. Figure 3.15 is thus the key result of this work and shows that gating on higher fold processes favors the selection of the slower process. This results suggests that the gamma ray probe can play a very important role in disentangling FF and QF in the regions of the mass-TKE matrix where they are overlapped. The expectation is that QF is a process faster than FF and

should give rise to a lower gamma multiplicity, thus lower gamma fold values. To accomplish this separation a large efficiency for gamma ray detection would be mandatory.

For the future plans, it is crucial to test this method in condition of major interest: when FF and QF are overlapped with comparable intensity in the same mass region. However an intermediate step would be to measure the gamma fold distribution in systems where QF is dominant. It would also be important to benefit of the properties of the QF to populate unknown neutron-rich nuclei. Reactions can be chosen carefully to populate neutron-rich regions of the nuclide chart of specific interest, like the one of interest from the r-process. However, it is clearly evident that the experimental condition must be kept at the optimum and that much larger gamma ray detection efficiency is necessary to reach a sufficient statistics.

References

- [1] Hodgson, *Nuclear reaction and nuclear structure*, Oxford: Clarendon Press (1978)
- [2] R. Bass, *Nuclear Reactions with Heavy Ions*, Springer (1980)
- [3] I. Ahmad and W. R. Phillips, *Rep. Prog. Phys.* 58 (1995)
- [4] S. Cohen, F. Plasil and W. J. Swiatecki, *Ann. Of Phys.* 82, 557-596 (1974)
- [5] R. du Rietz *et al.*, *Phys. Rev. C* 88 054618 (2013)
- [6] V. Zagrebaev, W. Greiner, *Phys. Rev. Lett.* 101 (2008)
- [7] A. V. Karpov *et al.*, *J. Phys. G: Nucl. Part. Phys.* 35 (2008)
- [8] A. Yu. Chizhov *et al.*, *Phys. Rev. C* 67 (2003)
- [9] V. E. Viola *et al.*, *Phys. Rev.* 130 (1963)
- [10] V. E. Viola *et al.*, *Phys. Rev. C* 31 (1985)
- [11] M.G. Itkis *et al.*, *Z. Phys. A* 320 (1985)
- [12] I.V. Pokrovski, *et al.*, *Phys. Rev. C* 60 (1999)
- [13] H.C. Britt, H.E. Wegner, J.C. Gursky, *Phys. Rev.* 129 (1963)
- [14] M. G. Itkis *et al.*, *Nucl. Phys. A* 944 (2015)
- [15] K. H. Schmidt – fission – a complete laboratory. Preprint of a contribution to the proceedings of the Joliot – Curie school, Nice, France, 12th - 17th Sept 2011
- [16] U. Brosa *et al.*, *Phys. Rep.* 197, 167 (1990)
- [17] A. Ya. Rusanov *et al.*, in: Proceedings of the 2nd International Conference on Current Problems in Nuclear Physics and Atomic Energy, (NPAE-Kyiv2008), June 9 to June 15, 2008, Kyiv, Ukraine
- [18] A. N. Andreyev, K. Nishio and K.H. Schmidt, *Rep. Prog. Phys.* 81 016301 (2018)
- [19] S. Goriely *et al.*, *Phys. Rev. Lett.* 111, 242502 (2013)
- [20] A. N. Andreyev *et al.*, *Phys. Rev. Lett.* 105, 252502 (2010)
- [21] J. Elseviers *et al.*, *Phys. Rev. C* 88, 044321 (2013)
- [22] S. Panebianco *et al.*, *Phys. Rev. C* 86, 064601 (2012)

- [23] A. V. Andreev *et al.*, *Phys. Rev. C* 88, 047604 (2013)
- [24] P. Möller and J. Randrup, *Phys. Rev. C* 91, 044316 (2015)
- [25] P. Möller, J. Randrup, and A. J. Sierk, *Phys. Rev. C* 85, 024306 (2012)
- [26] E. M. Kozulin *et al.*, *Instr. and Exp. Tec.* 51 (2008)
- [27] D. Quero, Ph.D. Thesis, University of Naples Federico II.
- [28] E.M. Kozulin *et al.*, *Phys. Rev. C* 86, 044611 (2012)
- [29] Yu. Ts. Oganessian, A. Sobiczewski and G. M. Ter-Akopian, *Phys. Scr.* 92, 023003 (2017)
- [30] P.J. Karol, R.C. Barber, B.M. Sherril, E. Vardaci, T. Yamazaki, *Pure Appl. Chem.* 88, 139 (2016)
- [31] P.J. Karol, R.C. Barber, B.M. Sherril, E. Vardaci, T. Yamazaki, *Pure Appl. Chem.* 88, 155 (2016)
- [32] E. Vardaci *et al.*, *J. Phys. G: Nucl. and Part. Phys.* 46, 103022 (2019)
- [33] M. G. Itkis *et al.*, *Nucl. Phys. A* 787 (2007)
- [34] P. J. Nolan *et al.*, *Annu. Rev. Nucl. Part. Sci.* (1994)
- [35] A. Maj *et al.*, *Acta Phys. Pol. B* 40 565 (2009)
- [36] S. Brambilla, private communication (2012)
- [37] M. Romoli *et al.*, *IEEE Trans. Nucl. Sci.* 52, 1860 (2005)
- [38] C. Signorini *et al.*, *Eur. Phys. J. A* 44, 63 (2010)
- [39] D. Pierroutsakou *et al.*, *Eur. Phys. J. Special Topics* 150, 47 (2007)
- [40] M. Mazzocco *et al.*, *Eur. Phys. J. Special Topics* 150, 37 (2007)
- [41] A. Pulcini, E. Vardaci *et al.*, *Journal of Physics: Conference Series* 1014 (2018)
- [42] A. Pulcini, E. Vardaci *et al.*, *Exotic Nuclei - Proceedings of the International Symposium on Exotic Nuclei*, 330–337 (2019)
- [43] A. Maj *et al.*, *Nucl. Phys. A* 571, 185 (1994)
- [44] W.J. Ockels, *Z. Phys. A* 286, 181 (1978)
- [45] G.B. Hagemann *et al.*, *Nucl. Phys. A* 245, 106 (1975)
- [46] O. Anderson, *et al.*, *Nucl. Phys. A* 295, 163 (1978)
- [47] W. Kohl *et al.*, *Z. Physik A* 285, 17 (1978)

- [48] K. Werner, M. Kutschera, *Phys. Lett. B* 220, 243 - 246 (1989)
- [49] K. H. Schmidt *et al.*, *Nucl. Data Sheets* 131 (2016)
- [50] E.M. Kozulin, I. M. Harca, E. Vardaci, *et al.*, *Eur. Phys. J. A* 56, 6 (2020)
- [51] R. P. Schmitt, G. Mouchaty and D.R. Haenni, *Nucl. Phys. A* 427, 614 (1984)
- [52] M. Oghihara *et al.*, *Z. Phys. A* 335, 203 (1990)

